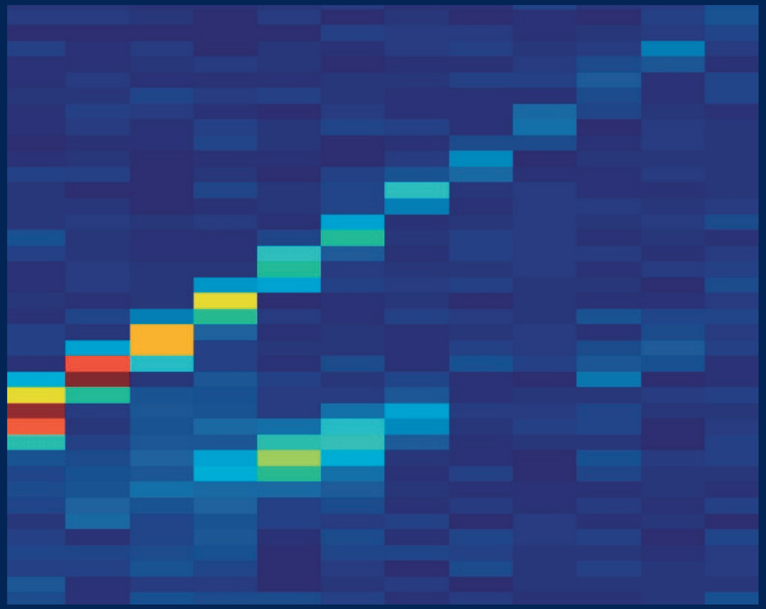

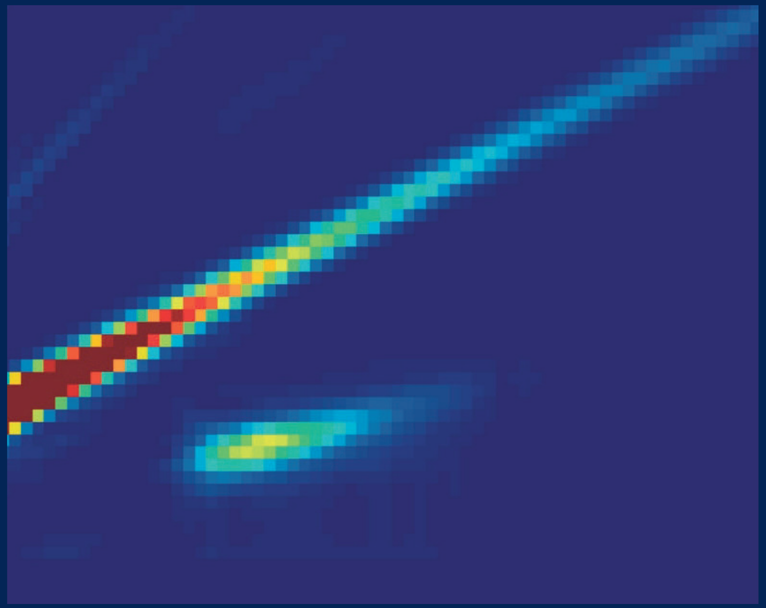

Ultrasound Contrast Agents - Optical and Acoustical Characterization Jeroen Sijl

Ultrasound Contrast Agents
Optical and Acoustical Characterization

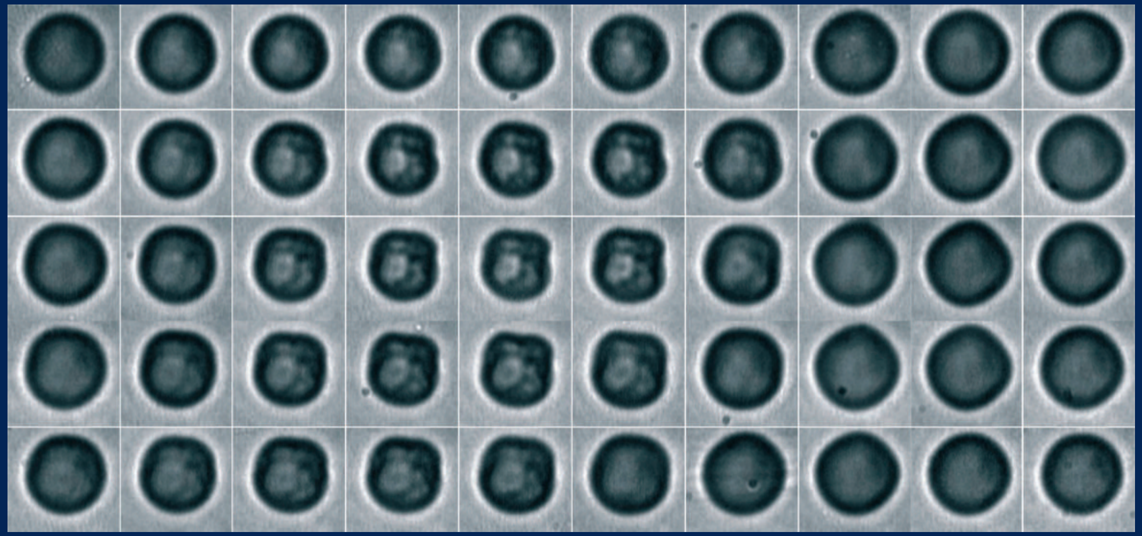

Jeroen Sijl

Uitnodiging

voor het bijwonen
van de verdediging
van mijn proefschrift
getiteld:

Ultrasound
Contrast Agents:
Optical and
Acoustical
Characterization

welke zal plaatsvinden
op woensdag 16
december 2009
om 11.00
collegezaal II
gebouw de Spiegel
Universiteit Twente,
Enschede

Voorafgaand aan de
verdediging zal ik om
10:45 een korte inleiding
geven over de inhoud
van het proefschrift.
Na afloop van de
promotieplechtigheid
zal er ter plaatse een
receptie zijn.

Jeroen Sijl
jeroensijl@gmail.com

Ultrasound Contrast Agents
Optical and Acoustical Characterization

Jeroen Sijl

Samenstelling promotiecommissie:

Prof. dr. ir. L. van Wijngaarden (voorzitter)	Universiteit Twente, TNW
Prof. dr. rer. nat. D. Lohse (promotor)	Universiteit Twente, TNW
Prof. dr. ir. N. de Jong (promotor)	Universiteit Twente, TNW
Dr. A.M. Versluis (assistent promotor)	Universiteit Twente, TNW
Prof. dr. ir. C.H. Slump	Universiteit Twente, EWI
Prof. dr. A.G.J.M. van Leeuwen	Universiteit Twente, TNW
Dr. ir. P.J.A. Frinking	Bracco Research S.A. Geneva
Prof. dr. M. Averkiou	University of Cyprus

The work in this thesis was carried out at the Physics of Fluids group of the Faculty of Science and Technology of the University of Twente.

Nederlandse titel:
Ultrageluid contrast vloeistoffen – Optische en acoustische karakterisatie

Publisher:
Jeroen Sijl, Physics of Fluids, University of Twente,
P.O. Box 217, 7500 AE Enschede, The Netherlands
pof.tnw.utwente.nl
Front cover illustration: Optical highspeed recording of a buckling microbubble (image analysis done by Timo Rozendal)
Backside illustration: Three dimensional representation of the Fourier transform of the subharmonic oscillations of a 3.8 μm phospholipid coated microbubble as a response to different driving pressures with different frequencies around two times the resonance frequency of the bubble: Experiment (top) and Theory (bottom) [Chapter 4 of this thesis].
Print: Gildeprint Drukkerijen B.V.

ISBN 978-90-365-2951-8

ULTRASOUND CONTRAST AGENTS: OPTICAL AND ACOUSTICAL CHARACTERIZATION

PROEFSCHRIFT

ter verkrijging van
de graad van doctor aan de Universiteit Twente,
op gezag van de rector magnificus,
prof. dr. H. Brinksma,
volgens besluit van het College voor Promoties
in het openbaar te verdedigen
op woensdag 16 december 2009 om 11.00 uur

door

Jeroen Sijl

geboren op 13 November 1980

te Laren (NH)

Dit proefschrift is goedgekeurd door de promotoren:
Prof. dr. rer. nat. D. Lohse
Prof. dr. ir. N. de Jong
en de assistent-promotor:
Dr. A.M. Versluis

Contents

1

Introduction

Already for decennia the interaction between sound and bubbles has provided research with an apparent unlimited source of fascinating phenomena to be understood and described. In 1917, Lord Rayleigh got intrigued by the sound of boiling water which was hypothesized to result from collapsing bubbles [1]. His theoretical description of the collapse of an empty cavity in an infinite liquid medium is still extensively used today [1]. In like manner fascinated by the sound of running water, Minnaert in 1933, derived a formula for the resonance frequency of an oscillating bubble [2]. He showed that the musical sound of running water primarily results from resonant oscillating bubbles entrained in the flow. Likewise, when listening to the sound of rain falling on a pond or the sound of the surf in the sea, one hears the resonance frequencies of many entrained air bubble's all singing together.

Another trigger was given to the research on bubbles and sound in 1989 when Felipe Gaitan observed something extraordinary for an oscillating single bubble driven with a continuous (20 kHz) sinusoidal sound wave [3]. For low gas concentration in the liquid and a large driving pressure amplitude, Gaitan observed that a strongly pulsating single bubble (with an initial bubble radius of around 20 μm) can emit light visible to the naked eye; "with the room lights dimmed, a greenish luminous spot the size of a pinpoint could be seen with the unaided eye, near the bubble's position in the liquid" [3]. Though, luminescence from multiple cavitating bubbles was not new and especially in the field of cavitation studied before [4–8], it was never observed to come from a single bubble and to be controllable. A complete understanding of what is referred to as single-bubble sonoluminescence was provided ten years later in 2002 as reviewed in [9]. In the search for this explanation, the interaction between ultrasound and bubbles gained a lot of scientific, media, industrial and even governmental attention. The attention was not surprising since the emitted light resulted from an extreme focussing of energy which occurred when the bubble with an initial bubble radius of around 5 μm collapsed very rapidly from its maximum radius of 50 μm to a minimum radius of 0.5 μm. It was hypothesized that by upscaling this process controllable nuclear fusion was possible. Although it was ascertained in 2002 that this energy focus was not sufficient to enable nuclear fusion, the beauty of this tiny source of light remains intriguing.

Beside the scientific fascinating nature of the interaction between sound and bubbles, it also has a large variety of industrial and medical applications. Already in the time of Rayleigh, screw-propellers were known to be damaged by collapsing bubbles. This damage, also referred to as cavitation damage, nowadays still provides science and industry with a motivation to investigate bubble dynamics. In the past decennia sound has been shown to give a certain amount of control over cavitation. Some authors have shown that if the gas concentration and contamination and cavitation nuclei are also controlled, ultrasound can be used to produce perfect reproducible and predictable cavitation [10].

In the semiconductor industry ultrasonically induced cavitating bubbles are created on purpose and used to clean micro- and nano-sized structures [11, 12]. On a larger scale but in a similar fashion cavitating clouds of bubbles are used in an ultrasonic bath to clean surgical tools, engine parts or even fabrics [13–15]. In a medical setting, extracorporeal lithotripsy, uses cavitating clouds of bubbles created by a focussed shockwave to break kidney stones.

This finally brings us to the subject of this thesis where microbubbles in a less violent manner interacting with ultrasound are studied for the application of contrast-enhanced ultrasound imaging. In contrast-enhanced ultrasound imaging, microbubbles coated with a phospholipid or albumin shell are injected intravenously into the blood stream. A non-linear interaction between the ultrasound and the encapsulated microbubbles generates a specific acoustic signature that can be used to distinguish the bubble form the surrounding tissue and enhance the contrast in for example ultrasound imaging of the myocardial blood perfusion. The focus of this thesis is on the characterization of the small amplitude behavior of these phospholipid coated ultrasound contrast

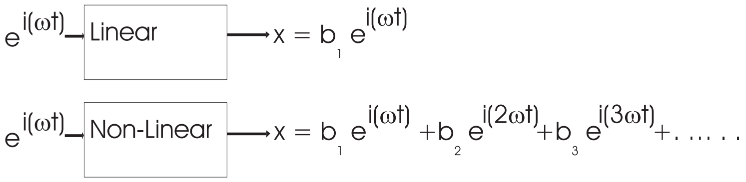

Figure 1.1: Schematic representation of the difference between a linear and a non-linear system

agent microbubbles to reveal the origin of this specific acoustic signature.

1.1 Non-linear bubble dynamics

The equation to describe bubble dynamics introduced by Lord Rayleigh in 1917 is by nature non-linear. Unlike for a linear system, the output of a non-linear system is not proportional to the input of the system. If a system is described by a function, f, such that the output, x, is related to the input a:

$$x = f(a). \tag{1.1}$$

In general f can be developed as a power series:

$$f = \sum b_n a^n. \tag{1.2}$$

where n is an integer and $b_n = B_n + iC_n$ is in general a complex number. Then, if we assume, a, is a harmonic function of t,

$$a = e^{i\omega t}, \tag{1.3}$$

then, in general, the output function x is described by,

$$x(t) = \sum b_n e^{i(n\omega t)}. \tag{1.4}$$

For a linear system $b_n = 0$ for all n except for $n = 1$, then, $b_1 = B_1 + iC_1$, where B_1 and C_1 are constants. For a non-linear system on the other hand B_n and C_n can have a value for all n. The non-linear behavior of bubbles is advantageous for the application of coated microbubbles as contrast agents for medical ultrasound imaging. If an ultrasound wave with a frequency ω is applied to a microbubble it will start to oscillate not only with the applied frequency ω but also with integer multiples of this applied frequency, 2ω, 3ω but also $(1/2)\omega$ and $(3/2)\omega$ as is shown in Fig. 1.2. In Fig. 1.2 we observe the acoustic response of a 4.9 μm radius phospholipid coated microbubble to an acoustic driving pressure pulse with an amplitude of 40 kPa and a frequency of 2.1 MHz. When the driving pressure pulse reaches the bubble it will start to oscillate as a response to the oscillating pressure field it is sensing. Then, as a result of the oscillations of the bubble wall an acoustic wave, which also contains non-linear harmonic components, will travel outward from the bubble. This acoustic wave can be picked up by a transducer and as shown in Fig. 1.2(b) contains many harmonics of the initially applied driving pressure pulse.

If phospholipid microbubbles are injected intravenously into the blood flow of a human body as is done in contrast-enhanced ultrasound imaging these non-linear harmonic bubble responses help to distinguish between blood flow and the surrounding tissue. The more non-linear the response of a microbubble the better it can be distinguished from the surrounding tissue which is considered a linear system. For contrast-enhanced ultrasound imaging it is therefore of primary importance to understand the origin of the non-linear behavior of phospholipid coated microbubbles.

For uncoated gas bubbles the origin of non-linearities are well understood and extensively described in the literature, see for example, [16–21]. Coated microbubbles on the other hand have been observed to behave differently and more non-lineary than free gas bubbles. Even so, the change in the linear/fundamental response of coated microbubbles and to some extent the change in the second harmonic response introduced by the coating can be accounted for by extensions to the models for uncoated bubbles, see [22–24]. However, the (phospholipid) coating has also been observed to introduce non-linearities which cannot not be accounted for nor understood by these models. Recordings with the Brandaris ultrahigh-speed camera for example have revealed that phospholipid coated microbubbles only start to vibrate, if excited with a driving pressure above a certain threshold pressure [25]. The origin of this behavior, termed “threshold behavior”, is still unclear. Another non-linearity specifically related to the bubble coating is referred to in the literature as “compression-only” behavior [26, 27]. For a bubble showing this behavior the bubble oscillations are non-symmetric with respect to the resting radius; the bubbles compress more than they expand. Finally, the subharmonic behaviour, i.e. the response at half the driving pressure frequency, $(1/2)\omega$, is also observed to be enhanced by the coating of a bubble [28–35]. In this thesis

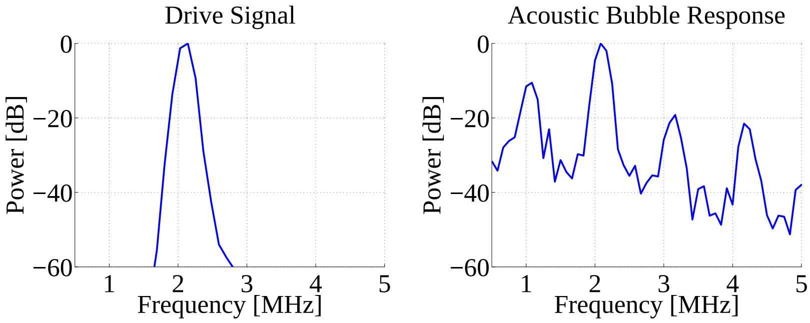

(a) (b)

Figure 1.2: An example of the non-linear behavior of a coated microbubble. An acoustic driving pressure pulse with an amplitude of 40 kPa of which the fourier transform is presented in (a), is send to a 4.9 μ*m radius phospholipid coated microbubble. In the acoustic response of the microbubble, presented in (b), we can identify four different harmonics,* 2ω*,* $(1/2)\omega$ *and* $(3/2)\omega$*, clearly demonstrating the strong non-linear character of the phospholipid coated microbubble system.*

we explain the origin of the latter two non-linearities for phospholipid coated microbubbles, i.e. "compression-only" behavior and enhanced subharmonic behavior. Hereto, experimental techniques to characterize and study the behavior of these micron sized bubbles oscillating with more than a million pulsations a second, is of fundamental importance. These experimental aspects of this study will therefore also comprise an extensive part of the thesis.

1.2 Origin of non-linearities

To understand the origin of the non-linear dynamics of oscillating bubbles it is insightful to compare the bubble dynamics as described by the equation introduced by Lord Rayleigh with the classical dynamical mass spring system [36]. A nowadays popular form of the equation introduced by Lord Rayleigh is:

$$\rho\left(R\ddot{R}+\frac{3}{2}\dot{R}^2\right)=(p_L(R)-p_\infty) \tag{1.5}$$

In this equation R, $\dot{R}$, and $\ddot{R}$ describe the radius, the velocity and the acceleration of the bubble wall, respectively. The density of the liquid is described by $\rho = 10^3$ kg/m^3 and the pressure difference is determined by the pressure in the liquid at the bubble wall, $p_L(R)$, and the pressure far from the bubble wall, p_∞. If we neglect viscosity and the vapor pressure inside the bubble and we assume the gas inside the bubble is correctly described by the polytropic ideal gas law, $P_g \propto R^{-3\gamma}$ where γ is the polytropic exponent we obtain:

$$p_L(R) = \left(P_0 + \frac{2\sigma}{R_0}\right)\left(\frac{R_0}{R}\right)^{3\gamma} - \frac{2\sigma}{R} \tag{1.6}$$

In this equation P_0 is the ambient pressure and σ the surface tension of the gas liquid interface. The pressure far from the bubble wall p_∞ is determined by the atmospheric pressure and the driving pressure $P_{drive} = -P_A e^{i\omega t}$.

$$p_\infty = -P_A e^{i\omega t} + P_0 \tag{1.7}$$

Inserting Eq. 1.6 and Eq. 1.7 into Eq. 1.5 the total equation becomes:

$$\rho\left(R\ddot{R} + \frac{3}{2}\dot{R}^2\right) = \left(P_0 + \frac{2\sigma}{R_0}\right)\left(\frac{R_0}{R}\right)^{3\gamma} - \frac{2\sigma}{R} - P_0 + P_A e^{i\omega t} \tag{1.8}$$

Equation 1.8 can be linearized by replacing R by $R_0 + x$ where we assume $x << R_0$. Rewriting the resulting equation and keeping only the terms of first order in x we obtain:

$$\ddot{x} + \omega_0^2 x = \frac{P_A}{\rho R_0} e^{i\omega t} \tag{1.9}$$

where ω_0 denotes the resonance frequency of the bubble as was already shown by Minnaert [2]

$$\omega_0^2 = \frac{1}{\rho R_0^2}\left[3\gamma\left(P_0 + \frac{2\sigma}{R_0}\right) - \frac{2\sigma}{R_0}\right] \tag{1.10}$$

This equation is identical to the differential equation of a driven harmonic oscillator/mass spring system with spring constant k and mass m, where x in this case denotes a deviation from the equilibrium position of the mass:

$$m\ddot{x} + kx = Fe^{i\omega t}. \tag{1.11}$$

In analogy with the mass spring system, the mass of the uncoated bubble system is determined by the surrounding liquid and can be obtained by determining the kinetic energy of the oscillating bubble/liquid system. The velocity of the liquid at the bubble wall is equal to $\dot{R}$. Far from the bubble wall, at a

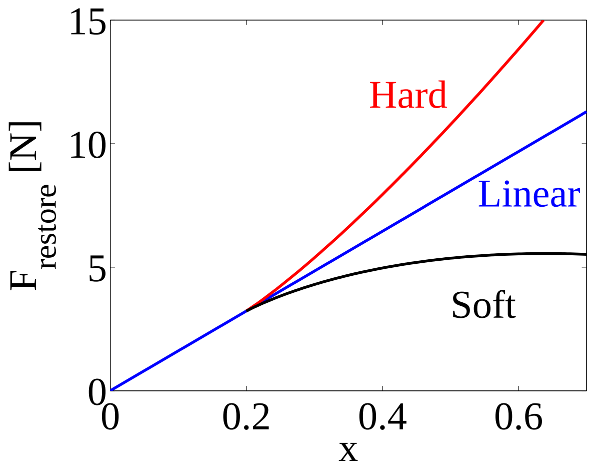

Figure 1.3: For a linear system the restoring force increases linearly with distance, x*, the system is away from equilibrium. For a non-linear system the relation between the restoring force and* x *deviates from linear. For a "hard" system the restoring force increases more than linear with* x*, for a "soft" system the opposite is true.*

distance r, the velocity of the liquid v_r is determined by the conservation of mass:

$$R^2\dot{R} = r^2 v_r. \tag{1.12}$$

The total kinetic energy of the oscillating surrounding liquid is determined by the integral:

$$E_{\text{kinetic}} = \frac{1}{2}\rho\int_{R_0}^{\infty} v_r^2 4\pi r^2 dr = 2\pi\rho\dot{R}^2{R_0}^3. \tag{1.13}$$

Therefore we can conclude that the mass of the oscillating bubble system can be described by $m = 4\pi\rho R_0^3$, where ρ is the liquid density, and R_0 the initial bubble radius. By comparing Eq. 1.9 and Eq. 1.11 we can show the restoring force of the uncoated bubble system is provided by the surface tension and the gas inside the bubble, according to $k = {\omega_0}^2 m = 4\pi R_0[3P_0\gamma + 2(3\gamma - 1)\sigma/R_0]$. For a perfectly linear system, like a mass spring system, with a constant k, the restoring force of the system increases linearly with oscillation amplitude of the system $F_{\text{restore}} = kx$. However, for larger amplitudes of oscillation many systems become non-linear and the restoring force of the system does no longer increase linearly with oscillation amplitude. For a "soft system" the gradient between the restoring force and the amplitude of oscillation decreases for larger amplitude and for a ”hard system” the opposite happens as shown in Fig. 1.3. The more non-linear the system the faster the linear relation between the restoring force and oscillation amplitude breaks down. For an uncoated bubble the restoring force results from the surface tension σ and the expanded or compressed gas inside the bubble described by the polytropic exponent γ. It can be shown that an oscillating bubble is a ”soft” system [18], and for larger amplitudes of oscillation the restoring force does no longer increase linearly with x. A phospholipid coated bubble is observed to behave even more non-lineary than a free gas bubble and the linear relation between the restoring force and oscillation amplitude is expected to break down for even smaller x. In order to understand this difference between a coated and an uncoated bubble and to explain the non-linearities discussed in the previous section we should therefore investigate the difference between the restoring force of a coated and an uncoated bubble. Since the gas inside a coated and an uncoated bubble is expected to behave similarly the key to the origin of a difference in non-linear behavior between the two types of bubbles should be in the surface tension. A major part of this thesis will therefore deal with the effect of changes of the surface tension introduced by the (phospholipid) coating of microbubbles and the effect this has on the dynamics of the bubbles.

1.3 Guide through the thesis

In this introduction it has become clear that to fully characterize the interaction of ultrasound with coated microbubbles the focus should be on the small amplitude behavior of these bubbles. The amplitude of oscillation of the bubbles should be small enough to reveal the transition from a linear system into a non-linear system. Only in this way one can fully understand the origins of the non-linearities introduced by the coating.

Clearly, this requirement puts stringent demands on the experimental techniques one can explore. In Ch. 2 we will show how acoustical techniques provide a good way to characterize the small amplitude behavior of acoustically driven phospholipid coated microbubbles. In Ch. 3 and in Ch. 4 we will explore optical ultra-high speed imaging to reveal the effect of a phospholipid coating on the non-linear “compression-only” and subharmonic behavior of ultrasound contrast agent microbubbles. In Ch. 5 we combine the acoustical techniques presented in Ch. 2 and the ultra-high speed imaging explored in

Ch. 3 and Ch. 4 and show how both techniques complement each other in the research and exploration of the non-linear nature of the dynamics and the resulting acoustic signature of ultrasound contrast agents for medical imaging purposes. Finally, the conclusions and an outlook are presented in Ch. 6

References

[1] L. Rayleigh, “On the pressure development in a liquid during the collapse of a spherical cavity”, Philos. Mag. **32 (S8)**, 94 – 98 (1917).

[2] M. Minnaert, “On musical air bubbles and the sound of running water”, Philos. Mag. **32 (S16)**, 235 – 248 (1933).

[3] D. F. Gaitan, L. A. Crum, C. C. Church, and R. A. Roy, “Sonoluminescence and bubble dynamics for a single, stable, cavitation bubble”, J. Acoust. Soc. Am. **91**, 3166–3183 (1992).

[4] F. B. Peterson, “Light emission from hydrodynamic cavitation”, PhD thesis, Northwestern University, USA (1966).

[5] F. B. Peterson, “Monitoring hydrodynamic cavitation light emission as a means to study cavitation phenomena”, Proc. Symp. on Testing Techniques in Ship Cavitation Research Trondheim, Norway (1967).

[6] J. H. J. van der Meulen, “The use of luminescence as a measure of hydrodynamic cavitation activity”, ASME Cavitation and Multiphase Flow Forum, Houston 55 – 53 (1983).

[7] J. H. J. van der Meulen, “On correlating erosion and luminescence from cavitation on a hydrofoil”, Intl Symp. on Propellers and Cavitation, Edinburgh 13 – 19 (1986).

[8] R. E. A. Arndt, “Cavitation in vortical flows”, Annu. Rev. Fluid Mech. **34**, 143 –175 (2002).

[9] M. P. Brenner, S. Hilgenfeldt, and D. Lohse, “Single-bubble sonoluminescence”, Rev. Mod. Phys. **74**, 425 – 483 (2002).

[10] N. Bremond, M. Arora, S. M. Dammer, and D. Lohse, “Interaction of cavitation bubbles on a wall”, Phys. Fluids **18**, 121505–10 (2006).

[11] G. W. Gale and A. A. Busnaina, “Removel of particulate contaminants using ultrasonics and megasonics: A review”, Part. Sci. Technol. **13**, 197 (1995).

[12] F. Holsteyns, “Ph.d. thesis”, K.U. Leuven, Belgium (2008).

[13] D. Krefting and W. Lauterborn, “High-speed observation of acoustic cavitation erosion in multibubble systems”, Phys. Fluids **11**, 119 (2004).

[14] C. D. Ohl, M. Arora, R. Dijkink, V. Janve, and D. Lohse, “Surface cleaning from laser-induced cavitation bubbles”, Appl. Phys. Lett. **89**, 74102 (2006).

[15] V. S. Moholkar, M. M. C. G. Warmoeskerken, C. D. Ohl, and A. Prosperetti, “Mechanism of mass-transfer enhancement in textiels by ultrasound”, AIChEJ **50**, 58 (2004).

[16] A. Eller and H. G. Flynn, “Generation of subharmonics of order one-half by bubbles in a sound field”, J. Acoust. Soc. Am. **46**, 722–727 (1969).

[17] A. Eller, “Subharmonic response of bubbles to underwater sound”, J. Acoust. Soc. Am. **55**, 871–873 (1974).

[18] A. Prosperetti, “Nonlinear oscillations of gas bubbles in liquids: steady-state solutions”, J. Acoust. Soc. Am. **56**, 878–885 (1974).

[19] A. Prosperetti, “Nonlinear oscillations of gas bubbles in liquids. Transient solutions and the connection between subharmonic signal and cavitation”, J. Acoust. Soc. Am. **57**, 810–821 (1975).

[20] W. Lauterborn, “Numerical investigation of nonlinear oscillations of gas bubbles in liquids”, J. Acoust. Soc. Am. **59**, 283–293 (1976).

[21] M. S. Plesset and A. Prosperetti, “Bubble dynamics and cavitation”, Annu. Rev. Fluid Mech. **9**, 145–85 (1977).

[22] N. de Jong and L. Hoff, “Ultrasound scattering properties of albunex microspheres”, Ultrasonics **31** (1993).

[23] C. C. Church, “The effect of an elastic solid surface layer on the radial pulsations of gas bubbles”, J. Acoust. Soc. Am. **97**, 1510 – 1521 (1995).

[24] K. Sarkar, W. T. Shi, D. Chatterjee, and F. Forsberg, “Characterization of ultrasound contrast microbubbles using in vitro experiments and viscous and viscoelastic interface models for encapsulation”, J. Acoust. Soc. Am. **118**, 539–550 (2005).

[25] M. Emmer, A. van Wamel, D. E. Goertz, and N. de Jong, “The onset of microbubble vibration”, Ultrasound Med. Biol. **33**, 941–949 (2007).

[26] P. Marmottant, S. van der Meer, M. Emmer, M. Versluis, N. de Jong, S. Hilgenfeldt, and D. Lohse, “A model for large amplitude oscillations of coated bubbles accounting for buckling and rupture”, J. Acoust. Soc. Am. **118**, 3499 – 3505 (2005).

[27] N. de Jong, M. Emmer, C. T. Chin, A. Bouakaz, F. Mastik, D. Lohse, and M. Versluis, ““Compression-Only” behavior of phospholipid-coated contrast bubbles”, Ultrasound Med. Biol. **33** (2007).

[28] O. Lotsberg, J. M. Hovem, and B. Aksum, “Experimental observation of subharmonic oscillations in infoson bubbles”, J. Acoust. Soc. Am. **99**, 1366–1369 (1996).

[29] P. M. Shankar, P. D. Krishna, and V. L. Newhouse, “Advantages of subharmonic over second harmonic backscatter for contrast-to-tissue echo enhancement”, Ultrasound Med. Biol. **24**, 395–399 (1998).

[30] P. M. Shankar, P. D. Krishna, and V. L. Newhouse, “Subharmonic backscattering from ultrasound contrast agents”, J. Acoust. Soc. Am. **106**, 2104–2110 (1999).

[31] P. D. Krishna, P. M. Shankar, and V. L. Newhouse, “Subharmonic generation from ultrasonic contrast agents”, Phys. Med. Biol. **44**, 681–694 (1999).

[32] P. H. Chang, K. K. Shung, S. Wu, and H. B. Levene, “Second harmonic imaging and harmonic doppler measurements with albunex”, IEEE Trans. Ultrason. Ferroelect. Freq. Contr. **42**, 1020–1027 (1995).

[33] E. Biagi, L. Breschi, E. Vannacci, and L. A. Masotti, “Stable and transient subharmonic emissions from isolated contrast agent microbubbles”, IEEE Trans. Ultrason. Ferroelect. Freq. Contr. **54**, 480–497 (2007).

[34] P. J. A. Frinking and N. de Jong, “Subharmonic imaging”, in *Fourth Annual Ultrasound Contrast Research Symposium in Radiology* (San Diego, USA) (1999).

[35] P. J. A. Frinking, E. Gaud, J. Brochot, and M. Arditi, “Subharmonic scattering of phospholipid-shell microbubbles at low acoustic pressure amplitudes”, submitted to IEEE Trans. Ultrason. Ferroelec. Freq. Contr. (2009).

[36] T. G. Leighton, *The acoustic bubble (Academic, London, 1994)*.

2

Acoustic characterization of single ultrasound contrast agent microbubbles[‡]

Individual ultrasound contrast agent microbubbles (BR14) were characterized acoustically. The bubbles were excited at a frequency of 2 MHz and at peak-negative pressure amplitudes of 60 and 100 kPa. By measuring the transmit and receive transfer functions of both the transmit and receive transducers, echoes of individual bubbles were recorded quantitatively and compared to simulated data. At 100 kPa driving pressure, a second harmonic response was observed for bubbles with a size close to their resonance size. Power spectra were derived from the echo waveforms of bubbles of different sizes. These spectra were in good agreement with those calculated from a Rayleigh Plesset-type model, incorporating the viscoelastic properties of the phospholipid shell. Small bubbles excited below their resonance frequency have a response dominated by the characteristics of their phospholipid shell, whereas larger bubbles, excited above resonance, have a response identical to those of uncoated bubbles of similar size.

[‡] Published as: Jeroen Sijl, Emmanuel Gaud, Peter. J.A. Frinking, Marcel Arditi, Nico de Jong, Michel Versluis and Detlef Lohse, "Acoustic characterization of single ultrasound contrast agent microbubbles", Journal of the Acoustical Society of America **124**(6). 4091-4097 (2008).

2.1 Introduction

Ultrasound is the most widely used medical imaging method. It is capable of providing real-time information of tissue structure and blood flow in larger vessels. In smaller vessels and capillaries, however, blood flow detection is limited by the low flow velocities in combination with a low scattering efficiency of red blood cells, tissue motion artifacts, and the limited resolution of the applied ultrasound, which is, typically, on the order of 0.5 mm. Ultrasound contrast agents (UCAs), have been proposed and are successfully used for the assessment of tissue perfusion. UCAs consist of micron-sized bubbles with a size distribution around a typical mean size of 2-3 µm. The microbubbles have an air or inert-gas core and are coated with a thin protein, lipid or polymer layer. Such microbubbles are efficient scatterers of ultrasound and have a scattering cross section, which is several orders of magnitude higher than that of red blood cells. Therefore, blood flow at the microvascular level can be measured after an intravenous injection of an UCA, e.g., to image tissue perfusion in liver, kidney, and the myocardium.

There is an increasing interest in the development of sophisticated ultrasound contrast imaging techniques exploiting bubble-specific signatures. Therefore, current studies are focused on a quantitative description of the behavior of UCA microbubbles in an ultrasound field. Numerous studies have been performed in the past on bubble populations with known size distributions, in which experimentally obtained attenuation spectra were fitted to modeled spectra [1–4] to determine the shell properties of the bubbles. However, Gorce *et al.* [3] suggested, by considering fractions of the native size distribution of the contrast agent SonoVue®, that the shell properties of the bubbles are actually size dependent. Moreover, bubble-bubble interactions were not taken into account, although they could play an important role. Both of these problems could be overcome by studying and characterizing the response of *individual* contrast agent microbubbles to ultrasound.

Several authors have shown that high-speed optical recordings provide quantitative information on the dynamic behavior of single microbubbles in an ultrasound field [5–8]. Moreover, high-speed imaging has revealed new phenomena that were not observed before, such as “compression-only” behavior [9, 10], ”thresholding” behavior [11] and the occurrence of surface modes [12] and non-spherical oscillations [13, 14]. However, high-speed imaging of bubble dynamics has some disadvantages. Besides being costly and of limited availability, these studies are unable to detect small radial displacements

($<$ 30 nm) at low acoustic pressure amplitudes (on the order of 20 kPa), due to the limited resolving power of the optical system($<$ 30 nm) [11]. In addition, optical measurements give quantitative information on the amplitude of oscillation of the microbubble, but they provide no direct measurements of the ultrasound waves scattered by these microbubbles, which are important for their characterization in medical applications. Also, optical observations are less sensitive than acoustic measurements at detecting second and higher harmonic components. Finally, *in vivo* optical measurement of the dynamics of microbubbles is extremely difficult, although feasible [15]. For all these reasons, quantitative acoustic measurements of single ultrasound contrast agent microbubbles provide valuable information for their characterization.

Recent *in vitro* studies have demonstrated that single bubble responses can be measured acoustically [16–19]. There are, however, three main difficulties associated with single bubble measurements. First, it is difficult to isolate single microbubbles within an ultrasound beam, which is required to ensure that the measured response originates from one bubble only. Second, to prevent bubble destruction and to operate in the linear regime, the measurements should be performed at low acoustic driving pressure amplitudes, which puts stringent requirements on the sensitivity of the receiving transducer. Finally, to quantify the size-dependent shell properties, the corresponding initial bubble radius should be measured accurately. To our knowledge, the work reported here is the first time all three challenges are successfully addressed.

Acoustic responses of single UCA microbubbles were measured at low pressure amplitudes using a highly sensitive calibrated receive transducer. The bubbles were isolated in a capillary tube and their resting radii were determined by optical means. The measured bubble responses were analyzed and compared to numerical simulations using a RayleighPlesset-type equation, incorporating the viscoelastic properties of the phospholipid shell. [9].

2.2 Experimental Setup

The experimental setup is shown in Fig. 2.1. It comprises of two 1 in. diameter transducers. A focused 2.25 MHz center frequency transducer (Panametrics V304, Waltham, MA) was used as a transmitter, and a second broadband focused transducer (3 MHz, 100 % -6 dB relative bandwidth, M3, W1001, Vermon SA, Tours, France) was used as a receiver. A 500 μm diameter zirconia/silica alignment bead glued onto a 140 μm nylon fishing wire was positioned at the center of the field of view of a microscope objective.

Both transducers were confocally aligned using the alignment bead at a focal distance of 75 mm, at an angle of 100° to one another and at an angle of 50° to the capillary tube to avoid any specular reflection. The bubbles were confined in a 200 μm diameter cellulose capillary tube with an 8-μm wall thickness (Product No. 132294, Spectrum Europe, Breda, The Netherlands), occupying the exact position of the alignment bead after its removal. This then ensures that any bubble positioned at the center of the field of view of the microscope objective was also precisely positioned in the confocal region of the transducers. The transmit transducer was excited by a 2 MHz, 5 cycle Hanning-windowed sinusoidal burst, which was generated by an arbitrary waveform generator (Tabor Electronics Ltd, Model 8024, Haifa, Israel) and amplified by a power amplifier (ENI, Model A150 with 50 Ω input impedance, Rochester, NY). The peak-negative pressure amplitudes were determined from the excitation waveforms which were measured at the focus of the transmit transducer using a calibrated membrane hydrophone (MH0415, Precision Acoustic Ltd., Dorset, UK) as shown in Fig. 2.2. The received bubble echoes were amplified by the preamplifier part of a pulser/receiver (Panametrics, Model 5900 PR, Waltham, MA) and digitized (9 bit box averaged four times at 100 MHz) by a digital oscilloscope (Yokogawa Electric Corp., Model DL 1740, 50 Ω input impedance, Tokyo, Japan).

The two transducers and the capillary tube were mounted in a water tank that was made to fit onto the translation stage of an inverted microscope (IX50, Olympus Optical, Japan). The microscope objective lens (Olympus Plan Fluorite, 40x, N.A. 0.55, SLCPLFL, Product No. 37471) was focused on the confocal area of the two transducers.The objective lens had two functions. First, it was used in combination with the translation stage of the microscope to scan the acoustic focal area to verify that only one single bubble was present. Second, it was used to determine the resting radius of the bubble by imaging it onto a Peltier-cooled charge coupled device camera F-View II, 1376 x 1032 pixels, pixel size 6.45 x 6.45 μm^2, Soft Imaging System GmbH, Münster, Germany). The flow of UCA bubbles through the capillary tube was controlled by a peristaltic pump (Dynamax, Model RP-1, U.S.A, Emeryville, CA).

2.2.1 Single Bubbles

One key aspect of the experimental setup is the capability to isolate single bubbles in the ultrasound beam. The experimental agent BR14, which con-

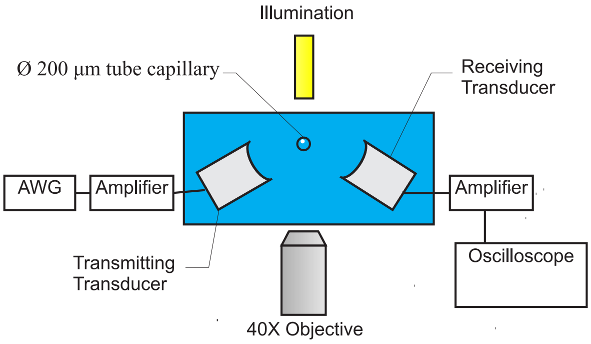

Figure 2.1: The experimental setup used for measuring single bubble responses. Contrast bubbles are located inside a capillary tube, placed perpendicular to the plane of the figure. The driving pressure waveform produced by an AWG was amplified and transmitted by a focused transducer. The echo responses of the bubbles were received by a second focused transducer.

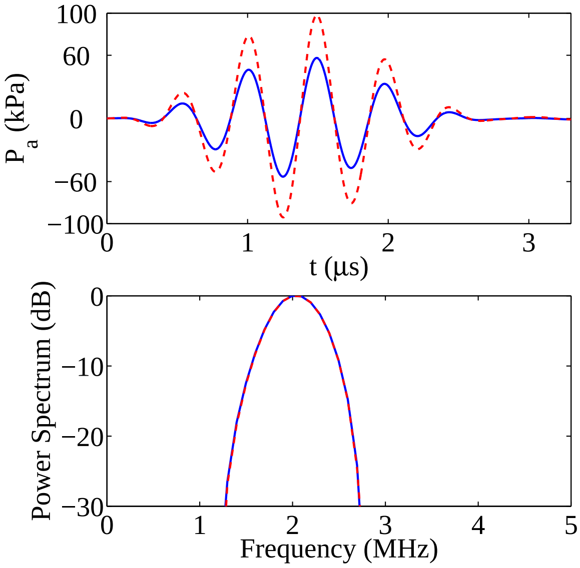

Figure 2.2: The excitation pressure waveforms $P_a(t)$*, as measured with a calibrated membrane hydrophone at the focus of the transmit transducer (top) and corresponding calculated power spectra (bottom). Both the 60-kPa and the 100-kPa peak-negative pressure pulses are presented by the solid blue line and the dashed red line, respectively*

tains microbubbles with a phospholipid shell and a perfluorocarbon-gas core (Bracco Research S.A., Geneva, Switzerland), were used in the experiments at a dilution of 1: 10 000 (i.e. 25 000 bubbles/ml). This high dilution ratio corresponds to having statistically only one bubble in the effective insonified volume (0.04 μl). Within the capillary tube, this corresponds to a statistical average distance of 1.5 mm between two subsequent bubbles. The suspension was first decanted to filter out the smaller bubbles (< 2 μm in order to ensure that all the bubbles present in the capillary tube could be optically detected. As a result, 80% of the bubbles in the suspension had a radius larger than 2 μm, as was measured with a Multisizer 3 Coulter Counter (Beckman-Coulter Inc., Miami, FL). The other advantage of using a filtered set of bubbles is that the larger bubbles rise faster to the upper wall of the capillary tube (after the pump was stopped). Consequently, only the upper wall of the capillary tube needed to be scanned to ensure that there was indeed only one single bubble present within the acoustic focal area.

2.2.2 Transducer transfer function

To allow for a quantitative study of the acoustic response of single bubbles, the transfer function of the receive transducer was measured, as described in the Appendix 2.6. The receive transfer function acts as a filter, determining the signal ultimately recorded by the oscilloscope. Therefore, all comparisons between the experimentally recorded signals and the modeled signals were performed with the latter first convolved with the receive transfer function.

2.2.3 Data analysis

The acoustic responses of 77 single bubbles with sizes between 1.5 μm and 5.0 μm were investigated; 35 of the bubbles were insonified with a peak-negative pressure amplitude of 60 kPa and 42 with a peak-negative pressure amplitude of 100 kPa. Sets of 20 successive acoustic responses were recorded for each bubble, with manual triggering at approximately 3 s intervals. Bubble images were recorded with the microscope before and after every five insonifications, to check whether they remained intact, i.e., whether they did not change in size due to shell rupture or possible ultrasound-driven gas dissolution. The acoustic responses and the images were stored on a personal computer, and all data were postprocessed using MATLAB (The Mathworks, Natick, MA). For each bubble, the 20 acoustic responses were digitally filtered (fourth order Butterworth bandpass filter (0.756 MHz)) to reduce electronic noise. Before averaging, the successive responses were time aligned to correct for possible jitter and small lateral displacements of the bubble in the capillary tube during insonification by maximizing the cross-correlation function.

2.3 Experimental Results

Fig. 2.3 shows a typical example of a single bubble response measured at an excitation pressure of 100 kPa. The left column of the figure displays the acoustic response as a function of time for bubbles with initial bubble radii of R_0 = 4.6 µm, 2.1 µm, and 1.5 µm, respectively. The right column of the figure displays the power spectra of the corresponding bubble echoes. It can be seen that the acoustic response for the smallest bubble, which is excited below its resonance frequency, is about 25 dB lower than the response measured for the bubble with the initial bubble radius of 4.6 µm. The bubble with an initial bubble radius of R_0 = 2.1 µm (middle panel in Fig. 2.3) is excited close to its resonance frequency, which is confirmed by the presence of substantial second harmonic components in its power spectrum. Note that the bubble echo amplitudes presented in the figure are absolute pressures in Pascal at the face of the receive transducer. The resonant behavior of the microbubbles is even more evident in Fig. 2.4. Here, the scattered power is displayed in color coded surface spectrograms as a function of both the bubble radius and the frequency. The response of bubbles with a similar size i.e., with a difference in radius smaller than the error in the measured radius (+/- 0.1 µm), are averaged. This resulted in 12 responses of differently sized bubbles at a driving pressure of 60 kPa (Fig. 2.4(a)) and 17 responses of differently sized bubbles at a driving pressure of 100 kPa (Fig. 2.4(b)). The color scale for both figures is normalized to the maximum scattered power at 100 kPa.
Figure 2.4(a) shows that at a driving frequency of 2 MHz, the measured echo power increases for increasing bubble size and increases strongly for bubbles with an initial radius around 2 µm. The second harmonic component (around 4 MHz) was not observed, except for very weak responses for bubbles around 1.8 µm. In Fig. 2.4(b), the scattered power also increases strongly for bubbles with an initial bubble radius around 2 µm, and a second-harmonic component is clearly visible for bubbles around that same size. These observations are in agreement with the scattering theory, which predicts that, in the fundamental

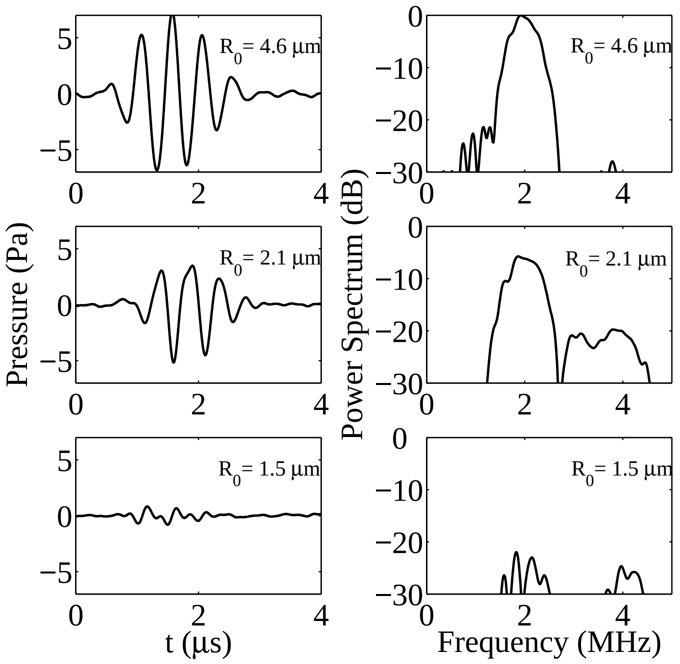

Figure 2.3: Measured acoustic responses of three single bubbles of different sizes excited with a driving pressure of 100 kPa. The response amplitude decreases with decreasing bubble radius. Furthermore, the second harmonic response is highest for the bubble closest to resonance size, i.e. $R_0 = 2.1$ *µm.*

band, a measurable response is expected for a wide range of bubble sizes, around and above their resonance. In the second harmonic band, however, only bubbles with a size near their resonance size are expected to contribute to a second harmonic response [20].

2.4 Modeling

The experimental dataset was compared with bubble dynamics modeling predicted by the model described by Marmottant *et al.*[9], which takes into account the influence of the phospholipid shell on the bubble dynamics. This coated bubble model is comparable to previous models used for ultrasound contrast agents [1, 4, 21, 22] in the sense that a RayleighPlesset-type equation is extended to include two or more so-called shell parameters. The parame-

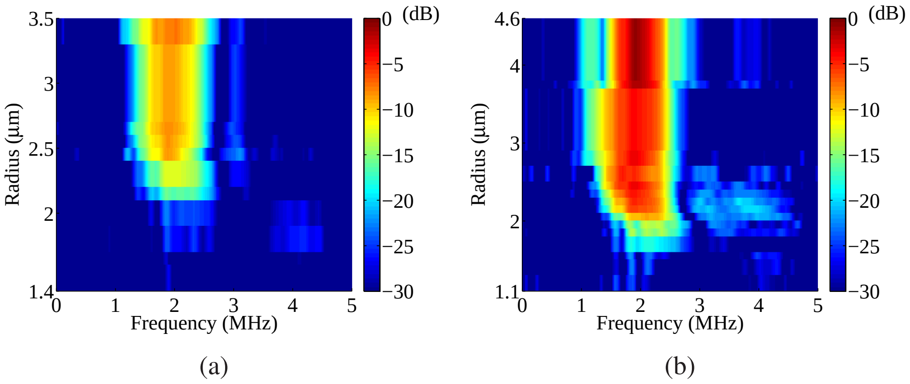

(a) (b)

Figure 2.4: Measured scattered power as a function of both radius (y-axis) and frequency (x-axis) for bubbles excited at 2 MHz and driving pressure amplitudes of 60 kPa (a) and 100 kPa (b). The data are normalized to the maximum measured scattered power at the 100 kPa driving pressure.

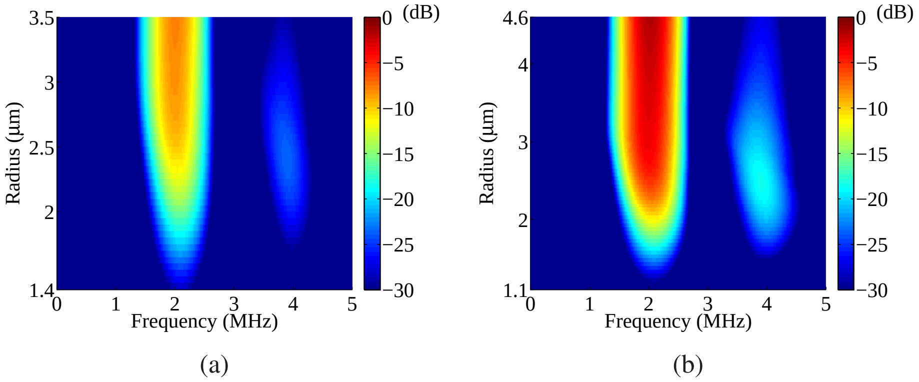

(a) (b)

Figure 2.5: Simulated scattered power as a function of both radius (y-axis) and frequency (x-axis) for bubbles excited at 2 MHz and driving pressure amplitudes of 60 kPa (a) and 100 kPa (b). The data are normalized to the maximum measured scattered power at the 100 kPa driving pressure, just as in Fig. 2.4, so that an absolute comparison with the measured data is possible.

ters describing the viscoelastic behavior of the shell are the shell elasticity χ and the shell viscosity κ_s. In the model used here, an effective surface tension is introduced. The effect of the shell elasticity is limited to small bubble oscillations, which is termed the elastic regime. In the compression phase, the effective surface tension is assumed to be zero as the phospholipid concentration is high and the bubble is likely to buckle. On the other hand, for large bubble expansions, the coating may be ruptured and the phospholipid molecules may be separated.

Thus, the gas core is in direct contact with the surrounding liquid and the effective surface tension is taken as that of the gas/water interface. The values for the shell elasticity $\chi = 0.54$ N/m and shell viscosity $\kappa_s = 2 \cdot 10^{-8}$ kg/s are those for BR14 from van der Meer *et al.* [8] and are in good agreement with values found elsewhere in literature [3, 9]. The effect of the shell on the bubble dynamics as modeled by Marmottant Marmottant *et al.* is most pronounced for bubbles oscillating around resonance. In this regime, the resonance radius is shifted by the shell elasticity while the shell viscosity decreases the amplitude of the bubble oscillations, strongly affecting the acoustic response of the bubble. Finally, we used the experimentally recorded driving pulses $P_a(t)$, shown in Fig. 2.2, as input into the RayleighPlessettype model. The equation is solved to give the radial dynamics of the bubble, $R(t)$. The first and second time derivatives $\dot{R}(t)$ and $\ddot{R}(t)$ are used to predict the scattered pressure waveform $P_s(r,t)$ [23]:

$$P_s(r,t) = \left(\frac{\rho(R(t)^2\ddot{R}(t) + 2R(t)\dot{R}(t)^2)}{r} \right) \tag{2.1}$$

where r denotes the distance from the bubble to the receiving transducer which is equal to the focal distance of the transducer in the present work.

The responses calculated with the model proposed by Marmottant *et al.*[9] are presented in Fig. 2.5. Here, the scattered power is displayed in the *same* color coding as in Fig. 2.4, as a function of both the bubble radius and the frequency, i.e. the color scale for both figures is normalized to the maximum *measured* scattered power at 100 kPa used in Fig. 2.4, allowing an absolute comparison with the measured data. A very good agreement may be observed between the measured and modeled scattered power, in particular around the fundamental frequency, for bubbles of all sizes, i.e. with radii both smaller and larger than the resonance radius. Second harmonic components may be recognized in the experimental data of Fig. 2.4, although not as clearly as expected from the simulated data of Fig. 2.5. The reason for the discrepancy is that the expected second harmonic amplitudes are close to the noise level of our experimental setup. To allow for a comparison in the second harmonic frequency range, a solution could be to increase the driving pressure amplitude to bring the second harmonic response well above the noise level. However, this was beyond the scope of the present work.

Figure 2.6 illustrates a direct comparison between the modeled and measured scattered power at the fundamental frequency, as a function of the initial bubble radius. The graphs in Fig. 2.6 are thus one-dimensional representations of the color surface plots of Fig. 2.4 and Fig. 2.5, i.e. vertical "slices" at frequencies around 2 MHz. The scattered power at the fundamental frequency was calculated by averaging the power in the 6 dB bandwidth around the maximum at 2 MHz. The modeled and experimental data are normalized to the maximum scattered power at 100 kPa, corresponding to an absolute scattered pressure amplitude of 7 Pa; this allows a direct quantitative comparison between the experimental and the modeled data. Figure 2.6(a) shows the data at a driving pressure of 60 kPa and Fig. 2.6(b) shows the data at a driving pressure of 100 kPa. In addition, the graphs of Fig. 2.6 also represent simulated results for bubbles without shell terms, i.e. free gas bubbles [24].

Excellent agreement was found between the measured scattered power and the ones calculated with the model taking into account the effect of the shell, with the viscoelastic parameter values given above. In contrast, the free-bubble model is unable to represent correctly the acoustic responses of the smaller bubbles that oscillate near and below resonance [2]. However, it correctly describes the response of the larger bubbles in their inertial regime, because 2 MHz is a frequency significantly above their resonance frequencies. This indicates that for bubbles larger than the resonance size at a driving frequency of 2 MHz, the shell elasticity and shell viscosity have a negligible effect on the bubble dynamics [23, 25, 26]. In this situation, the bubble dynamics is determined predominantly by the inertia of the liquid surrounding the bubble, similar to the case of a harmonic oscillator driven above resonance [23]. The inertial forces are the same for bubbles with and without a shell [23, 25, 26].

For the smaller bubbles, the experimental data are in good agreement with the simulated data of the coated-bubble model. Around resonance, the bubble dynamics are substantially affected by the shell elasticity and viscosity. Shell viscosity leads to damping and, as can be inferred from Fig. 2.6, the scattered amplitude of the bubbles is lower than for bubbles without a shell. Furthermore, the shell elasticity shifts the resonance radius toward larger bubble sizes [2].

It is worth noting that despite the conceptual difference in the experimental methods, this observation is in agreement with the results presented by van der Meer *et al.* [8]. In the microbubble spectroscopy method described by van der Meer *et al.*, resonance curves are determined by recording the amplitude of the radial excursion of single bubbles as a function of the frequency of the driving pressure waveform. In the work presented here, the excitation pulse frequency is fixed, while the acoustical response is determined for varying initial bubble radii. Since the data of the scattered power presented here are in good agreement with those predicted using the RayleighPlesset-type model of Marmottant *et al.* [9] and the shell parameters determined by van der Meer *et al.*, the results presented here are consistent with those of van der Meer *et al.* [8]. Finally, comparing the 60 and 100 kPa data, a shift of the resonance size toward smaller bubble sizes can be observed. The fact that the resonance radius of a microbubble shifts to smaller radii for larger driving pressures is well known for non-linear harmonic systems and it has been predicted and observed for bubbles without a shell [27, 28]. Also, it has been observed in optical studies on ultrasound contrast agents but is still poorly understood for these types of bubbles [8, 12]. This interesting observation clearly deserves more detailed study in future work.

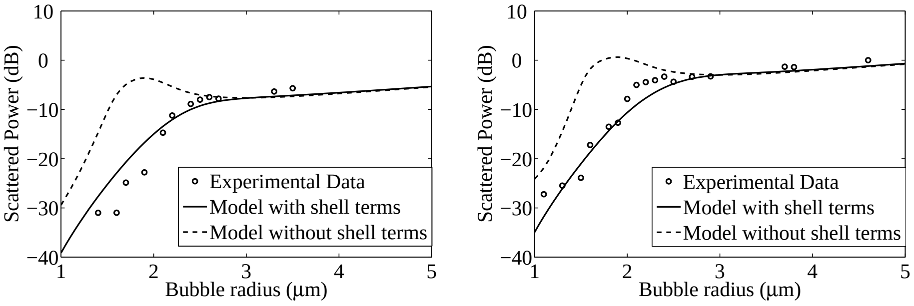

(a) (b)

Figure 2.6: A comparison between the simulated and the experimentally measured linear (fundamental frequency) scattered power as a function of bubble radius excited at pressure amplitudes of 60 kPa (a) and 100 kPa (b). A good quantitative agreement can be observed between the measured scattered power values and the ones calculated with the model taking into account the effect of the shell. The results obtained with the free-bubble model are not able to represent correctly the acoustic responses of the smaller bubbles that oscillate near and below the resonance.

2.5 Conclusions

Pulse-echo pressure waveforms from single ultrasound contrast agent microbubbles were recorded. A rigorous transducer calibration procedure allows for the quantification of the ultrasound pressure waveform scattered by single bubbles. Power spectra were derived from the scattered power of microbubbles of different sizes. The power spectra provide quantitative and detailed information on the dynamic behavior of individual ultrasound contrast agent microbubbles, in contrast to acoustic measurements made on a population of microbubbles with a relatively wide size distribution. The power spectra were compared to bubble dynamics simulations using a RayleighPlesset-type model describing the dynamics of uncoated microbubbles and a similar model incorporating the viscoelastic properties of the phospholipid shell. A quantitative agreement between the measured and the theoretically calculated acoustic backscatter was indeed found only if the phospholipid shell characteristics were taken into account.

2.6 Appendix: Transfer function

The receive transfer function of the receive transducer was determined in two ways [29–32]. In the first method, it was derived from a combination of its transmit transfer function, as measured with the calibrated membrane hydrophone described in Sec. 2.2, and its transmit-receive transfer function, as measured from reflection from a plane reflector. In the second method, the receive transfer function was estimated from the transmit transfer function alone, assuming transducer reciprocity. In both cases, the applied voltage on transmit (1 V) resulted in 25 kPa peak-negative pressure at the focus, a value sufficiently low to ensure linear acoustic propagation to and from the focal region. The results of both methods are compared hereafter. First, the transmit transfer function of this transducer was determined by:

$$T_T(f) = \frac{P_{T,o}(f)}{V_{in}(f)} \tag{2.2}$$

where f is the frequency, $V_{in}(f)$ is the complex spectrum of the input voltage waveform applied to the transducer surface (measured in open circuit), and $P_{T,o}(f)$is the spectrum of the resulting acoustic pressure at the transducer surface. A chirp signal with frequencies ranging from 0.1 MHz to 7 MHz was used as the input signal $V_{in}(f)$, and the resulting acoustic pressure at the focus of the transducer was computed using the calibration function of the membrane hydrophone. The pressure at the transducer surface, $P_{T,o}(f)$, was then estimated using the diffraction function of a focused transducer [33]. Finally, the transmit transfer function was calculated using Eq. 2.2 and its magnitude is plotted in Fig. 2.7(a).

A steel piston mirror with known reflection coefficient was subsequently positioned at the focal distance of the transducer and aligned for maximum echo. The same chirp signal was applied to the transducer and the spectrum $V_{out}(f)$ of the recorded echo signal was computed. Using the transmit transfer function previously obtained, and the reflection transfer function for a transducer focused on a flat piston [31] at normal incidence, the spectrum of the echo pressure at the surface of the transducer, $P_{R,o}(f)$, was determined. Together, these functions allowed to express the receive transfer function as:

$$T_R(f) = \frac{V_{out}(f)}{P_{R,o}(f)}, \tag{2.3}$$

and its magnitude is shown in Fig. 2.7(b).

The transfer function determined in this way was then compared to that inferred assuming reciprocity. A transducer is reciprocal if the transmit and the receive transfer function are related through a constant called the reciprocity factor [34]:

$$\frac{T_R(f)}{T_T(f)} = \frac{2RA_t}{\rho c} = \text{const.} \tag{2.4}$$

where R is the impedance of the load connected to the transducer (50 Ω), A_t is the effective surface area of the transducer, ρ the density of water and c the speed of sound in water. To verify the accuracy of the experimentally determined receive transfer function using Eq. 2.3, the receive transfer function was also calculated from the measured T_t using Eq. 2.4, which is shown in the bottom part of Fig. 2.7(c) (dotted line), together with the receive transfer function determined experimentally using the plane reflector, without assuming reciprocity, solid line in Fig. 2.7(c) (same as in Fig. 2.7(b)). Within the 3 dB bandwidth of the transducer, the amplitudes of the receive transfer functions calculated in both ways agree within 15%, or 1.2 dB. This figure may be considered as characterizing the accuracy of the experimentally determined receive transfer function. Note also that this figure may be compared to the limited accuracy of the hydrophone, stated by the manufacturer at 10%, or

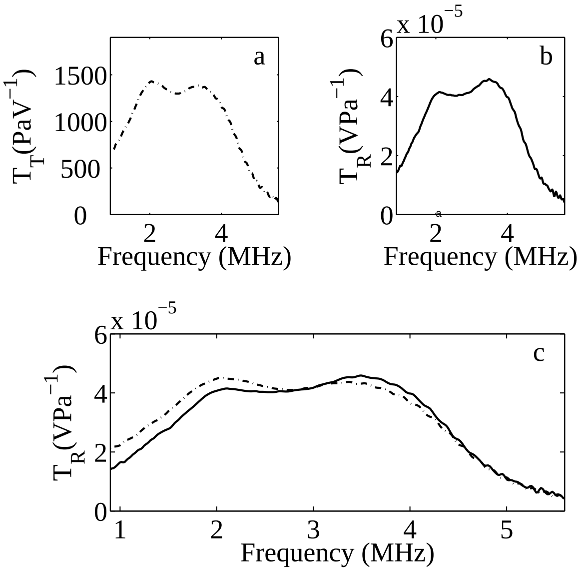

Figure 2.7: Magnitude of the transmit (a) and receive (b) transfer functions of the receiving transducer. In the bottom figure (c), the receive transfer function (solid line) is compared with the one determined assuming reciprocity (dotted line), confirming reasonable similar results (within 15%).

0.8 dB. In all results presented here the receive transfer function of Fig. 2.7(b), i.e. the one without the assumption of reciprocity, was used throughout.

References

[1] N. de Jong and L. Hoff, “Ultrasound scattering properties of albunex microspheres”, Ultrasonics **31**, 175–181 (1993).

[2] N. de Jong, L. Hoff, T. Skotland, and N. Bom, “Absorption and scatter of encapsulated gas filled microspheres: Theoretical considerations and some measurements”, Ultrasonics **30**, 95–103 (1992).

[3] J. M. Gorce, M. Arditi, and M. Schneider, “Influence of bubble size distribution on the echogenecity of ultrasound contrast agents: A study of SonoVue^{TM}”, Invest. Radiol. **35**, 661–671 (2000).

[4] K. Sarkar, W. T. Shi, D. Chatterjee, and F. Forsberg, “Characterization of ultrasound contrast microbubbles using in vitro experiments and viscous and viscoelastic interface models for encapsulation”, J. Acoust. Soc. Am. **118**, 539–550 (2005).

[5] N. de Jong, P. J. A. Frinking, A. Bouakaz, M. Goorden, T. Schuurmans, X. Jingping, and F. Mastik, “Optical imaging of contrast agent microbubbles in an ultrasound field with a 100-mhz camera”, Ultrasound Med. Biol. **26**, 487–492 (2000).

[6] P. A. Dayton, K. E. Morgan, A. L. Klibanov, G. H. Brandenburger, and K. W. Ferrara, “Optical and acoustical observations of the effects of ultrasound on contrast agents”, IEEE Trans. Ultrason. Ferroelect. Freq. Contr. **46**, 220–232 (1999).

[7] J. E. Chomas, P. A. Dayton, J. Allen, K. E. Morgan, and K. W. Ferrara, “Mechanisms of contrast agent destruction”, IEEE Trans. Ultrason. Ferroelect. Freq. Contr. **48**, 232–248 (2001).

[8] S. M. van der Meer, B. Dollet, M. Voormolen, C. T. Chin, A. Bouakaz, N. de Jong, M. Versluis, and D. Lohse, “Microbubble spectroscopy of ultrasound contrast agents”, J. Acoust. Soc. Am. **121**, 648–656 (2007).

[9] P. Marmottant, S. M. van der Meer, M. Emmer, M. Versluis, N. de Jong, S. Hilgenfeldt, and D. Lohse, “A model for large amplitude oscillations of coated bubbles accounting for buckling and rupture”, J. Acoust. Soc. Am. **118**, 3499–3505 (2005).

[10] N. de Jong, M. Emmer, C. T. Chin, A. Bouakaz, F. Mastik, D. Lohse, and M. Versluis, ““Compression-Only” behavior of phospholipid-coated contrast bubbles”, Ultrasound Med. Biol. **33**, 653–656 (2007).

[11] M. Emmer, A. van Wamel, D. Goertz, and N. de Jong, “The onset of microbubble vibration”, Ultrasound Med. Biol. **33**, 941–949 (2007).

[12] B. Dollet, S. M. van der Meer, V. Garbin, D. Lohse, N. de Jong, and M. Versluis, “Non spherical oscillations of ultrasound contrast agents”, Ultrasound Med. Biol. **34**, 1465–1473 (2008).

[13] S. Zhao, K. W. Ferrara, and P. A. Dayton, “Asymmetric oscillation of adherent targeted ultrasound contrast agents”, Appl. Phys. Lett. **87**, 134103–3 (2005).

[14] H. J. Vos, B. Dollet, J. G. Bosch, M. Versluis, and N. de Jong, "Non-spherical vibrations of microbubbles in contact with a wall: A pilot study at low mechanical index", Ultrasound Med. Biol. **34**, 685–688 (2008).

[15] C. F. Caskey, S. M. Stieger, S. Qin, P. A. Dayton, and K. W. Ferrara, "Direct observations of ultrasound microbubble contrast agent interaction with the microvessel wall", J. Acoust. Soc. Am. **122**, 1191–1200 (2007).

[16] V. Sboros, S. D. Pye, C. A. MacDonald, J. Gomatam, C. M. Moran, and W. N. McDicken, "Absolute measurement of ultrasonic backscatter from single microbubbles", Ultrasound Med. Biol. **31**, 1063–1072 (2005).

[17] V. Sboros, S. D. Pye, T. A. Anderson, C. M. Moran, and W. N. McDicken, "Acoustic rayleigh scattering at individual micron-sized bubbles", Appl. Phys. Lett. **90**, 123902–3 (2007).

[18] A. L. Klibanov, P. T. Rasche, M. S. Hughes, J. K. Wojdyla, K. P. Galen, J. H. Wible, and G. H. Brandenburger, "Detection of individual microbubbles of ultrasound contrast agents: Imaging of free-floating and targeted bubbles", Invest. Radiol. **39**, 187–195 (2004).

[19] A. L. Klibanov, P. T. Rasche, M. S. Hughes, J. K. Wojdyla, K. P. Galen, J. H. Wible, and G. H. Brandenburger, "Detection of individual microbubbles of an ultrasound contrast agent: Fundamental and pulse inversion imaging", Acad. Radiol. **9**, 279–281 (2002).

[20] D. L. Miller, "Ultrasonic detection of resonant cavitation bubbles in a flow tube by their second-harmonic emissions", Ultrasonics **19**, 217–224 (1981).

[21] C. C. Church, "The effect of an elastic solid surface layer on the radial pulsations of gas bubbles", J. Acoust. Soc. Am. **97**, 1510–1521 (1995).

[22] S. Hilgenfeldt, D. Lohse, and M. Zomack, "Response of bubbles to diagnostic ultrasound: a unifying theoretical approach", Eur. J. Phys. **4**, 247–255 (1998).

[23] T. G. Leighton, *The acoustic bubble (Academic, London, 1994).*

[24] J. B. Keller and M. Miksis, "Bubble oscillations of large amplitude", J. Acoust. Soc. Am. **68**, 628–633 (1980).

[25] M. S. Plesset and A. Prosperetti, "Bubble dynamics and cavitation", Annu. Rev. Fluid Mech. **9**, 145–85 (1977).

[26] M. P. Brenner, S. Hilgenfeldt, and D. Lohse, "Single-bubble sonoluminescence", Rev. Mod. Phys. **74**, 425–483 (2002).

[27] W. Lauterborn, "Numerical investigation of nonlinear oscillations of gas bubbles in liquids", J. Acoust. Soc. Am. **59**, 283–293 (1976).

[28] A. Prosperetti, "Nonlinear oscillations of gas bubbles in liquids: steady-state solutions", J. Acoust. Soc. Am. **56**, 878–885 (1974).

[29] X. Chen, K. Q. Schwarz, and K. J. Parker, "Radiation pattern of a focussed transducer: A numerically convergent solution", J. Acoust. Soc. Am. **94**, 2979–2991 (1993).

[30] X. Chen, K. J. Parker, and K. Q. Schwarz, "Acoustic coupling from a focussed transducer to a flat plate and back to the transducer", J. Acoust. Soc. Am. **95**, 3049–3054 (1994).

[31] X. Chen, D. Philips, K. Q. Schwarz, J. G. Mottley, and K. J. Parker, "The measurement of backscatter coefficient from a broadband pulse-echo system: A new formulation", IEEE Trans. Ultrason. Ferroelect. Freq. Contr. **44**, 515–524 (1997).

[32] T. L. Szabo, B. U. Karbeyaz, R. O. Cleveland, and E. L. Miller, "Determining the pulse-echo electromechanical characteristic of a transducer using flat plates and point targets", J. Acoust. Soc. Am. **116**, 90–96 (2004).

[33] M. Arditi, F. S. Foster, and J. W. Hunt, "Transient fields of concave annular arrays", Ultrason. Imaging **3**, 37–61 (1981).

[34] K. R. Erikson, "Tone-burst testing of pulse-echo transducers", IEEE Trans. Sonics Ultrason. **SU-26**, 7–14 (1979).

3

"Compression-Only" behavior of single ultrasound contrast agent microbubbles[‡]

Uncoated bubbles as used in single bubble sonoluminesence experiments expand more than they compress for increasing oscillation amplitude. In contrast phospholipid coated ultrasound contrast agent microbubbles are observed to compress more than they expand. Through a weakly non-linear analysis of the theoretical model proposed by Marmottant et al., we provide a more intrinsic understanding of the source of this interesting non-linear behavior of coated microbubbles. The negative offset of the mean bubble radius during oscillation, termed "compression-only", is shown to be a result of a rapidly changing bubble shell elasticity as a function of oscillation amplitude. The analytical solutions deduced from the weakly non-linear analysis are shown to predict the maximum negative offset of the initial bubble radius during oscillation at the resonance frequency. To confirm this finding the radial dynamics of single phospholipid coated microbubbles was studied as a function of both the amplitude and the frequency of the driving pressure. The radial response of the microbubbles to the different driving pressures were

---

[‡] to be submitted as: Jeroen Sijl, Marlies Overvelde, Benjamin Dollet, Valeria Garbin, Nico de Jong, Detlef Lohse and Michel Versluis,"Compression-only" behavior of ultrasound contrast agent microbubbles", Journal of the Acoustical Society of America (2009).

recorded with the Brandaris ultrahigh-speed camera. The comparison between the analytical solutions and the experimental data provides an estimate for the change in shell elasticity as a function of oscillation amplitude.

3.1 Introduction

The contrast in medical ultrasound imaging is enhanced through the use of micron-sized bubbles which through their compressibility increase the scattering cross section of the blood. The typical bubble size of the ultrasound contrast agents (UCA) is 2 to 3 μm in radius. The gas core consists of air or an inert gas and the bubbles are coated with a thin protein, lipid or polymer layer. The microbubbles are resonant scatterers at medical ultrasound frequencies of 1 to 5 MHz. Moreover, unlike tissue, the contrast agents scatter at harmonic frequencies of the driving ultrasound frequency f, mainly at the second harmonic frequency $2f$, which opens up improved imaging modalities in ultrasound, termed harmonic imaging [1]. Power modulation imaging [2] and pulse inversion imaging [3], including many of its derivatives are now standard pulse-echo techniques found on ultrasound scanner equipment. The imaging modalities exploit the non-linear behavior of the ultrasound contrast agents. A thorough and fundamental understanding of the interaction of the ultrasound with the bubbles, the induced bubble dynamics and its resulting non-linear acoustic response is therefore of prime importance for the development of improved contrast-enhanced ultrasound (CEUS) imaging.

Theoretically the non-linear dynamics of the bubbles is described by a Rayleigh-Plesset (RP)-type equation. For coated bubbles the RP equation can be extended with a set of shell parameters to model the rheological behavior of the viscoelastic coating. De Jong *et al.* [4] introduced a shell stiffness parameter and a shell friction parameter for Albunex, a human serum albumin-coated microcapsule. Church [5] refined the physical modeling for Albunex, while Hoff *et al.* [6] introduced a thin shell limit to model the phospholipid monolayer of Sonazoid, a second generation contrast agent. The volumetric oscillations predicted by the RP model were then used to predict attenuation and acoustic backscatter of the agent. Experiments on a representative sample of the UCA, containing many microbubbles, confirm the general trends and the influence of the bubble coating as predicted by the modeling: a shift of the resonance behavior to higher frequencies due to increased stiffness and a decrease of the overall acoustic response as a result of increased damping.

At a detailed level and particularly on a single bubble level the agreement between theory and experiment is less convincing. Recent optical characterization studies using high-speed imaging revealed some interesting features of single bubble dynamics that could not be described by the traditional bubble models. These include compression-only behavior reported by de Jong *et al.* [7], where the bubble oscillations are non-symmetric with respect to the resting radius; the bubbles compress more than they expand, and an apparent thresholding behavior reported by Emmer *et al.*[8], where the larger bubbles appear to respond linearly to the driving pressure, as expected, while the smaller bubbles only start to oscillate at elevated pressures, sometimes as high as 80 kPa, with no response below the threshold. Clearly, the observed non-linear features are of great interest for CEUS imaging purposes, however, the traditional models fail to describe the observations. A typical example of the compression-only behavior is shown in Fig. 3.3. A selection of a high-speed recording displays the dynamics of a 3 μm radius BR-14 contrast agent bubble driven at an acoustic pressure of 40 kPa. The experimental agent BR-14 (Bracco Research S.A., Geneva, Switzerland) consists of a suspension of bubbles with a perfluorocarbon gas core and a phospholipid monolayer. Each row in Fig. 3.1(b) corresponds to one acoustic cycle. The frames to the left and to the right show the bubble during expansion, while the center frames show the bubble during compression at maximum pressure. The radius-time (R-t) curve of the bubble displays the compression-only behavior, the bubble appears to compress twice as much relative to its expansion. Another feature that can be identified in the recording is that the coating of the bubble appears to buckle during compression. Buckling is a state of zero surface tension as a result of the high surface concentration of lipids following compression and where the monolayer will fold as it cannot resist further compression. The buckling is shown to be reversible and repeatable.

Buckling is well-known for macroscopic phospholipid monolayers and it has inspired Marmottant *et al.* [9] to develop a coated bubble dynamics model, accounting for buckling and rupture of the shell. With the static behavior of phospholipid monolayers in mind [10–14], the model relates the lipids concentration at the gas-liquid interface to an effective surface tension. The total number of phospholipids on the interface is fixed and, consequently, the effective surface tension changes with bubble radius when the bubble pulsates. The regime where the surface tension can change with radius is limited however by buckling and rupture of the shell, leading to three separate regimes, which are connected by the relevant boundary conditions. The three regimes

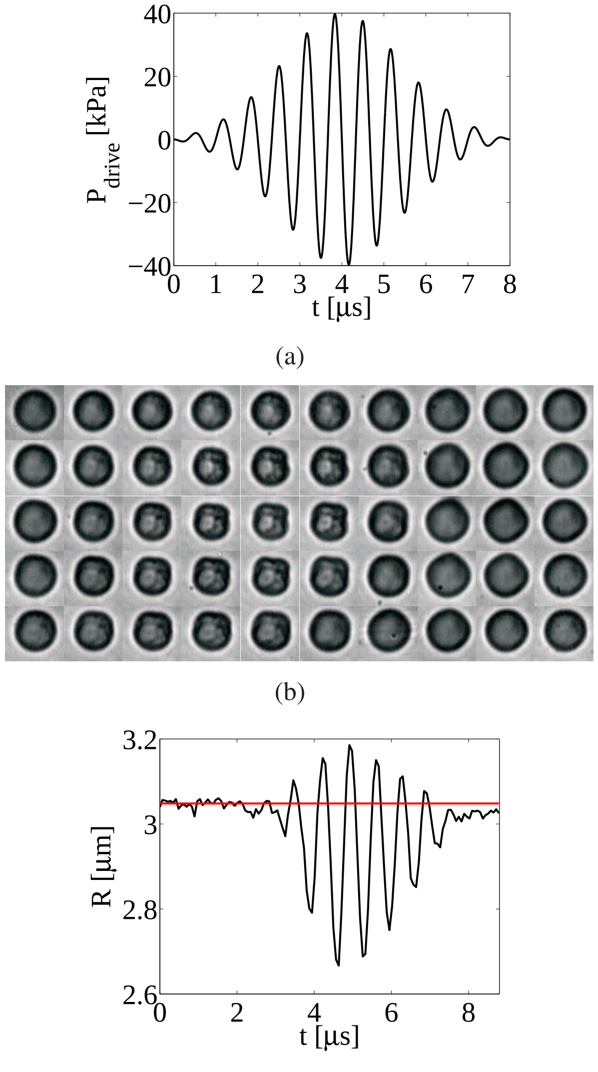

(a)

(b)

(c)

Figure 3.1: An example of the radial response of a phospholipid coated microbubble, recorded with the Brandaris ultrahigh-speed camera, showing "compression-only" behaviour. a) the driving pressure pulse b) corresponding optical images, showing buckling of the phospholipid shell c) corresponding radius time curve.

with corresponding shell parameters describe the properties of the shell: an elastic regime in the spirit of the traditional models with a shell compressibility parameter, a buckling regime defined by a buckling radius below which the bubble buckles and a ruptured regime where the lipid concentration is so small that the lipids possibly segregate into lipid islands and the gas is directly exposed to the surrounding liquid. This regime is characterized by a critical shell tension which was chosen to be that of the water-air interface. The concentration of phospholipids at the resting radius and the bubble oscillation amplitude determines the behavior of the bubble. For a moderately populated interface and at low driving pressure the bubble oscillates purely elastically. For a high packing of lipids the bubble is close to its buckling radius and the bubble easily compresses as there is little tension to resist compression and it is difficult to expand as the elastic regime resists expansion. This behavior translates into the compression-only behavior depicted in Figure 3.1(c). It should be noted that in typical recordings the buckling is not always as pronounced as shown in Figure 3.1(b). The compression-only behavior occurs quite frequently, 50% in a typical sample, see [7].

Experimental data presented in the paper by Marmottant *et al.* give very good agreement with the model calculations for each individual bubble where the shell parameters are free to vary for each case. So far we have not come to a generalized description of compression-only behavior with an unique and dedicated set of shell parameters; the overall trends are difficult to model. This has become evident in the work of de Jong *et al.* [7] where no clear dependency was found on either the initial bubble radius, the driving pressure frequency or driving pressure amplitude . The goal in this chapter is therefore to come to a more universal description of the compression-only behavior. Following previous successful work on uncoated bubbles we linearize the generalized model of the RP-equation for coated bubbles up to second order to come to an analytical solution. The analytical solution may give direct and detailed insight how the shell parameters govern the compression-only behavior. We have also used the Brandaris 128 ultra-high speed camera [15] to study the radial dynamics and related compression-only behavior of single BR-14 microbubbles. Both the driving pressure frequency and pressure amplitude were varied to enable a full characterization of this phenomenon.

In the following section, Sec. 3.2, details of the model and the linearization will be discussed. In Sec. 3.3 we will discuss and show the implications of the results from the analytical solution on the full numerical model. In Sec. 3.4 the experimental setup is described and in Sec. 3.5 the experimental results are discussed and related to the full numerical model. In Sec. 3.6 will end with a discussion. The conclusions are presented in Sec. 3.7 .

3.2 Weakly non-linear analysis

To describe the radial dynamics of a phospholipid coated microbubble, many different models have been proposed [4–6, 9, 16]. The models are based on the dynamics of an uncoated microbubble which is typically described by a Rayleigh-Plesset-type equation [17, 18]. The phospholipid shell is assumed to increase the damping of the system and is taking into account through the shell viscosity κ_s. The shell of the bubble also increases the resonance frequency of the coated microbubble [4, 19]. In earlier models this effect was accounted for by incorporating a shell stiffness that is described by the compression modulus or shell elasticity χ [4, 6]. For a phospholipid-coated microbubble it has recently been shown that the shell elasticity may be expressed as the gradient that describes the change of an effective surface tension $\chi = A(d\sigma/dA)$ [9], where A is the bubble surface area. For a bubble oscillating at small amplitude the elasticity can be related to the effective surface tension through $\sigma(R) \simeq 2\chi(R/R_0 - 1)$. How $\sigma(R)$ varies with radius is not precisely known. Some authors assumed a linear relationship between σ and R, with constant χ, while others explore more complex behavior of the viscoelastic shell. For now we assume the relation $\sigma(R)$ is unknown which brings us to the generalized form of the bubble dynamics equation for a phospholipid-coated microbubble,

$$\begin{aligned}&\rho\left(R\ddot{R}+\frac{3}{2}\dot{R}^2\right)\\&=\left(P_0+\frac{2\sigma(R_0)}{R_0}\right)\left(\frac{R_0}{R}\right)^{3\gamma}\left(1-\frac{3\gamma\dot{R}}{c}\right)\\&-\frac{2\sigma(R)}{R}-4\mu\frac{\dot{R}}{R}-4\kappa_s\frac{\dot{R}}{R^2}-P_0-P_A(t),\end{aligned} \tag{3.1}$$

In this equation R, $\dot{R}$ and $\ddot{R}$ describe the radius, the velocity and the acceleration of the bubble wall, respectively. The initial bubble radius is given by R_0 and the ambient pressure by P_0. The properties of the surrounding liquid are described by the viscosity $\mu = 10^{-3}$ Pa s, the density $\rho = 10^3$ kg/m^3 and the speed of sound $c = 1500$ m/s. The driving pressure pulse is described by $P_A(t)$. The relation between the internal gas pressure (P_g), the gas temperature and bubble volume is described by the polytropic ideal gas law, $P_g \propto R^{-3\gamma}$ where γ is the polytropic exponent. For isothermal oscillations $\gamma = 1$ and for adiabatic oscillations γ is equal to the ratio of the specific heats of the gas inside the bubble, C_p/C_v. In the experiments discussed in this chapter the thermal diffusion length scale inside the gas during one oscillation cycle can be shown to be smaller than the bubble radius [9, 19]. Therefore we approximate the oscillations as adiabatic. For the experimental agent BR-14 the gas core consists of perfluorocarbon-gas with $\gamma = C_p/C_v = 1.07$ [9, 19]. Following Eller [20] we can show that thermal damping is small but not zero in this problem. We account for thermal damping through a slight increase of the liquid viscosity $\mu = 2 \cdot 10^{-3}$ Pa s. The other three damping mechanisms are acoustic radiation damping, viscous damping by the surrounding liquid and viscous shell damping as a result of the viscosity of the phospholipid shell.

To understand why a phospholipid coated microbubble shows "compression-only" behavior it is insightful to approximate Eq. 3.1 with a second order linearization. The linearized equations can be solved analytically as shown before for similar equations [5, 21]. As a most general assumption we approximate $\sigma(R)$ around $\sigma(R_0)$ for small amplitude oscillations around R_0 through a second-order Taylor expansion:

$$\sigma(R) = \sigma(R_0) + 2\chi_{eff}\left(\frac{R}{R_0} - 1\right) + \frac{1}{2}\zeta_{eff}\left(\frac{R}{R_0} - 1\right)^2 \tag{3.2}$$

where we have defined,

$$\chi_{eff} = \frac{1}{2}R_0 \frac{\partial \sigma(R)}{\partial R}\bigg|_{R_0} \tag{3.3}$$

$$\zeta_{eff} = R_0^2 \frac{\partial^2 \sigma(R)}{\partial R^2}\bigg|_{R_0} \tag{3.4}$$

To come to an analytical solution of Eq. 3.1 we substitute Eq. 3.2 into Eq. 3.1 and we use a perturbation technique where we substitute,

$$R(t) = R_0(1 + x) \tag{3.5}$$

into Eq. 3.1. Here, x represent the bubble's relative radial excursion, where $x << 1$. After substitution we keep only the first and second order terms. This results in the following equation.

$$\ddot{x}+\omega_0\delta\dot{x}+\omega_0^2 x = P_A(t)+4b_2\dot{x}x+\alpha x^2-\frac{3}{2}\dot{x}^2-\ddot{x}x \tag{3.6}$$

where ω_0 is the linear eigenfrequency of the system. We can show that the results of the weakly non-linear analysis presented in the following are independent of the choice of the initial surface tension $\sigma(R_0)$. To simplify the calculations we therefore choose $\sigma(R_0)$ to be zero. The eigenfrequency is then given by,

$$\omega_0^2=\frac{3P_0\gamma}{R_0^2\rho}+\frac{4\chi_{eff}}{R_0^3\rho} \tag{3.7}$$

From Eq. 3.7 it is clear that the shell elasticity increases the eigenfrequency of the coated bubble compared to that of an uncoated bubble. The linear dimensionless damping coefficient of the system consists of three parts,

$$\delta=\frac{3P_0\gamma}{\omega_0 c R_0\rho}+\frac{4\mu}{\omega_0 R_0^2\rho}+\frac{4\kappa_s}{\omega_0 R_0^3\rho} \tag{3.8}$$

where the first term represents acoustic radiation damping, the second represents viscous damping and the third represents shell viscous damping. The shell viscous damping is the largest and accounts for nearly 80% of the total damping of the system. The second order terms (resonance and damping) are given by,

$$\alpha=\frac{9P_0\gamma(\gamma+1)}{2R_0^2\rho}-\frac{(\zeta_{eff}-8\chi_{eff})}{R_0^3\rho} \tag{3.9}$$

$$b_2=\frac{P_0 3\gamma(3\gamma+1)}{R_0\rho 4c}+\frac{2\mu}{R_0^2\rho}+\frac{3\kappa_s}{R_0^3\rho} \tag{3.10}$$

The solution of Eq. 3.6 depends on the driving pressure which we take, $P_A(t)=P_A\sin(\omega t)$. Next, following Church [5] we assume Eq. 3.6 has a solution of the form,

$$x(t)=A_0+A_1\sin(\omega t+\phi_1)+A_2\cos(2\omega t+\phi_2) \tag{3.11}$$

The amplitude A_1 is of first order and both A_0 and A_2 are of second order. In this solution A_0 is a time-averaged offset of the radius time curve. A_2 represents the amplitude of the second harmonic response at two times the driving pressure frequency.

Eq. 3.11 is inserted into Eq. 3.6 and if only the first order terms are considered the well-known differential equation of a harmonic oscillator is obtained:

$$\ddot{x}+\omega_0\delta\dot{x}+\omega_0^2(x)=P_A(t) \tag{3.12}$$

The solution of Eq. 3.12 gives the amplitude A_1 which describes the linear resonance curve of the microbubble,

$$A_1=\left(\frac{P_A}{\rho\omega_0^2R_0^2}\right)\left(\frac{1}{\sqrt{(1-\Omega^2)^2+\Omega^2\delta^2}}\right) \tag{3.13}$$

where the phase is described by,

$$\phi_1=\arctan\left[\frac{\delta\Omega}{\Omega^2-1}\right] \tag{3.14}$$

where Ω is the non-dimensional driving frequency,

$$\Omega=\frac{\omega}{\omega_0} \tag{3.15}$$

The second order terms from Eq. 3.6 give the amplitude and phase of the second harmonic response,

$$A_2=\frac{A_1^2\alpha}{2\omega_0^2}\sqrt{\left[\left[1+\frac{5\omega^2}{2\alpha}\right]^2+\frac{16b_2^2\omega^2}{\alpha^2}\right]}\left[\frac{1}{\sqrt{(1-4\Omega^2)^2+4\Omega^2\delta^2}}\right] \tag{3.16}$$

and a phase,

$$\phi_2=\arctan\left[\frac{B_r\sin(2\phi_1)-B_i\cos(2\phi_1)}{B_r\cos(2\phi_1)+B_i\sin(2\phi_1)}\right] \tag{3.17}$$

with,

$$B_r=\frac{4b_2\omega}{\alpha}(1-4\Omega^2)-2\delta\Omega\left[1+\frac{5}{2}\frac{\omega}{\sqrt{\alpha}}\right] \tag{3.18}$$

$$B_i=(1-4\Omega^2)\left[1+\frac{5}{2}\Omega_2^2\right]+2\delta\Omega\frac{4b_2\omega}{\alpha} \tag{3.19}$$

While the second harmonic response is important for medical imaging purposes, our main interest goes out to the time-averaged offset of the initial bubble radius which is also determined from Eq. 3.6, namely

$$A_0=\frac{A_1^2}{2\omega_0^2}\left(\alpha-\frac{1}{2}\omega^2\right) \tag{3.20}$$

with α from Eq. 3.9. We observe that the time-averaged offset A_0 can be derived from the Rayleigh-Plesset equation linearized up to second order. For a coated and an uncoated bubble the expression for A_0 is the same. Differences between the average offset of a coated and an uncoated bubble result from differences in the resonance frequency ω_0 and α. The derivation of Eq. 3.20 is based on a *continuous* driving pressure wave and A_0 is therefore a zero order frequency component. In pulsed excitation A_0 is not a harmonic function and its frequency is of the order of the length of the driving pressure waveform. Equation 3.20 shows the relationship between A_0 and A_1^2. Since A_1 is maximum at the resonance frequency, A_0 will also be maximum at the resonance frequency of the bubble. This is shown in Fig. 3.2, where A_1 and A_0 are plotted as a function of the driving frequency both for an uncoated bubble and for a coated bubble. The initial bubble radius is R_0=3.8 μm for both bubbles. A_1 and A_0 are normalized with respect to the maximum fundamental response (A_1). For this reason the decrease of the maximum amplitude of oscillation of the coated bubble as a result of the shell damping with respect to the uncoated bubble is not visible. On the other hand the increase of the resonance frequency and broadening of the resonance curve that results from the bubble shell can be clearly identified. In the figure below we find that the time-averaged offset A_0 of the uncoated bubble has a positive amplitude whereas for the coated bubble it has a negative amplitude. This remarkable difference results from the difference in α, see Eq. 3.9. For an uncoated bubble there is no change in its effective surface tension, both χ_{eff} and ζ_{eff} are zero and Eq. 3.9 reduces to the first term only, which is always positive. For a coated bubble on the other hand, the value of α can become negative for a sufficiently large ζ_{eff}, in which case A_0 becomes negative, leading to a decrease of the initial bubble radius during the forcing. This is in agreement with what was found by Marmottant *et al.* [9] who showed with a numerical study with his model that a bubble with an initial bubble radius close to the transition from the elastic to the buckling regime ($R_0 = R_{buckling}$) shows most compression-only behavior. This sudden buckling transition is characteristic for a collapsing phospholipid monolayer [14] and marks a large positive second derivative of the effective surface tension with respect to radius ζ_{eff}.

A few comments on the elasticity χ_{eff} and its first order correction ζ_{eff} are in order. In the most general form both χ and ζ are a function of the radius R. In the model by de Jong et al. the bubble shell is assumed to be purely viscoelastic with a constant elasticity, $\chi = \text{constant}$. Consequently the first order correction and derivative of χ, $2R_0(\partial\chi/\partial R) = \zeta$ is zero. Using a constant elasticity to model a more complex elastic behavior, results in an effective elasticity χ_{eff} which is different from the elasticity $\chi(R)$ which varies with radius, R. As the linear eigenfrequency ω_0 originates from a first order linearization, the elasticity in Eq. 3.7 is assumed to be constant, χ_{eff}. This analysis holds similarly for the description of $\zeta(R)$ where we have introduced a constant effective first order correction ζ_{eff} for the linearized equations. In the analytical solutions presented in Fig. 3.2 χ_{eff} was taken to be 0.55 N/m, following van der Meer et al. [19] who deduced the elasticity of phospholipid coated bubbles from an analysis of linear resonance curves; the use of χ_{eff} is adequate. ζ_{eff} was taken to be 42.2 N/m. For this value of ζ_{eff} we observe in Eq. 3.9 and Eq. 3.20 that the zero order offset of the radius of the bubble at resonance is larger even than the oscillation amplitude. This indeed results in the very asymmetric radius-time curves similar to the curves found experimentally by Marmottant et al. [9] and de Jong et al. [7]. Let us reconsider the radius-time curve of Fig. 3.1(c). If we now view the radius-time curve, not as a set of bubble expansions and compressions from a reference resting radius R_0, but instead we recover the radius-time curve from a superposition of R_0, a negative zero-order offset A_0, and a linear oscillation A_1, we obtain the picture plotted in Fig. 3.3. As the frequency of A_0 is an order lower than that of A_1, a segmentation in the frequency domain can be performed after subtraction of the resting radius R_0. This results in the temporal evolution of A_0 and A_1, Fig. 3.3 to the right. Note that strictly speaking A_1 analyzed in this way may contain higher order harmonics of the form given in Eq. 3.16, which we will neglect here. Details of the Fourier segmentation will be given in the experimental section. Equation 3.20 has shown that the zero-order offset A_0 is negative for sufficiently large ζ_{eff} and that the maximum compression-only behavior is recovered for a maximum A_1. It can also be shown that the driving frequency has very little effect on the relation between A_0 and A_1 when compression-only behavior is observed. In this case ζ_{eff} is large as to make α sufficiently large and the contribution of ω is negligible. Something that is less obvious from the equation, but it can be shown once one goes through all the equations is that the compression-only behavior is most pronounced for the smallest bubbles. This finding will be confirmed by full numerical simulations in the following section and is in agreement with the recent observations of compression-only behavior of phospholipid-coated Sonovue and BR-14 by de Jong et al. [7].

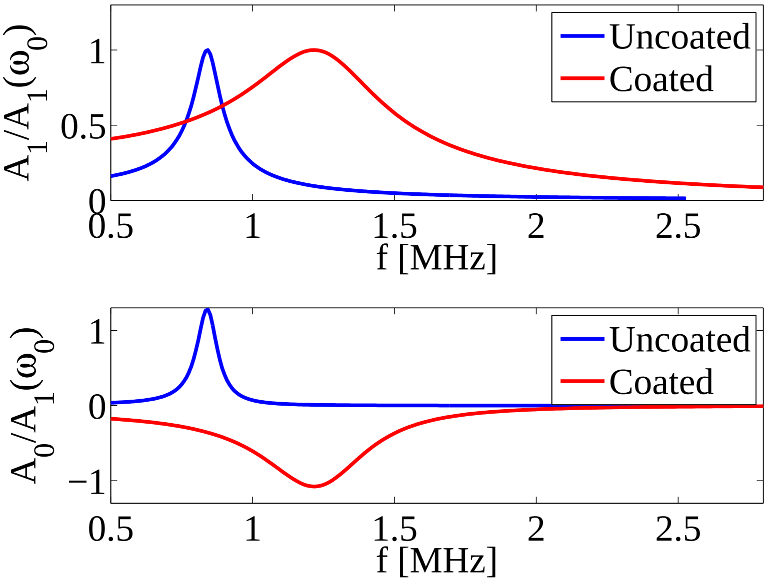

Figure 3.2: The top figure shows the resonance curve (fundamental response (A_1) as a function of driving frequency) of a R_0=3.8 μm radius free gas bubble and a coated microbubble as determined from the linearized Rayleigh-Plesset equations. Both are normalized to their maximum amplitude. The bottom figure shows the corresponding zero order frequency component (A_0) as a function of frequency, also normalized to the corresponding maximum fundamental response (A_1). Both for the uncoated bubble and the coated microbubble the zero order frequency component is maximal at the resonance frequency. The free gas bubble shows a positive offset whereas the coated microbubble shows a negative offset. The parameters used in the simulation were, P_A = 40 kPa, χ_{eff}=0.55 N/m, $\kappa_s = 3 \cdot 10^{-8}$ kg/s and $\zeta_{eff} = 42.2$ N/m.

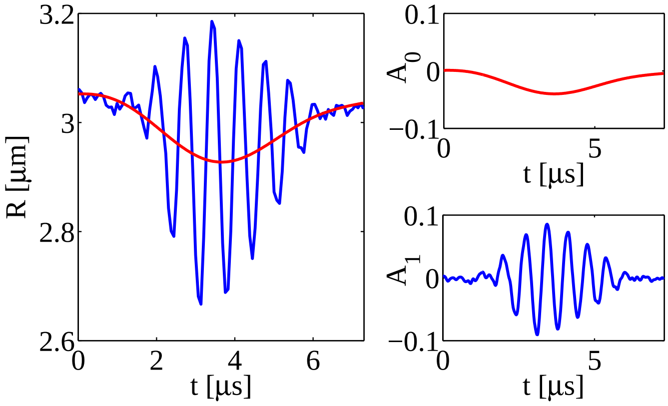

Figure 3.3: The radius time curve presented in Fig. 3.1(c) can be decomposed into two components. The fundamental response A_1 *and a low frequency component* A_0 *expressing the "compression-only" behavior the bubble is showing. The frequency of* A_0 *is of the order of the reciprocal of the length of the driving pressure pulse.*

3.3 Numerical Model

From the analytical solutions for A_0 presented in the previous section it was observed that "compression-only" behavior of phospholipid coated microbubbles is predominately determined by the initial increase of the shell elasticity with bubble oscillation amplitude $\zeta_{\mathrm{eff}} = 2R_0\partial\chi_{\mathrm{eff}}/\partial R$. Earlier models such as proposed by de Jong *et al.* [4] assume a constant shell elasticity and are therefore unable to explain such behavior. Equation.3.2 is valid for small bubble oscillation amplitudes only. For larger bubble oscillation amplitudes the effective surface tension as predicted by Eq. 3.2 grows indefinitely with R and could become negative. Therefore in this chapter we will use the model proposed by Marmottant *et al.* [9] where the shell elasticity is assumed to change with bubble oscillation amplitude and the effective surface tension is bound between $\sigma = 0$ N/m and $\sigma = 0.072$ N/m.

As a first and rather ad-hoc approximation Marmottant *et al.* assumed three regimes for $\sigma(R)$, one elastic regime, for small bubble oscillations, where the effective surface tension is described in the spirit of the model of de Jong *et al.* [4] and two regimes where the shell elasticity is assumed to be zero $\chi = 0$ Nm^{-1}. The shell elasticity χ in the elastic regime is assumed to be fixed and the function $\sigma(R)$ as a whole is assumed to be same for all bubbles indepen-

dent of the initial bubble radius. Therefore this model introduces only one additional parameter as compared to the model proposed by de Jong *et al.* [4]: the initial surface tension of the bubble $\sigma(R_0)$, which directly relates to the phospholipid concentration on the interface of the bubble.
In the model described by Marmottant et al. $\sigma(R)$ is defined as a piecewise affine function, implying that $\zeta(R)$ is zero except at the two transition points $\sigma(R) = 0$ and $\sigma(R) = \sigma_{\text{water}}$, where this quantity is not defined. As already pointed out by Marmottant *et al.* [9], this is a practical idealization of the shell response which is smoother in reality. Furthermore, the weakly non-linear analysis presented in the previous section has shown that ζ_{eff} and thus $\zeta(R)$ is of prime importance to explain "compression-only" behavior. In order to have $\zeta(R)$ defined for all R we propose to introduce two quadratic crossover functions, $Y_1(R)$ and $Y_2(R)$ in the two transition regions as depicted in Fig. 3.4. In order for both the effective surface tension and the shell elasticity to remain continuous at the two transition points the two quadratic functions at the two different transitions should each satisfy a set of boundary conditions. For the transition from the so called 'buckling' regime to the 'elastic' regime the function $Y_1(R)$ should be chosen such that $\sigma(R)$ satisfies,

$$\begin{aligned} \sigma(R_{\text{Buck}}) &= 0 \text{ N}/m \\ \partial\sigma(R_{\text{Buck}})/\partial R &= 0 \text{ N}/m^2 \\ \partial\sigma(R_{\text{Elas}})/\partial R &= 2\chi_{max}/R_0 \text{ N}/m^2 \end{aligned} \tag{3.21}$$

where R_{Buck} marks the transition to the buckling regime and R_{Elas} to the elastic regime. In a separate experiment by Overvelde *et al.* [22] resonance curves of phospholipid coated BR-14 microbubbles were measured at extremely low driving pressures. This allowed measurements of the resonance curves of bubble in a purely elastic state as the oscillations were confined to the 'elastic' regime. In this way the *maximum* shell elasticity in the elastic regime could be determined and was found $\chi_{max} = 2.5\text{N}/m$. For radii between R_{Buck} and R_{Elas} the shell elasticity is determined by Y_1 as shown in Fig. 3.4. To limit the number of free parameters of the model we have assumed the transition from the 'buckling' regime to the 'elastic' regime and from the 'elastic' regime to the 'ruptured' regime are the same. The boundary condition that should be

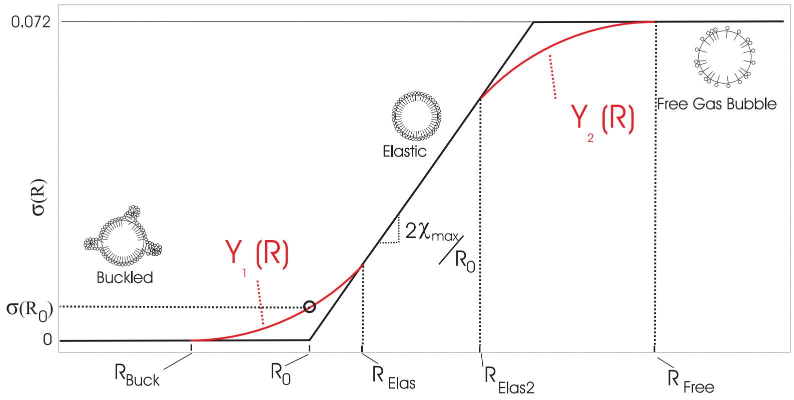

Figure 3.4: In the model of Marmottant et al. [9] the second derivative of $\sigma(R)$ *with respect to* R *is undefined in the transitions from the buckling regime to the elastic regime, and from the elastic regime to the free gas bubble regime. To correct this, we propose to expand the original model with two quadratic functions* Y_1 *and* Y_2 *that describe the two transition points.*

satisfied for this last transition are therefore,

$$\begin{aligned} \sigma(R_{\text{Free}}) &= 0.072\ N/m \\ \partial\sigma(R_{\text{Elas2}})/\partial R &= 2\chi_{max}/R_0\ N/m^2 \\ \partial\sigma(R_{\text{Free}})/\partial R &= 0\ N/m^2 \end{aligned} \tag{3.22}$$

The end of the elastic regime is now marked by R_{Elas2} and the start of the 'ruptured' regime is marked by R_{free}. From the boundary conditions we find the following quadratic functions.

$$Y_1 = \frac{1}{2}\zeta\left(\frac{R}{R_{\text{Buck}}} - 1\right)^2 \qquad \text{if} \quad R_{\text{Buck}} < R < R_{\text{Elas}} \tag{3.23}$$

$$Y_2 = \sigma_{\text{water}} - \frac{1}{2}\zeta\left(\frac{R}{R_{\text{Buck}}} - \frac{R_{\text{Free}}}{R_{\text{Buck}}}\right)^2 \qquad \text{if} \quad R_{\text{Elas2}} < R < R_{\text{Free}} \tag{3.24}$$

With these two new quadratic functions the final function of $\sigma(R - \Delta R)$

becomes,

$$\sigma(R-\Delta R) = \begin{cases} 0 & \text{if } (R-\Delta R) < R_{\text{Buck}} \\ Y_1(R-\Delta R) & \text{if } R_{\text{Buck}} < (R-\Delta R) < R_{\text{Elas}} \\ 2\chi_{max}\left(\frac{(R-\Delta R)}{R_0} - 1\right) & \text{if } R_{\text{Elas}} < (R-\Delta R) < R_{\text{Elas2}} \\ Y_2(R-\Delta R) & \text{if } R_{\text{Elas2}} < (R-\Delta R) < R_{\text{Free}} \\ \sigma_{\text{water}} & \text{if } (R-\Delta R) > R_{\text{Free}} \end{cases} . \tag{3.25}$$

Here ΔR defines the shift of the $\sigma(R)$ curve with respect to R_0, i.e. ΔR defines $\sigma(R_0)$.

In the original model ζ was undefined in the two transition regions. With the introduction of the two quadratic function the constant ζ can be defined. This implies that another shell parameter must be introduced. However, since in the original model ζ was undefined and in fact was determined by the step size of the numerical code, the original model could also be considered as having already incorporated (in an uncontrolled way) the ζ shell parameter. Note that once ζ, $\sigma(R_0)$ and χ_{max} are defined, the parameters, R_{Buck}, R_{Elas}, R_{Elas2} and R_{Free} are fixed and are therefore not to be considered free shell parameters. Furthermore, as in the original model we assume that $\sigma(R)$ is valid for all bubble radii.

Since χ_{max} is known and the same for all bubbles, the only parameters that affect the “compression-only” behavior of bubbles and that can vary from bubble to bubble are ζ and $\sigma(R_0)$. To investigate the effect of these two free parameters and the initial bubble radius R_0 on the “compression-only” behavior of phospholipid coated microbubbles we have conducted a parameter study of the full numerical model described by Eq. 3.1 where $\sigma(R)$ is described by Eq. 3.25. The results are presented in Fig. 3.5. Through a variation of the driving pressure amplitude the zero order offset A_0, i.e. the “compression-only” behavior, was determined as a function of the oscillation amplitude A_1^2. By varying both ζ and $\sigma(R_0)$ independently for a bubble with an initial bubble radius $R_0 = 1.2$ µm the influence of these two parameters on the relation between A_0 and A_1 was determined. Finally, also the effect of the initial bubble radius R_0 on the “compression-only” behavior was investigated by varying R_0. In the weakly non-linear analysis it was found that A_0/A_1^2 is nearly independent of the driving pressure frequency. We therefore chose the frequency close to resonance, as to promote large amplitude oscillations to cover a reasonable range of A_1. We used a frequency of 4 MHz in the case of the 1.2 μm bubble and 2 MHz and 1 MHz for the 2.3 μm and 3.4 μm bubble, respectively. Similarly the shell viscosity κ_s does not affect the quantity A_0/A_1^2 and a difference in the shell viscosity for different bubbles therefore not alters the results presented in Fig. 3.5. In the simulations presented in Fig. 3.5 a shell viscosity of $\kappa_s = 1 \cdot 10^{-9}$ kg/s was taken for the 1.2 μm bubble and the 2.3 μm and 3.4 μm bubble were assumed to have a shell viscosity of $\kappa_s = 1 \cdot 10^{-8}$ kg/s and $\kappa_s = 2.5 \cdot 10^{-8}$ kg/s respectively, in agreement with the values found by van der Meer *et al.* [19] for the same type of bubbles. To determine A_1 from the individual radius-time curve, the zero-order frequencies were first filtered out with an ideal high-pass filter with a cut-off frequency of 1 MHz. The resulting radius time curve was normalized to the initial bubble radius R_0. Note again that strictly speaking the A_1 defined here differs slightly from the A_1 of the analytical solutions, since the numerical data may contain higher harmonics. To determine A_0, the initial bubble radius R_0 is first subtracted from the full radius time curve $R(t)$. After the resulting curve is normalized with the initial bubble radius R_O we apply an ideal low-pass filter with a cut-off frequency of 1 MHz to the curve. The amplitude of the resulting low frequency offset shown in Fig. 3.3 is defined as A_0. As was found from the weakly non-linear analysis presented in the previous section, we find from the numerical simulations using the full numerical model that the zero-order frequency component A_0 is indeed negative and decreases for increasing oscillation amplitude A_1. Furthermore, from Fig. 3.5(b) we find that the "compression-only" behavior slightly increases for increasing ζ however the increase is limited even for a two order of magnitude increase of ζ. This confirms that the relation between A_0 and A_1^2 depends on an effective $\zeta_{eff} = (\int \zeta(R)dR)/(\int dR)$. ζ_{eff} is less dependent on the initial $\zeta(R_0)$ but depends both on the size of the regime of ζ and the value of ζ itself. This is confirmed by the decrease of the "compression-only" behavior that we observe for larger A_1^2 but also by the strong dependency of the A_0/A_1^2 on the initial surface tension $\sigma(R_0)$. In Fig. 3.5(d) we observe that for a bubble with an initial surface tension $\sigma(R_0)$ close to the buckling regime A_0/A_1^2 is smaller, i.e. we observe more "compression-only" behavior. For a bubble with a larger initial surface tension $\sigma(R_0)$ the region with a large positive ζ is reached only for larger oscillation amplitudes. Furthermore the transition from the elastic regime to the ruptured regime is marked by a negative ζ and is reached for much smaller oscillation amplitudes, explaining why the minimum A_0 reached for bubbles with a large $\sigma(R_0)$ is higher. For an initial surface tension $\sigma(R_0)$ sufficiently large $\sigma(R_0) > 0.036\mathrm{N}/m$(=0.072/2) we may even observe

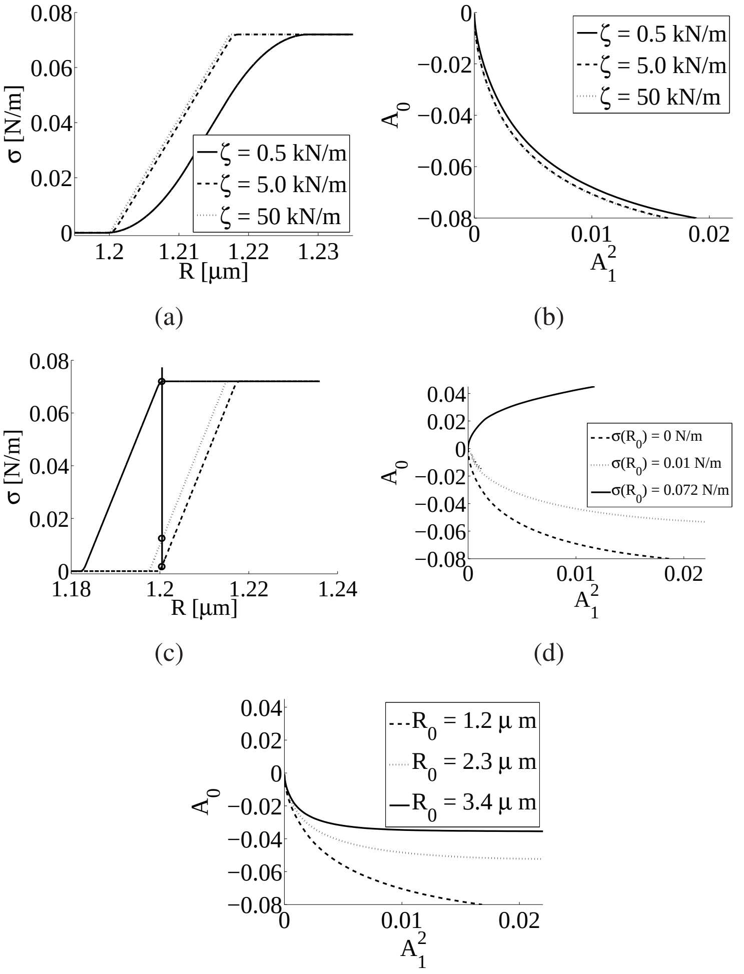

(a) (b)

(c) (d)

(e)

Figure 3.5: A parameter study of the "compression-only" behavior of phospolipid coated microbubbles. Three parameters were varied, ζ*,* $\sigma(R_0)$ *and* R_0 *which resulted in different relations for* $\sigma(R)$ *as shown in the two left figures a) and c). The "compression-only" behavior was expressed as the relation between* A_1^2 *and* A_0*, where* A_1^2 *was varied by changing the driving pressure amplitude with a fixed driving frequency of 4 MHz. The top right figure b) shows the "compression-only" behavior for three different values of* ζ *with* $\sigma(R_0) = 0$ *N/m and* $R_0 = 1.2$ *μm. The middle right figure d) shows how the "compression-only" behavior changes for different* $\sigma(R_0)$ *with* $\zeta = 5000$ *N/m and* $R_0 = 1.2$ *μm fixed. Finally in the bottom figure, e) the "compression-only" behavior for differently sized bubbles is shown (*$\zeta = 5000$ *N/m,* $\sigma(R_0) = 0$*). In all figures the maximum shell elasticity equals* $\chi_{max} = 2.5$ *N/m.*

”expansion only” instead of “compression-only” behavior, see also experimental evidence in Marmottant et al. [9]. Finally, we observe that the full numerical simulations predict that smaller bubbles show more “compression-only” behavior in agreement with recent observations by de Jong et al. [7].

3.4 Experimental

From the weakly non-linear analysis and the numerical calculations with the full model we found that the amount of “compression-only” behavior that a microbubble exhibits depends on the initial bubble radius R_0, the initial surface tension $\sigma(R_0)$ and the amplitude of oscillation A_1. The other parameters of the model, the shell elasticity, shell viscosity, and the driving pressure amplitude and frequency are all included in A_1. The relation between A_0 and A_1 is unaltered by these parameters. To investigate how and if these theoretical findings can be confirmed experimentally we recorded the radial dynamics of 45 individual microbubbles with the Brandaris ultrahigh-speed camera [15] as a function of both the driving pressure frequency and amplitude. To study purely the effect of compression-only on the bubble dynamics, the bubble under study was isolated and located away from neighboring objects (walls, bubbles) by means of optical tweezers.

3.4.1 Experimental setup

BR-14 (Bracco Geneva) contrast agent microbubbles were injected in an OptiCell® chamber (Nunc™). The chamber was positioned on top of a custom-built water tank, see figure 5.2. The water tank contained a light fiber and an ultrasound transducer (PA168, Precision Acoustics). A needle hydrophone (HPM02/1, Precision Acoustics) replacing the OptiCell was used to align the ultrasound with the focus of the objective. A XYZ-stage controlled the OptiCell position separately from the watertank in order to keep the ultrasound aligned with the objective. For accurate control of the distance between the bubble and the wall a motorized stage (M-110.2DG, PI) was used.

The ultrahigh-speed Brandaris camera [15] was coupled to a set of optical tweezers. A dichroic mirror (CVI laser) reflected the infrared laser beam (λ = 1064 nm) into the back aperture of the objective (LUMPLFL100xW, Olympus). Individual bubbles were trapped in the low intensity region of a Laguerre-Gaussian beam. The imaging and trapping of the microbubble was

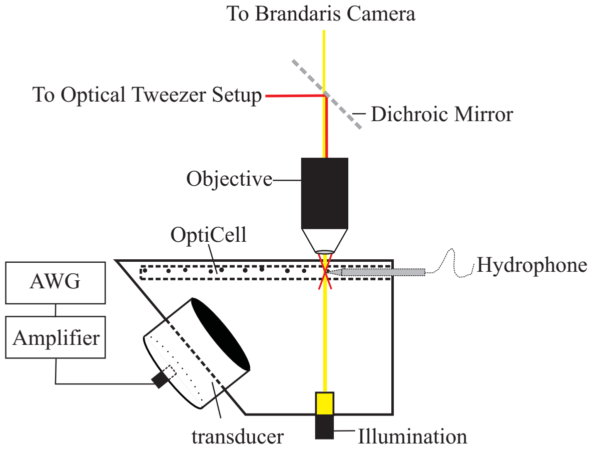

Figure 3.6: A schematic overview of the experimental setup. Single microbubbles were investigated with the combined Brandaris camera and optical tweezers setup. The driving waveform produced by an arbitrary waveform generator was amplified and transmitted by a focussed transducer.

performed through the same objective. The dichroic mirror transmitted the visible light used for imaging. Details of the optical tweezers setup coupled to the Brandaris camera can be found in Garbin *et al.* [23].

The ultrasound pulses were generated by an arbitrary waveform generator (8026, Tabor Electronics). The signal was amplified (350L, ENI) and sent to the ultrasound transducer. The transducer was calibrated prior to the experiments in a separate water tank over a broad range of frequencies (0.75-5 MHz) and ultrasound pressures. The driving pressure waveform had a length of 10 cycles and was apodized with a 3 cycle Hanning window. One experiment consisted of 2×6 movies of 128 frames. The bubble dynamics of the very same bubble was recorded while scanning the applied frequency at constant pressure in each of the 12 movies.

3.4.2 Data analysis

The images from the high-speed movies were analyzed off-line with Matlab (The Mathworks, Natick, MA). The radius of the bubble as a function of time $R(t)$ was determined from each image sequence through a semi-automatic minimum cost algorithm [19]. A typical radius-time curve is shown in Fig. 3.7

(top- left). The radius R was normalized to the initial bubble radius R_0. The linear oscillation amplitude A_1 was determined from the individual radius-time curve through filtering (see figure top right) with an ideal high-pass filter with a cut-off frequency of 1 MHz. To determine A_0, the initial bubble radius R_0 was first subtracted from the full radius-time curve $R(t)$, then normalized to R_0. An ideal low-pass filter with a cut-off frequency of 1 MHz was applied to the curve. The amplitude of the resulting low frequency offset shown in Fig. 3.7 is defined as A_0.

3.5 Results

In total, 324 resonance curves at different driving pressure amplitudes were obtained for 45 individual microbubbles. In 24 % of the experiments A_0 was found to be positive, i.e. 76 % of the experiments showed a negative time average offset. Furthermore the amount of "compression-only" behavior was observed to vary for different bubbles, even for bubbles with the same size. Figure 3.8 shows the linear resonance curves of two microbubbles, both with a size of 2.3 μm. A_1 and the corresponding A_0 are plotted as a function of the driving frequency. Both bubbles were excited with the same driving pressure amplitudes and driving pressure frequencies in order to construct their resonance curves at different driving pressure amplitudes. The driving pressure amplitude for both resonance curves shown in Fig. 3.8 was 18.5 kPa. We observe that the bubbles have the same resonance frequency of 2.5 MHz, which following Eq. 3.7 indicates that the bubbles have the same effective elasticity χ_{eff}. We find good agreement of the experimental data with the theoretical linear resonance curve with a χ_{eff} of 0.55 N/m. We also see that the time average offset A_0 is minimal at the resonance frequency of the bubbles, in agreement with our earlier findings in Eq. 3.20. On the other hand, one of the two bubbles shows less "compression-only" behaviour through a smaller amplitude of A_0. The data can be fitted to construct the two theoretical predictions for A_0 based on Eq. 3.20. Again excellent agreement is observed between the analytically calculated A_0 and the experimental data. For the very same bubbles we plot in Fig. 3.9 the negative time average offset. We find that the relation between A_0 and A_1^2 is different. In the data presented in Fig. 3.9 all the different resonance curves are bundled and can be observed to collapse onto a single line. This confirms our previous findings that both the driving pressure amplitude and frequency do not change the relation between A_0 and

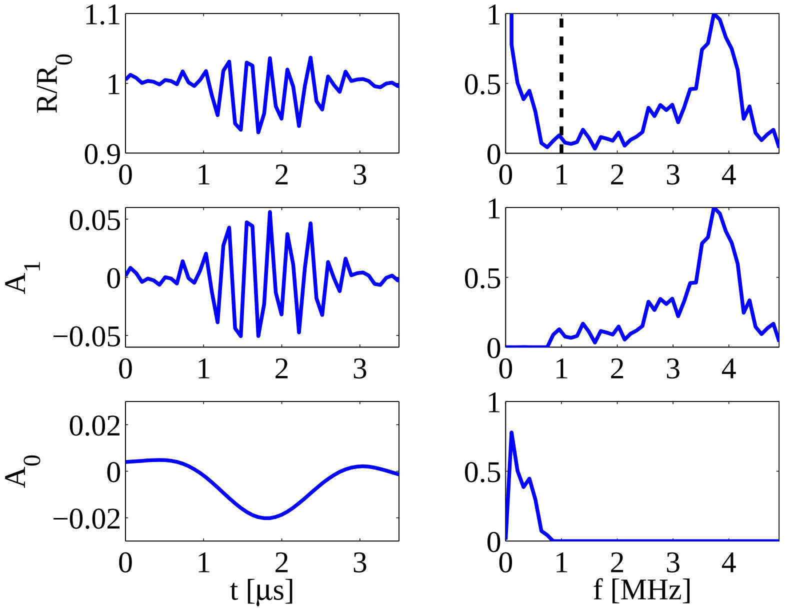

Figure 3.7: Top left figure, an example of a radius time curve of a 1.9 μm radius phospholipid coated bubble recorded with the ultrahigh-speed Brandaris camera. The top right figure shows the corresponding Fourier transform. The Fourier transform besides a zero-order component from the initial bubble radius R_0 *also shows another low frequency component which is associated with the "compression-only" behavior of the microbubble. The radial response can be decomposed into a fundamental/linear response (middle figures) and a low frequency component of the order of the length of the driving pressure pulse (bottom figures). For the phospholipid coated microbubble the low frequency component has a negative amplitude which is contrary to what we observe for the free gas bubble where it is positive.*

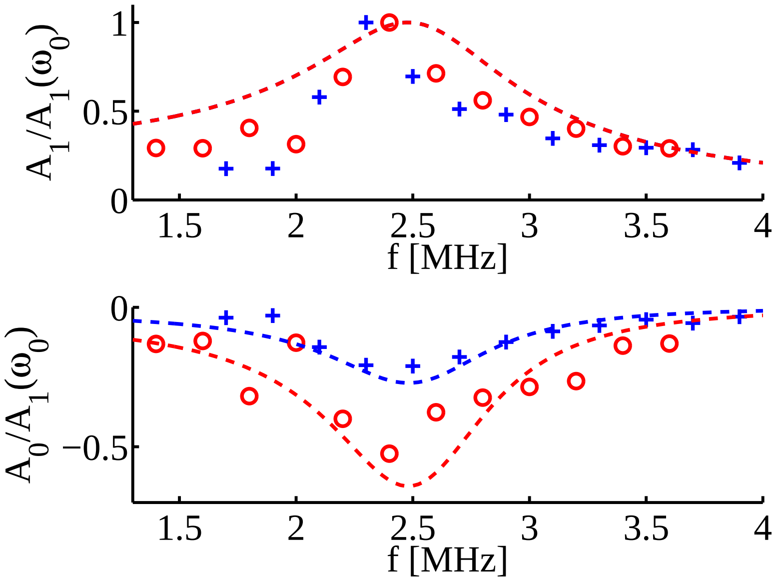

Figure 3.8: Experimentally determined resonance curve for two 2.3 μ*m radius bubbles (same bubbles as in Fig. 3.9 with the two corresponding time average offsets* A_0*. Both* A_0 *and* A_1 *are normalized on the maximum value of* A_1*. Though the resonance frequency and thus the shell elasticity* χ *is the same for both bubbles the time average offset is different for both, as in Fig. 3.9. The experimental data is in good agreement with the analytically calculated resonance curves which are based on* $\chi(R)=$ *0.55 (N/m) determined by van der Meer et al.[19]. The two theoretical predictions for* A_0 *are based on two different values for* ζ_{eff}*,* $\zeta_{\mathrm{eff}} = 91$ *(N/m) for the crosses and for the circles* $\zeta_{\mathrm{eff}} = 41$ *(N/m).*

A_1^2. The shape of the relation between A_0 and A_1^2 is similar to as found from the numerical simulations in Fig. 3.5. As mentioned before, this decrease of the gradient (or flattening of the curve at higher A_1) is a result from the transition from the elastic regime into the ruptured regime. For the two different bubbles we observe that both the change of the gradient and the minimum A_0 is different. Therefore, based on our analytical and numerical results where it was found that ζ was a parameter of relatively little importance, the difference between the two curves can only be explained by a difference in $\sigma(R_0)$. To fit the numerical model to the experimental data therefore requires the variation of only one parameters. Two least-squares fits of the numerical model to the two experimental data sets are shown in Fig. 3.9. The data set corresponding to the bubble showing most “compression-only” behaviour is best fitted with a value for $\sigma(R_0) = 0.008$ N/m, the other data set is shown to nicely fit with the numerical model for $\sigma(R_0) = 0.02$ N/m. The other shell parameters of the numerical model were taken as before from the literature $\kappa_s = 1 \cdot 10^{-8}$ kg/s and $\chi = 2.5$ N/m. Even though the maximum shell elasticity χ_{max} is the same, the initial surface tension $\sigma(R_0)$ can vary for different bubbles. Figure 3.10 shows all experimental data together where we plot A_0 as a function of A_1^2. The smallest initial bubble radius in the experimental data is 1.2 μm and the largest bubble had a radius of 3.4 μm. The shape of the scattered experimental data is determined by the limiting number of value’s $\sigma(R_0)$ can have. The smallest value for $\sigma(R_0) = 0$ N/m for the smallest bubble size determines the maximum amount of “compression-only” behavior phospholipid coated microbubbles can have. This is confirmed by the numerical simulation of the full model of Marmottant et al. for $\sigma(R_0) = 0$ N/m and $R_0 = 1.2\mu$m, already shown in Fig. 3.5 and again shown in Fig. 3.10. This numerical simulation which for this experimental data represents the maximum “compression-only” behavior corresponding to the smallest bubble with the smallest $\sigma(R_0)$ indeed confines the left/bottom side of the experimental data. As shown in the numerical simulation (Fig. 3.5) larger bubbles show less “compression-only” behaviour which is confirmed by another numerical simulation of the full model of Marmottant et al. shown in Fig. 3.5(e).

3.6 Discussion

A better understanding of “compression-only” behavior provides a better understanding of the characteristics of the phospholipid coated microbubbles in

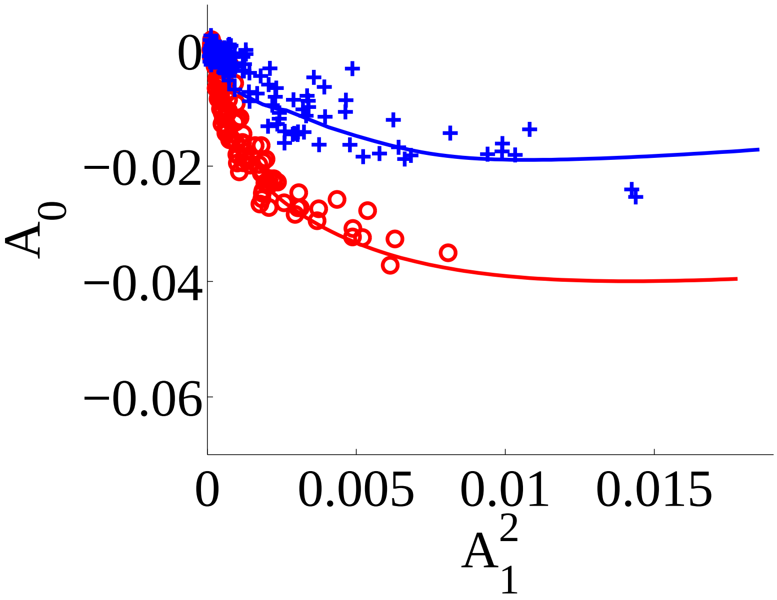

Figure 3.9: Two different microbubbles with the same radius $R_0 = 2.3$ μ*m show different "compression-only" behavior though the experimental data was obtained for similar driving pressure amplitudes and frequencies. Though the two curves look qualitative the same, quantitatively they are different. The experimental data of both bubbles is correctly described by a single parameter fit of* $\sigma(R_0)$ *of the full numerical model. The best fit through the circles corresponds to a* $\sigma(R_0) = 0.008$ *N/m and for the crosses it is* $\sigma(R_0) = 0.02$ *N/m. In the full numerical simulations the other shell parameters were taken from the literature to be* $\kappa_s = 1 \cdot 10^{-8}$ *kg/s and* $\chi = 2.5$ *N/m. The driving pressure frequency was fixed on 2 MHz and the driving pressure amplitude was varied.*

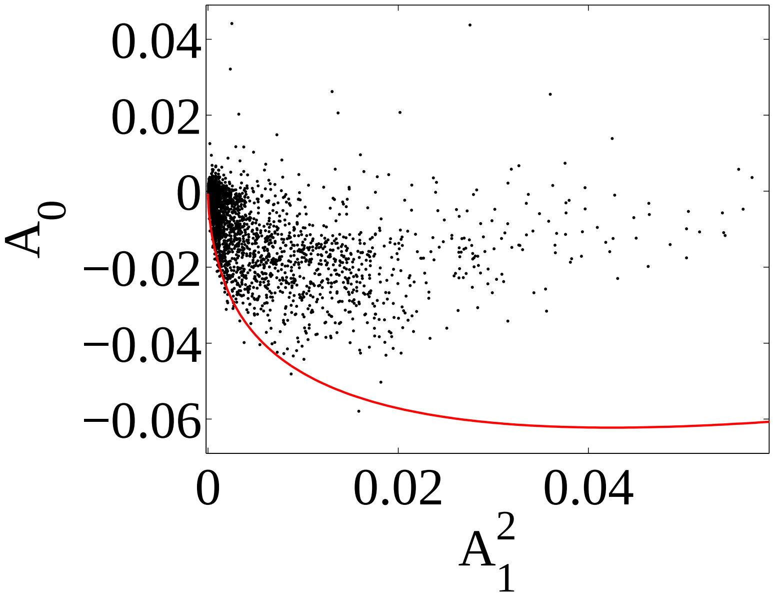

Figure 3.10: According to the numerical model the amount of "compression-only" exhibited by a phospholipid coated microbubble is restricted. The initial condition of the phospholipid shell, $\sigma(R_0)$ *and the initial bubble radius* R_0 *determine the maximal time average offset* A_0 *a bubble can show in its* $R(t)$ *curve. This hypothesis is confirmed by the clear boundary we observe on the left/bottom flank in this scattered plot where* A_0 *is plotted as a function of* A_1^2 *for all experimental data. This boundary is correctly described by the red line corresponding to the numerically calculated relation between* A_0 *and* A_1^2 *for a bubble with an initial bubble radius* $R_0 =$*1.2*μ*m (smallest bubble in the experimental data) and* $\sigma(R_0) = 0$ *N/m*

general. From the results presented in this chapter for example it is clear that the shell elasticity of the phospholipid shell varies with bubble oscillation amplitude. To explain the observed "compression-only" behavior the shell elasticity of a phospholipid coated microbubble should first rapidly increase with oscillation amplitude and for larger oscillation amplitude again decrease. This finding confirms the assumption of Marmottant *et al.* that the behavior of a phospholipid coated microbubble oscillating in the MHz frequency range is similar to the static behavior of phospholipid monolayers [10–14]. The rapid increase of the shell elasticity with oscillation amplitude is a result of reversible collapse of the phospholipid monolayer as it is referred to in the literature [14]. The collapse of the monolayer is a result of compressing a saturated layer of phospholipids that is in the solid state. If the monolayer is compressed beyond this point, 3D structures of phospholipids are formed on the surface of the monolayer. This phenomenon is termed buckling of the monolayer and can be observed in microscopic detail as shown in Fig. 3.1(b). If the monolayer is in the collapsed or buckled state the effective surface tension is zero or at least very close to zero and does not vary anymore with oscillation amplitude of the bubble. If the monolayer is expanded beyond its collapsed state, the effective surface tension suddenly starts to vary with the phospholipid surface concentration and thus with the bubble surface area/radius, effectively introducing a surface elasticity. The collapse point of the phospholipid monolayer marks the rapid increase of the shell elasticity. The decrease of the shell elasticity with oscillation amplitude for larger oscillation amplitudes is a result of an upper limit to the effective surface tension. The effective surface tension of a water/air interface cannot increase indefinitely as the phospholipid concentration becomes so small that the bubble ruptures and the phospholipids segregate in lipid islands on the interface and the surface tension recovers to that of the water/air interface ($\sigma = 0.072$ N/m). Therefore the shell elasticity decreases to zero for larger oscillation amplitudes. For a bubble with a known resonance frequency the "compression-only" behavior of a phospholipid microbubble quantified by A_0/A_1^2 provides a direct measure for the initial state of the phospholipid shell. Furthermore, assuming the resonance frequency of the bubble is known the relation between A_0 and A_1^2 for different oscillation amplitudes A_1 can be fitted to the full numerical model proposed by Marmottant *et al.* with the variation of only one parameter $\sigma(R_0)$. This fit will therefore provide an accurate measure of the initial surface tension of the bubble. This provides a quantitative way to dynamically measure the phospholipid concentration on the interface of the bubble. This quantitative and qualitative information deduced from the "compression-only" behavior of a phospholipid coated microbubble will also help to predict other non-linear properties of these microbubbles. It will be shown in the following chapter of this thesis, Chapter 4, that also the subharmonic behavior of phospholipid-coated microbubbles is shown to strongly depend on the initial surface tension of the microbubble $\sigma(R_0)$.

3.7 Conclusions

In this chapter we have investigated the negative time average offset of the initial bubble radius of acoustically driven oscillating phospholipid coated microbubbles, often referred to as "compression-only" behavior. We have linearized the model proposed by Marmottant *et al.* [9] up to second order to show that the negative time average offset results from an initial shell elasticity that rapidly increases with bubble radius. This is known to happen for statically collapsing phospholipid monolayers [14]. We propose to quantify the "compression-only" behavior of a microbubble according to its second order time average offset amplitude A_0. From the linearized equations it follows that the negative time average offset A_0 is strongly correlated with the fundamental oscillation amplitude A_1^2. We also show both experimentally and from numerical simulations that for larger oscillation amplitudes A_1^2 the negative time average offset A_0 saturates. This effect is shown to be correctly described by the full numerical model proposed by Marmottant *et al.* when the break up tension as proposed in this model is set to $\sigma_{max} = 0.072$ N/m, i.e. the surface tension of water. The saturation is shown to result from a decrease of the shell elasticity for larger oscillation amplitudes when the maximum effective surface tension/break-up tension is reached for low surface concentrations of phospholipids. Finally, we show that the relation between A_0 and A_1^2 in the full numerical model proposed by Marmottant *et al.* is predominately determined by the initial effective surface tension of the phospholipid shell $\sigma(R_0)$. For this reason a best fit of the experimentally determined relation between A_0 and A_1^2 with the full numerical model of Marmottant *et al.* provides an accurate method to determine $\sigma(R_0)$.

References

[1] P. N. Burns, J. E. Powers, D. Hope Simpson, A. Brezina, A. Kolin, C. T. Chin, and T. Fritzsch, “Harmonic imaging: New imaging and doppler method for contrast enahanced us”, Radiology **185**, 142 (1992).

[2] V. Mor-Avi, E. G. Caiani, K. A. Collins, C. E. Korcarz, J. E. Bednarz, and R. M. Lang, “Combined assessment of myocardial perfusion and regional left ventricular function by analysis of contrast-enhanced power modulation images”, Circulation **104**, 352–357 (2001).

[3] D. Hope Simpson, C. T. Chin, and P. N. Burns, “Pulse inversion doppler: a new method for detecting nonlinear echoes from microbubble contrast agents”, IEEE Trans. Ultrason. Ferroelec. Freq. Contr. **46**, 372–382 (1999).

[4] N. de Jong and L. Hoff, “Ultrasound scattering properties of albunex microspheres”, Ultrasonics **31** (1993).

[5] C. C. Church, “The effect of an elastic solid surface layer on the radial pulsations of gas bubbles”, J. Acoust. Soc. Am. **97**, 1510 – 1521 (1995).

[6] L. Hoff, P. C. Sontum, and J. M. Hovem, “Oscillations of polymeric microbubbles: effect of the encapsulating shell”, J. Acoust. Soc. Am. **107**, 2272–2280 (2000).

[7] N. de Jong, M. Emmer, C. T. Chin, A. Bouakaz, F. Mastik, D. Lohse, and M. Versluis, ““Compression-Only” behavior of phospholipid-coated contrast bubbles”, Ultrasound Med. Biol. **33** (2007).

[8] M. Emmer, A. van Wamel, D. E. Goertz, and N. de Jong, “The onset of microbubble vibration”, Ultrasound Med. Biol. **33**, 941–949 (2007).

[9] P. Marmottant, S. van der Meer, M. Emmer, M. Versluis, N. de Jong, S. Hilgenfeldt, and D. Lohse, “A model for large amplitude oscillations of coated bubbles accounting for buckling and rupture”, J. Acoust. Soc. Am. **118**, 3499 – 3505 (2005).

[10] M. I. Sández, A. Suárez, and A. Gil, “Surface pressure-area isotherms and fluorescent behavior of phospholipids containing labeled pyrene”, J. Coll. Interf. Sci **250**, 128–133 (2002).

[11] F. Pétriat, E. Roux, J. C. Leroux, and S. Giasson, “Study of molecular interactions between a phospholipidic layer and a ph-sensitive polymer using the langmuir balance technique”, Langmuir **20**, 1393–1400 (2004).

[12] X. Wen and E. I. Franses, “Adsorption of bovine serum albumin at the air/water interface and its effect on the formation of dppc surface film”, Colloid. Surface. A **190**, 319–332 (2001).

[13] C. C. Cheng and C. H. Chang, “Retardation effect of tyloxapol on inactivation of dipalmitoyl phosphatidylcholine surface activity by albumin”, Langmuir **16**, 437–441 (2000).

[14] K. Y. C. Lee, “Collapse mechanisms of langmuir monolayers”, Ann. Rev. Phys. Chem. **59**, 771–791 (2008).

[15] C. T. Chin, C. Lancee, J. Borsboom, F. Mastik, M. E. Frijlink, N. de Jong, M. Versluis, and D. Lohse, “Brandaris 128: A digital 25 million frames per second camera with 128 highly sensitive frames”, Rev. Sci. Instr. **74**, 5026–5034 (2003).

[16] K. Sarkar, W. T. Shi, D. Chatterjee, and F. Forsberg, “Characterization of ultrasound contrast microbubbles using in vitro experiments and viscous and viscoelastic interface models for encapsulation”, J. Acoust. Soc. Am. **118**, 539–550 (2005).

[17] J. B. Keller and M. J. Miksis, “Bubble oscillations of large amplitude”, J. Acoust. Soc. Am. **68**, 628 – 633 (1980).

[18] R. Löfstedt, K. Weninger, S. Putterman, and B. P. Barber, “Sonoluminescing bubbles and mass diffusion”, Phys. Rev. E **51**, 4400 – 4410 (1995).

[19] S. van der Meer, B. Dollet, M. Voormolen, C. T. Chin, A. Bouakaz, N. de Jong, M. Versluis, and D. Lohse, “Microbubble spectroscopy of ultrasound contrast agents”, J. Acoust. Soc. Am. **121**, 648–656 (2007).

[20] A. I. Eller, “Damping constants of pulsating bubbles”, J. Acoust. Soc. Am. **47**, 1469–1470 (1970).

[21] D. L. Miller, “Ultrasonic detection of resonant cavitation bubbles in a flow tube by their second-harmonic emissions”, Ultrasonics **19**, 217 (1981).

[22] M. Overvelde, V. Garbin, J. Sijl, B. Dollet, N. de Jong, D. Lohse, and M. Versluis, “The non-linear behaviour of phospholipid coated microbubbles at low acoustic pressure is dominated by buckling of the shell”, in preperation .

[23] V. Garbin, D. Cojoc, E. Ferrari, E. Di Fabrizio, M. L. J. Overvelde, S. M. van der Meer, N. de Jong, D. Lohse, and M. Versluis, “Changes in microbubble dynamics near a boundary revealed by combined optical micromanipulation and high-speed imaging”, Appl. Phys. Lett. **90**, 114103–3 (2007).

4

Subharmonic behavior of phospholipid-coated ultrasound contrast agent microbubbles [‡]

Unlike tissue, coated microbubbles are able to scatter sound subharmonically. Therefore, subharmonic behavior of coated microbubbles can be used to enhance the contrast in ultrasound contrast imaging. Theoretically, a threshold amplitude of the driving pressure can be calculated above which subharmonic oscillations of microbubbles are initiated. Interestingly, earlier experimental studies on phospholipid coated microbubbles demonstrated that the measured threshold for these bubbles is much lower than predicted by the traditional viscoelastic shell models. This chapter presents an experimental study on the subharmonic behavior of individual differently sized BR14 (Bracco Research S.A., Geneva, Switzerland) coated microbubbles with initial radii between 2.2 and 4.8 micrometer. The subharmonic behavior was studied as a function of both the amplitude and the frequency of the driving pressure. The radial response of the microbubbles to the different driving pressures was recorded with the Brandaris ultrahigh-speed camera. As ex-

---

[‡] Submitted as: Jeroen Sijl, Benjamin Dollet, Marlies Overvelde, Valeria Garbin, Timo Rozendal, Nico de Jong, Detlef Lohse and Michel Versluis, ”Subharmonic behavior of phospholipid-coated ultrasound contrast agent microbubbles”, Journal of the Acoustical Society of America (2009).

pected from theory, this experimental study shows that the threshold pressure is minimal around a driving pressure frequency equal to twice the resonance frequency of the bubble. Furthermore, for certain bubble sizes we found a threshold pressure as low as 5 kPa. An explanation for this low threshold pressure is provided by the model proposed by Marmottant et al. [1]. We show that the change in the elasticity of the bubble shell as a function of bubble radius, R*, as proposed in this model, is responsible for the enhancement of the non-linear subharmonic behavior of phospholipid-coated Ultrasound Contrast Agent microbubbles.*

4.1 Introduction

Microbubbles scatter ultrasound effectively and non-linearly, which makes them ideal contrast agents for medical ultrasound imaging. The bubbles are coated with a protein, lipid or polymer layer and they are filled with air or an inert gas. Ultrasound contrast agents are clinically used on a daily basis to visualize blood flow at the microvascular level to image organ perfusion in e.g the liver, kidney and the myocardium[2]. Contrast enhancement is expressed in the ratio between the response of microbubbles in the blood pool and that of the surrounding tissue, termed the contrast-to-tissue ratio (CTR). Improvement of the CTR for current contrast imaging modalities such as power modulation [3] and pulse inversion imaging [4] is accomplished by exploiting the non-linear response of the microbubbles, predominantly at the second harmonic frequency of the driving frequency [5, 6]. The typical enhancement of the CTR in non-linear harmonic imaging is 40 dB. The contrast enhancement is limited, however, for deep tissue imaging through non-linear propagation of the ultrasound. Linear scattering of the generated second harmonic component of the driving pulse interferes with the bubble's second harmonic response. Non-linear propagation of the ultrasound is limited on the other hand to higher harmonics of the driving frequency. For this reason the subharmonic response of the bubbles at half the driving frequency has received increased interest for ultrasound contrast imaging [7]. Moreover the subharmonic response is attenuated less than both the fundamental and higher harmonic bubble responses. Given the transducer bandwidth limitations, subharmonic imaging is particularly interesting for high frequency imaging applications[8, 9].

Subharmonic bubble responses were first described following experimental observations by Esche [10] already in 1952. Additional experimental work has been conducted to investigate the nature of this non-linear behavior [11, 12] followed by theoretical descriptions of subharmonic behavior of bubbles in a sound field [13–17]. Prosperetti [15] showed through a weakly non-linear analysis of the Rayleigh-Plesset equation that the subharmonic behaviour of bubbles can only exist if the driving pressure amplitude exceeds a threshold pressure. It was found that the threshold pressure for subharmonic behavior is minimum when the bubble is driven at a frequency twice its resonance frequency. It was also shown that the threshold pressure increases for increased damping [13, 15, 18]. The viscoelastic shell of ultrasound contrast agent microbubbles is known to increase the damping considerably [19–21]. Therefore, it has always been suggested that the threshold pressure to excite subharmonic behavior for coated microbubbles is increased. Shankar et al.[22] studied the subharmonic behavior of coated bubbles following the analysis of Prosperetti[15] and confirmed by using a purely viscoelastic shell model as by de Jong [19], Church [23], or Hoff [24] that indeed the threshold for subharmonic generation is increased as a result of the increased damping.

There exists, however, experimental evidence in literature showing that for both the albumin-coated contrast agents Optison™ and Albunex® and the phospholipid-coated contrast agent SonoVue® the threshold pressure to excite subharmonic behavior is lower than that of uncoated bubbles [7, 22, 25–30]. Other work reports no significant change in the threshold pressure, neither for albumin-coated bubbles [31] nor for the phospholipid-coated Definity™ contrast agent microbubbles[32].

Here, we show that a lower threshold for the initiation of subharmonic behavior of phospholipid-coated microbubbles can be explained with the model proposed by Marmottant et al.[1]. Similar to Shankar et al.[22] we employ a weakly non-linear analysis along the earlier work on free bubbles by Prosperetti [15], and instead of using a purely viscoelastic model, we assume the shell elasticity of the phospholipid shell varies with bubble radius, R. It is shown that the change in the elasticity of the bubble shell as a function of, R, as also proposed in the model of Marmottant et al., is responsible for the enhancement of the non-linear subharmonic behavior of phospholipid-coated Ultrasound Contrast Agent microbubbles.

Furthermore we have used ultra-high-speed imaging with the Brandaris camera [33] to characterize the subharmonic behavior of individual microbubbles from the experimental agent BR14, which contains microbubbles with a phospholipid shell and a perfluorocarbon-gas core (Bracco Research S.A., Geneva,

Switzerland). With this setup, the full subharmonic resonance and threshold behaviour of individual coated microbubbles is investigated for different low amplitude driving pressures for different frequencies of around two times the resonance frequency of the microbubbles.
Details of the model and the weakly non-linear analysis will be presented in Sec. 4.2. The experimental setup is discussed in Sec. 4.3. In Sec. 4.4 the experimental results are presented and compared with the full numerical model of Marmottant *et al.*. Finally we end with a discussion in Sec. 4.5 and our conclusions in Sec. 4.6.

4.2 Shell modelling

4.2.1 Weakly non-linear analysis

The most general description of the dynamics of phospholipid coated microbubbles is given by,

$$\begin{aligned}
&\rho\left(R\ddot{R}+\frac{3}{2}\dot{R}^2\right)\\
&=\left(P_0+\frac{2\sigma(R_0)}{R_0}\right)\left(\frac{R_0}{R}\right)^{3\gamma}\left(1-\frac{3\gamma\dot{R}}{c}\right)\\
&-\frac{2\sigma(R)}{R}-4\mu\frac{\dot{R}}{R}-4\kappa_s\frac{\dot{R}}{R^2}-P_0-P_A(t).
\end{aligned}\tag{4.1}$$

Here, the radius of the bubble is described by $R(t)$ and its velocity and acceleration are given by $\dot{R}$ and $\ddot{R}$, respectively. The initial bubble radius is given by R_0 and the ambient pressure by P_0. The liquid viscosity is described by $\mu = 10^{-3}$ Pa s, its density by $\rho = 10^3$ kg/m^3 and the speed of sound in the liquid is $c = 1500$ m/s. The applied acoustic pressure pulse is described by $P_A(t)$. We approximate the microbubble oscillations as adiabatic. Therefore we assume the polytropic exponent γ to be the ratio of the specific heats of the gas inside the bubble. For the experimental agent BR-14 the gas core consists of perfluorocarbon-gas with $\gamma = C_p/C_v = 1.07$ [1, 21]. Thermal damping is accounted for by a slight increase of the liquid viscosity $\mu = 2\cdot10^{-3}$ Pa s. The effect of the phospholipid coating is taken into account by the shell viscosity κ_s and an effective surface tension that is assumed to depend on the concentration of phospholipid molecules on the surface of the bubble and thus on the radius of the bubble $\sigma(R)$. In the earlier models [19, 24] the effective surface tension is assumed to increase linearly with bubble , $\sigma(R) = 2\chi(R/R_0 - 1)$, where χ is the shell elasticity. In the previous chapter we have shown that a linear relation between σ and R is not sufficient to describe the observed "compression-only" behavior of phospholipid coated microbubbles. We show that also the shell elasticity should vary with bubble radius $\chi(R)$ as in the model proposed by Marmottant *et al.* [1].

Depending on the relation $\sigma(R)$ also the subharmonic behavior of phospholipid coated microbubbles as predicted by Eq. 4.1 changes. To investigate the effect of $\sigma(R)$ on the subharmonic response, Eq. 4.1 can be solved numerically for different functions $\sigma(R)$. However to come to a more fundamental understanding of the effect of $\sigma(R)$, i.e. the phospholipid coating, on the subharmonic behavior of ultrasound contrast agents it is insightful to solve Eq. 4.1 analytically. Hereto we perform a weakly non-linear analysis of Eq. 4.1 where we follow the approach of Prosperetti [15, 16, 18, 22]. The principal steps of the weakly non-linear analysis will be repeated here. As a most general approximation we assume $\sigma(R)$ for small oscillations around R_0 can be described as a second order Taylor expansion around $\sigma(R_0)$.

$$\sigma(R) = \sigma(R_0) + 2\chi_{\mathrm{eff}}\left(\frac{R}{R_0} - 1\right) + \frac{1}{2}\zeta_{\mathrm{eff}}\left(\frac{R}{R_0} - 1\right)^2 \tag{4.2}$$

If we define for any function $\sigma(R)$

$$\chi_{\mathrm{eff}} = \frac{1}{2} R_0 \frac{\partial \sigma(R)}{\partial R}\bigg|_{R_0} \tag{4.3}$$

$$\zeta_{\mathrm{eff}} = R_0^2 \frac{\partial^2 \sigma(R)}{\partial R^2}\bigg|_{R_0} \tag{4.4}$$

Then, χ_{eff} and ζ_{eff} are the effective shell elasticity around the equilibrium point R_0. Where in the full numerical model of Marmottant *et al.* $\chi(R)$ and $\zeta(R)$ depend on the bubble radius, R the effective shell elasticity χ_{eff} and ζ_{eff} are constants. The shell elasticity as determined by van der Meer *et al.* [21] for BR14 was assumed to be independent of the bubble radius, R, and is therefore equal to χ_{eff}

We can show that the results of the weakly non-linear analysis presented in the following are independent of the choice of the initial surface tension $\sigma(R_0)$. To simplify the calculations we therefore assume $\sigma(R_0)$ to be zero.

We insert Eq. 4.2 into Eq. 4.1 and assume the radius R is of the form

$$R = R_0(1+x), \tag{4.5}$$

where x is small. Following Prosperetti [15] we define a dimensionless timescale, frequency and driving pressure amplitude,

$$\tau = \sqrt{\frac{P_0}{\rho}}\frac{t}{R_0}, \quad \omega = R_0\Omega\sqrt{\frac{\rho}{P_0}}, \quad \xi = \frac{P_a}{P_0} \tag{4.6}$$

where Ω is the dimensional driving frequency. P_a is the driving pressure amplitude. Because we assume the surface tension at rest $\sigma(R_0)$ to be zero, the pressure inside the bubble is equal to P_0.

Inserting all these relations into Eq. 4.1 and performing a series expansion in x and ignoring third and higher order terms we obtain,

$$\begin{aligned}\frac{d^2x}{d\tau^2} + \omega_0^2 x = & -\frac{3}{2}\left(\frac{dx}{d\tau}\right)^2 + \alpha_1 x^2 - \xi x \cos(\omega\tau) \\ & -2b\frac{dx}{d\tau} + \xi\cos(\omega\tau).\end{aligned} \tag{4.7}$$

where we have assumed the driving pressure to be described as $P_A/(P_a P_0) = \xi \cos(\omega\tau)$. Equation 4.7 is the same as Eq. (4) from Prosperetti [15] except for the third order terms which we neglect since we are only interested in the solution of this equation for $\omega \approx 2\omega_0$, for which the second-order terms are sufficient [15].

Furthermore we have defined

$$\omega_0^2 = 3\gamma + \frac{4\chi_{eff}}{P_0 R_0}, \tag{4.8}$$

$$b = \frac{2\mu}{R_0\sqrt{\rho P_0}} + \frac{2\kappa_s}{R_0^2\sqrt{\rho P_0}} + \frac{3\gamma}{2c}\sqrt{\frac{P_0}{\rho}}, \tag{4.9}$$

$$\alpha_1 = \frac{9}{2}\gamma(\gamma+1) - \frac{(\zeta_{eff} - 8\chi_{eff})}{P_0 R_0}, \tag{4.10}$$

Note that the resonance frequency in dimensional form follows directly from Eq. 4.8 inserted into Eq. 4.6. Around $\omega \approx 2\omega_0$ the solution of Eq. 4.7 reads

$$\begin{aligned} x = {} & \frac{\xi}{\sqrt{(\omega^2-\omega_o^2)^2+4b^2\omega^2}}\cos(\omega\tau+\delta) \\ & +C\cos\left(\frac{1}{2}\omega\tau+\varphi\right), \end{aligned} \tag{4.11}$$

where δ is the phase angle of the pure harmonic solution which satisfies

$$\tan\delta = \frac{2b\omega}{\omega^2-\omega_0^2}. \tag{4.12}$$

The amplitude of the first subharmonic solution either vanishes: $C = 0$, or becomes

$$C = \sqrt{\frac{\omega_o^2-\frac{1}{4}\omega^2+g_1\xi^2+\sqrt{\beta^2\xi^2-\omega^2b^2}}{g_0}}, \tag{4.13}$$

where

$$\beta = \left|\frac{1}{2}-\frac{\alpha_1-\frac{3}{4}\omega^2}{\omega_0^2-\omega^2}\right|, \tag{4.14}$$

$$\begin{aligned} g_0 = {} & \alpha_1\left(\frac{\alpha_1-\frac{3}{8}\omega^2}{\omega_0^2}+\frac{1}{2}\frac{\alpha_1+\frac{3}{8}\omega^2}{\omega_0^2-\omega^2}\right) \\ & +\frac{3}{8}\omega^2\left(\frac{1}{4}-\frac{\alpha_1+\frac{3}{8}\omega^2}{\omega_0^2-\omega^2}\right), \end{aligned} \tag{4.15}$$

and:

$$\begin{aligned} g_1 = {} & \frac{\alpha_1}{\omega_0^2(\omega_0^2-\omega^2)}\left(1-\frac{\alpha_1-\frac{3}{2}\omega^2}{\omega_0^2-\omega^2}\right) \\ & -\frac{3}{4}\frac{\omega^2}{(\omega_0^2-\omega^2)^2}-\frac{1}{\omega_0^2-\omega^2} \\ & +\left(\omega_0^2-\frac{9}{4}\omega^2\right)\left(\frac{\alpha_1+\frac{3}{4}\omega^2}{\omega_0^2-\omega^2}-\frac{1}{2}\right)\left(\frac{1}{2}-\frac{\alpha_1-\frac{9}{4}\omega^2}{\omega_0^2-\omega^2}\right), \end{aligned} \tag{4.16}$$

Note that near $\omega = 2\omega_0$ all three quantities, β, g_0 and g_1 are positive.

Theoretically the solution from Eq. 4.13 can only exist if the term $\beta^2\xi^2 - \omega^2 b^2$ is positive. This determines the well known theoretical threshold for the existence of subharmonics

$$\xi_{th}(\omega) = \frac{\omega b}{\beta} \tag{4.17}$$

The threshold determines the regime where the subharmonic solution is stable. However, as discussed by Prosperetti and others [13, 18], depending on the initial conditions the subharmonic solution may still not exist. Another threshold is provided by the regime where the harmonic solution of Eq. 4.11 becomes unstable. In this regime the only stable solution is the subharmonic solution. This threshold is given by [13, 18]

$$\begin{aligned}\xi_{in}(\omega) = &\sqrt{\frac{\beta^2 - 2g_1\left(\omega_0^2 - \frac{1}{4}\omega^2\right)}{2g_1^2}} \\ &- \sqrt{\frac{\sqrt{\beta^4 - 4g_1\left[\left(\omega_0^2 - \frac{1}{4}\omega^2\right)\beta^2 + g_1\omega^2 b^2\right]}}{2g_1^2}},\end{aligned} \tag{4.18}$$

which for $\omega = 2\omega_0$ reduces to $\xi_{in} = \xi_{th}$

From Eq. 4.17 it is clear that the threshold for subharmonics increases with increased damping. However from Eq. 4.10 and Eq. 4.14 it follows that β and ξ_{th} vary with $\zeta_{eff} - 8\chi_{eff}$, determined by the initial condition of the phospholipid shell. In Fig. 4.1 we have plotted ξ_{th} at $\omega = 2\omega_0$ as a function of $\zeta_{eff} - 8\chi_{eff}$ for the linearized model from Prosperetti [15] and for the coated bubble model with $\sigma(R)$ described by Eq. 4.2 for $R_0 = 3.8$ µm. The damping for the coated bubble is determined by Eq. 4.9 where we assume the shell viscosity is equal to $\kappa_s = 3 \cdot 10^{-8}$ kg/s as determined by van der Meer *et al.* for the same type of bubbles [21]. This brings the total damping for the coated bubble to $b_{coated} = 0.5$. For the uncoated bubble the damping is determined by the bubble size and γ only, bringing the total damping of the uncoated bubble to $b_{free} = 0.1$. We observe that depending on the initial condition of the shell $\zeta_{eff} - 8\chi_{eff}$, the threshold for a coated bubble can vary. In the case $\zeta_{eff} - 8\chi_{eff}$ is large enough, the threshold for the coated bubble can be lower than the threshold for an uncoated bubble.

This provides a possible explanation that even for a fivefold increase of the damping as a result of the shell, the threshold for the existence of subharmonics for coated bubbles can be lower than for uncoated bubbles depending on

the initial conditions of the bubble shell.
The ultrasound contrast agent models with a purely elastic shell regime [19, 20, 23] cannot predict this decrease in threshold pressure as a function of the initial conditions since in these models ζ_{eff} is either zero or of the same order as χ_{eff}, hence $|\zeta_{\mathrm{eff}} - 8\chi_{\mathrm{eff}}|$ remains about 1 (N/m), which is too low to explain subharmonic enhancement for contrast agents. In the model proposed by Marmottant we can identify that close to the transition point from the elastic to the buckling regime, $\chi(R)$ changes rapidly from $\chi \approx 2.5$ N/m to $\chi = 0$ N/m, corresponding to a large $\zeta(R)$. In fact, in the current model of Marmottant $\zeta(R) = \infty$ at the transition points. At the transition points $\zeta(R_0) \sim \zeta_{\mathrm{eff}}$ can be much higher than $\chi(R_0) \sim \chi_{\mathrm{eff}}$, hence $|\zeta_{\mathrm{eff}} - 8\chi_{\mathrm{eff}}|$ can be large enough to enable subharmonic enhancement for contrast agents. In Fig. 4.2 we have fixed χ_{eff} = 0.55 N/m (corresponding to the average shell elasticity χ_{eff} found by van der Meer *et al.* [21] for the same type of bubbles) and $\zeta_{\mathrm{eff}} = 502.2$ N/m. In Fig. 4.2 we have plotted both ξ_{th} and ξ_{in} as a function of ω/ω_0 for both the free bubble and the coated bubble model with $\sigma(R)$ described by Eq. 4.2. As a result of the initial conditions we observe that both thresholds (ξ_{th} and ξ_{in}) for the coated microbubble are as low as 6 kPa, much lower than those for the free gas bubble where the threshold is near 90 kPa.

4.2.2 Numerical Model

The analytical solutions presented in the previous section provide a fundamental understanding of the source of subharmonic behavior of coated microbubbles. However, for these calculations we have assumed an infinitely long driving pressure pulse and a sufficiently small amplitude of oscillation neglecting higher order terms in Eq. 4.7. In practice, the driving pressure pulse has a finite length and the amplitudes of oscillation of the microbubbles exceed the small amplitude limit. In the following we will therefore solve Eq. 4.1 numerically. Solving the equation numerically requires a model for the relation between the bubble radius and the effective surface tension $\sigma(R)$. We will assume $\sigma(R)$ to be described as proposed in the model of Marmottant *et al.* [1]. The relation for $\sigma(R)$ as proposed by Marmottant *et al.* [1] both limits the effective surface tension between the physcial boundaries $\sigma(R) = 0$ and $\sigma(R) = \sigma_{\mathrm{water}}$. In the model of Marmottant *et al.* $\zeta(R)$ is undefined near the two transition points from the ”buckling regime” to the ”elastic regime” and from the ”elastic regime” to the ”ruptured regime”. In order to have $\zeta(R)$ defined for all R we assume $\zeta(R)$ in the two transition regimes to be defined

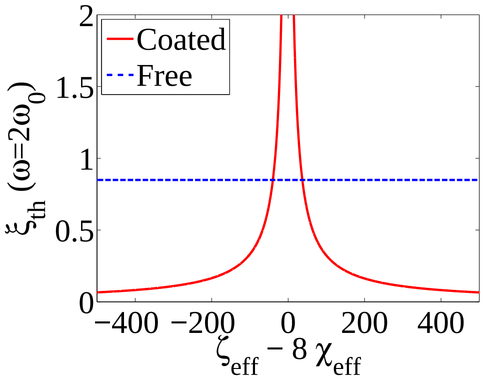

Figure 4.1: The mathematical threshold ξ_{th} *at* $\omega/\omega_0 = 2$ *given by Eq. (4.17) plotted as a function of the term* $\zeta_{eff} - 8\chi_{eff}$ *for* $R_0 = 3.8$ µ*m with fixed* $\chi_{eff} = 0.55$ *N/m. We observe that if* $|\zeta_{eff} - 8\chi_{eff}|$ *is large enough, the threshold for a coated bubble can decrease below the threshold of a free gas bubble despite its additional shell damping. The damping for the free gas bubble is determined by the reradiation damping and the liquid viscosity, for this bubble* $b = 0.1$*. For the coated bubble model the shell damping is added where the shell viscosity is taken* $3 \cdot 10^{-8}$ *kg/s resulting in an extra damping* $b_{shell} = 0.4$.

by the two quadratic functions introduced in chapter 3. Furthermore from Overvelde *et al.* [34] we know the shell elasticity in the elastic regime for these type of microbubbles is described by $\chi_{max} = 2.5$ N/m.

The shell parameters of the model that are undetermined up to now are the initial surface tension $\sigma(R_0)$, the shell viscosity κ_s and finally the value of ζ in the two transition regimes of the effective surface tension. From the theoretical threshold for the existence of subharmonics (Eq. 4.17) we expect that these three shell parameters strongly influence the subharmonic behavior. The shell viscosity increases the damping b of the system and is therefore expected to decrease the subharmonic response. On the other hand, the initial surface tension $\sigma(R_0)$ and the quadratic transition determined by ζ strongly affect ζ_{eff} and thus β in Eq. 4.17. The strong effect of $\sigma(R_0)$ on the subharmonic behavior of phospholipid coated microbubbles is shown in Fig. 4.3. In Fig. 4.3 two different responses of a 3.8 µm radius bubble driven at an acoustic pressure of 40 kPa with a frequency of 2.4 MHz. We observe that the bubble with a small initial surface tension, $\sigma(R_0)$ close to the "buckling regime" shows a large subharmonic response, in contrast to the response of a

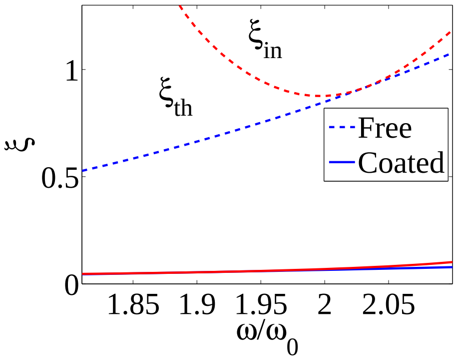

Figure 4.2: The mathematical threshold ξ_{th} *(blue) and the instability threshold* ξ_{in} *(red) as a function of* ω/ω_0 *for* $R_0 = 3.8$ *μm. The damping for the coated and the free bubble are the same as in Fig. 4.1, i.e. the damping coefficient for the coated bubble is five times as large as for the uncoated bubble. Even so, the threshold for the coated bubble is only 6 kPa, much lower than for the uncoated bubble which has a threshold of 90 kPa. This decrease of the threshold for the coated bubble results from the discontinuity in the effective surface tension described by* $\chi_{eff} = 0.55$ *N/m and* $\zeta_{eff} = 502.2$ *N/m (*$\zeta_{eff} - 8\chi_{eff} = 500$ *N/m)*

bubble with an initial surface tension in the ”elastic regime”, no subharmonic response is observed. Note that the fundamental response for both bubbles is similar and is almost unaffected by $\sigma(R_0)$.

To investigate the effect of the shell parameters of the model on the subharmonic behavior, a parameter study was conducted. The results are shown in Fig. 4.4. In the parameter study the driving pressure amplitude and the driving pressure frequency were kept constant at 40 kPa and 2.4 MHz. This driving frequency corresponds to two times the resonance frequency of the bubble. The shape of the driving pressure pulsed shown in Fig. 4.3(a) is the same as was used in the experiments and will be discussed in more detail in the next section. The initial bubble radius was kept constant at 3.8 μm but it was found that the results presented in Fig. 4.4 are similar for all bubbles with an initial bubble radius between 1 μm and 5 μm. Finally, while one of the shell parameters was varied the other four parameters were fixed as in Fig. 4.3, i.e. $\sigma(R_0) = 0.001$ N/m, ζ =2000 N/m, $\kappa_s = 3 \cdot 10^{-8}$ kg/s and $\chi_{max} = 2.5$ N/m.

The fundamental response in all three figures of Fig. 4.4 is observed to vary little compared to the subharmonic response which strongly depends on the value of the three shell parameters. The subharmonic threshold is observed

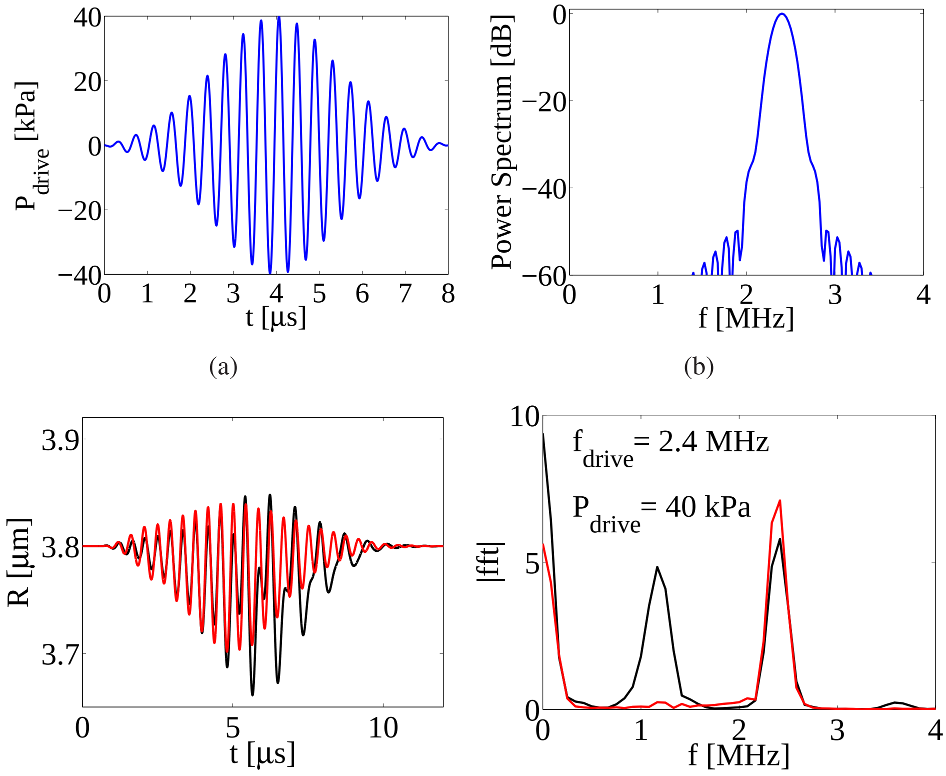

(a) (b)

(c) (d)

Figure 4.3: Top figures: An example of the driving pressure waveform (a), and (b) its corresponding power spectrum. Bottom figures: The radius time curve (c) and the corresponding Fourier transform (d) for two bubbles with a different initial surface tension $\sigma(R_0)$ *driven with the top driving pressure of 40 kPa with a frequency of 2.4 MHz. The black line represents the numerical simulation for a bubble with* $\sigma(R_0) = 0.001$ *N/m and the red line corresponds to a bubble with* $\sigma(R_0) =$ *0.01 N/m. The initial bubble radius and the other shell parameters are the same for both bubbles,* ζ *=2000 N/m,* $\kappa_s = 3 \cdot 10^{-8}$ *kg/s and* $\chi_{max} = 2.5$ *N/m.*

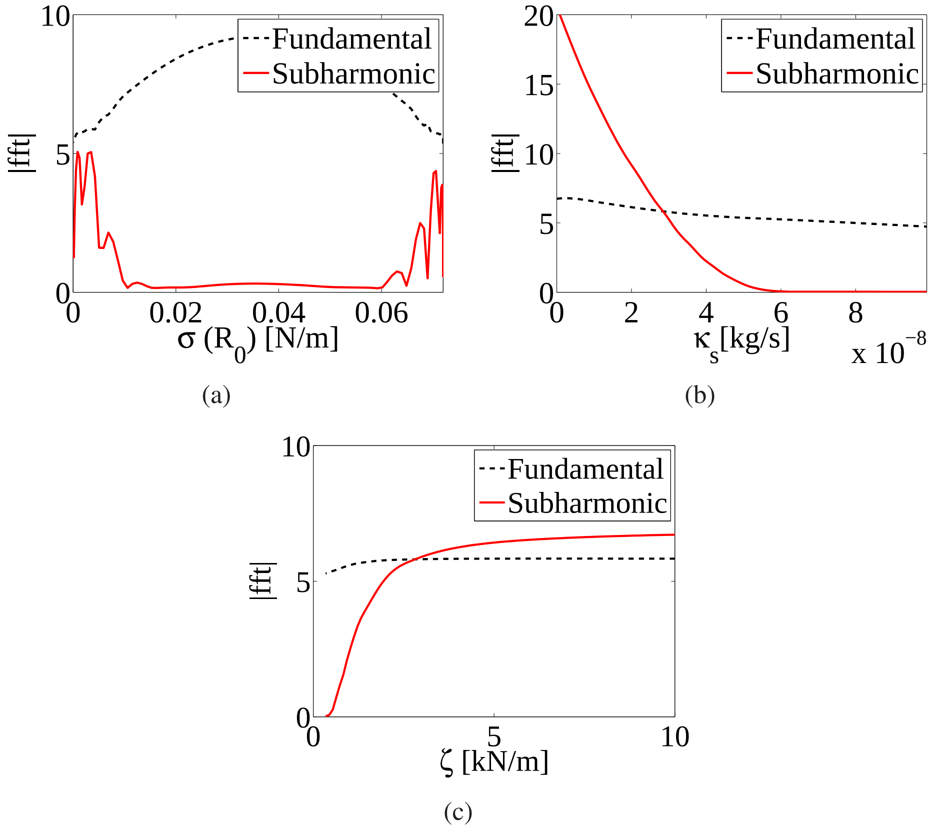

(a) (b)

(c)

Figure 4.4: The absolute value of the Fourier transforms of a parameter study on the simulated radius-time curve presented in Fig. 4.3. The fundamental response to the driving pressure of 2.4 MHz is clearly visible in all three figures while the subharmonic response is observed to strongly vary for each shell parameter varied independently. a) For $\sigma(R_0)$ *varied between 0 and* σ_{water} *the subharmonic response is only visible for the initial condition of the bubble satisfying* $\sigma(R_0) \approx 0$ *or* $\sigma(R_0) \approx \sigma_{\text{water}}$ *b) As expected the subharmonic is observed to decrease for* κ_s *increasing from 0 to* 10^{-7} *kg/s and for* ζ *increasing from 342 to 10000 N/m the subharmonic is observed to increase but for* $\zeta > 5000$ *N/m the amplitude of the subharmonic response saturates.*

to strongly depend on the damping and thus on κ_s. In Fig. 4.4(b) we observe that for $\kappa_s = 6 \cdot 10^{-8}$ kg/s the threshold for the initiation of subharmonics is 40 kPa corresponding to the driving pressure amplitude. For smaller κ_s the subharmonic response is observed to increase.

In agreement with what was found for the weakly non-linear analysis we find that the subharmonic response depends strongly on the change of the initial shell elasticity. Indeed, the subharmonic behaviour is only observed for microbubbles that have an initial surface tension close to $\sigma(R_0) \approx 0$ or $\sigma(R_0) \approx \sigma_{\text{water}}$, close to the transitions from the elastic regimes to the two other regimes corresponding to a large second derivative of the effective surface tension. The local minima observed in the subharmonic response in Fig. 4.4(a) are a result of transient effects resulting from the finite length of the driving pressure pulse. These local minima disappear for an increased length of the driving pressure pulse. As with the linearized model we can conclude that the change in the effective surface tension is of fundamental importance to be able to predict subharmonic behavior for phospholipid coated microbubbles at low driving pressure amplitudes. Furthermore a difference in the initial surface tension of bubbles explaines why in some experiments subharmonics are observed at low driving pressures while in other experiments no subharmonics are observed for similarly coated microbubbles [7, 22, 25–28, 31, 32]. Finally, the subharmonic response is also observed to increase with increasing ζ (see Fig. 4.4(c)). For an increased ζ also $\zeta_{\text{eff}} = 2R_0(\partial(\chi(R_0))/\partial R)$ increases. The transition from the elastic regime to the other two regimes in becomes sharper. Effectively the surface tension term in Fig. 4.1 is increased which results in a decrease of the threshold for the generation of subharmonics. Furthermore, the maximum subharmonic response is observed to saturate for a value of $\zeta > 5000$ N/m.

4.3 Experimental setup

The previous sections have shown the subharmonic behavior of phospholipid coated bubbles is predominately determined by the driving pressure frequency, the driving pressure amplitude, and the initial state of the phospholipid shell of the microbubble. Experimentally, the initial state of the phospholipid shell of the microbubble is hard to control whereas the driving pressure frequency and the driving pressure amplitude can be varied experimentally. Hereto we have recorded the radial dynamics of 39 different isolated microbubbles with the Brandaris ultrahigh-speed camera [33] as a function of both the driving pressure frequency and amplitude.

The experimental setup is schematically shown in Fig. 4.5. The setup consists of a cylindrical Plexiglass container that was mounted under an upright microscope (BXFM, Olympus Optical, Japan). Within the container the microbubbles were confined inside an OptiCell cell culture chamber (Thermo Fisher Scientific, Waltham, MA, USA). The acoustic transmit circuit consists of a focused 3-MHz center frequency transducer (PA168, Precision Acoustics Ltd., Dorset, UK) that was mounted under an angle of 45° under the OptiCell. A 0.2 mm needle hydrophone (Precision Acoustic Ltd., Dorset, UK) that moves in and out of the combined optical and acoustical focus was used to calibrate and align the transducer. The transmit transducer was excited with a sequence of pulses generated by an arbitrary waveform generator (Tabor Electronics Ltd, Model 8026, Haifa, Israel) and amplified by a power amplifier (ENI, Model 350L with 50 Ω input impedance, Rochester, NY). To calibrate and align the transmit transducer, a broadband chirp function was used to excite the transducer. The output response of the transducer was measured with the calibrated needle hydrophone in the focus of the transducer. From the response the transmit transfer function of the transducer was determined.

The optical focus of a 100× microscope objective (LUMFPL, Olympus Optical, Japan) was positioned onto the acoustical focus of the transducer. It was illuminated from below with a high intensity xenon flashlight (MVS 7010 XE, Perkin Elmer, Waltham, MA). A continuous-wave light source (ACE I, Schott, NY) in combination with a CCD camera (LCL-902K, Qwonn) was used to keep track of the bubble in between experiments. The image of the microscope objective was coupled into the Brandaris 128 ultra high speed imaging facility. The high-speed camera consists of 128 separate highly sensitive CCD (Charge Coupled Device) sensors that are illuminated consecutively by a rotating mirror. The mirror turbine is driven by a mass-flow controlled flow of Helium, at a revolving rate of 20000 revolutions per second corresponding to a frame rate of 25 million frames per second. Six consecutive movies of 128 frames each can be stored in a memory buffer with a time interval of 80 ms. We employed the microbubble spectroscopy method detailed in [21] to characterize the bubbles. The microbubbles were excited with a smoothly windowed driving pressure waveform with a frequency ranging from 1 to 4 MHz, all with peak rarefactional amplitudes ranging from 5 to 150 kPa and

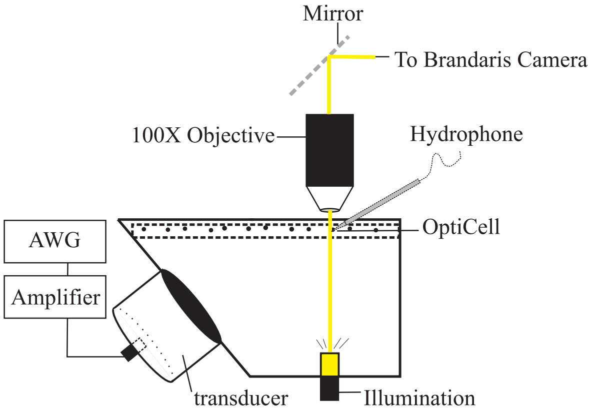

Figure 4.5: A schematic overview of the experimental setup that was used to optically record the radial dynamics of coated microbubbles located inside an optically and acoustically transparent OptiCell chamber. The driving pressure waveform produced by an arbitrary waveform generator (AWG) was amplified and transmitted by a focussed transducer. The radial dynamics were recorded through a 100× objective coupled through an inverted microscope into the Brandaris ultrahigh-speed camera.

a length of 8.9 μs. An example of a driving pressure waveform is shown in Fig. 4.3(a). In preparation of the experiment 12 driving pressure pulses were uploaded to the arbitrary waveform generator. The frequencies of each of the waveforms were varied and equally spaced near two times the resonance frequency of the microbubble. In this way the radial subharmonic resonance behavior of the bubble was quantified. The optical recordings consisted of two times six movies at a frame rate near 13 Mfps.

The movies were stored on a PC, and all data were post-processed using Matlab (The Mathworks, Natick, MA). The image sequence of the oscillating bubble was analyzed with Matlab through a semi-automatic minimum cost algorithm [21] to give the radius of the bubble as a function of time $R(t)$.

All the results discussed in this chapter were conducted with microbubbles located against the top wall of the OptiCell. However, the experimental setup is compatible with an optical tweezers setup that was coupled through the microscope into the microscope objective. With this combined setup we could also bring the microbubbles 100 μm away from the top wall. The details of this setup are described in full detail by other authors [35, 36]. To investigate the effect of the wall on the subharmonic behavior of coated microbubbles we have conducted several scans around the subharmonic resonance of different microbubbles both when the bubble was located against the top wall of the OptiCell and when brought 100μm away from the wall. Based on these experiments we conclude that a wall does not alter the subharmonic behavior of ultrasound contrast agents sufficiently to be experimentally observable in the current setup. Hereafter we therefore only discuss the results based on the setup without the optical tweezers.

4.4 Results

The study discussed here is based 39 individual microbubbles. Subharmonic responses were observed for approximately 50% of the microbubbles. The other 50% of the microbubbles could not be forced into subharmonic oscillations for the driving pressure amplitudes and/or pulse lengths employed in this study which were always smaller than 150 kPa. This finding confirms previous results by Bhagavatheeshwaran *et al.* and by Kimmel *et al.* [31, 32]. In those cases where subharmonic oscillations were observed these were initiated already at driving pressure amplitudes smaller than 40 kPa confirming the results found by several other authors [7, 22, 25–28].

Figure 4.6 shows a typical example of an ultra-high speed recording of a microbubble with an initial bubble radius of 3.8 μm. The bubble was excited with 12 different frequencies near two times its resonance frequency, which was 1.3 MHz following van der Meer *et al.* [21]. The subharmonic response is clearly visible both in the time and frequency domain. We observe a maximum for the amplitude of the subharmonic response around a driving pressure frequency of 2.4 MHz corresponding to a 1.2 MHz subharmonic oscillation. At this frequency the amplitude of the (radial) subharmonic response is even higher than the amplitude of the fundamental response. Both above and below the resonance frequency the subharmonic response decreases and a subharmonic resonance curve can be obtained similar to the resonance curve produced with microbubble spectroscopy by van der Meer *et al.* [21]. Furthermore, as expected the fundamental response of the microbubble does not show a resonance behavior since it is excited far above its resonance frequency, which also explains why the fundamental response is observed to decrease for increasing driving frequency. Finally, note that most of the responses presented in Fig. 4.6 show a zero order frequency component even though the initial bubble radius was subtracted from the radius-time curve before the Fourier transform was performed. The zero order component results from the "compression-only" behavior, i.e. the bubble appears to compress more than it expands (see chapter 3).

The experimental data is compared to the theoretical predictions. Figure. 4.7 shows a best-fit of the model of Marmottant *et al.* [1] with the radius-time curve with the maximum subharmonic response in Fig. 4.6 e. The unknown parameters of the model, ζ, the shell viscosity κ_s and the initial surface tension $\sigma(R_0)$ of the bubble are varied using the iterative fit function *fit* in Matlab . The driving pressures for the simulated and measured radius-time curve are exactly the same. The goal of the fit was not to determine the ultimate values for the three shell parameters but to see if the model proposed by Marmottant et al. is able to predict subharmonic behavior of coated microbubbles at these low driving pressure amplitudes as observed in the experiments. The agreement between the two radius-time curves is good. The best fit parameters found are in good agreement with the parameter study presented in Sec. 4.2.2 and the values found elsewhere in the literature. The best fit value for the shell viscosity $\kappa_s = 3 \cdot 10^{-8}$ kg/s is in agreement with van der Meer et al.[21]. To explain the amplitude of the subharmonic oscillations observed in Fig. 4.7 we observe in Fig. 4.4 that the amount of damping depicted by $\kappa_s = 3 \cdot 10^{-8}$ kg/s requires a large value for ζ. This is in agreement with the value for ζ found in the best fit, namely $\zeta = 2000$ N/m. Furthermore, in Sec. 4.2.2 and from the analytical solutions in Sec. 4.2.1, we found $\sigma(R_0)$ should be close to zero which is in good agreement with the best fit value found in Fig. 4.7, $\sigma(R_0) = 0.001$ N/m.

To determine the threshold pressure for the initiation of subharmonic oscillations for these coated bubbles the experiment as presented in Fig. 4.6 was repeated for different driving pressure amplitudes. The maximum response frequency for the experimentally determined subharmonic oscillations was observed to decrease from 1.4 MHz (<5 kPa) to 1 MHz (>80 kPa) for increased driving pressures. This can be attributed to a non-linear phenomenon, where the resonance frequency of the bubble decreases for increased driving pressure [15, 34]. In Fig. 4.8 the subharmonic oscillation amplitude at the maximum subharmonic response frequency is plotted as a function of the driving pressure amplitude. We observe that the threshold pressure for the initiation of subharmonic oscillations is smaller than 5 kPa, much lower than that of a free gas bubble without a shell and much lower than is expected based on the additional damping introduced by the phospholipid shell of the bubble [7, 22, 25–28]. For the 5 kPa driving pressure the only driving frequency with showing a subharmonic response was 2.8 MHz corresponding to a resonance

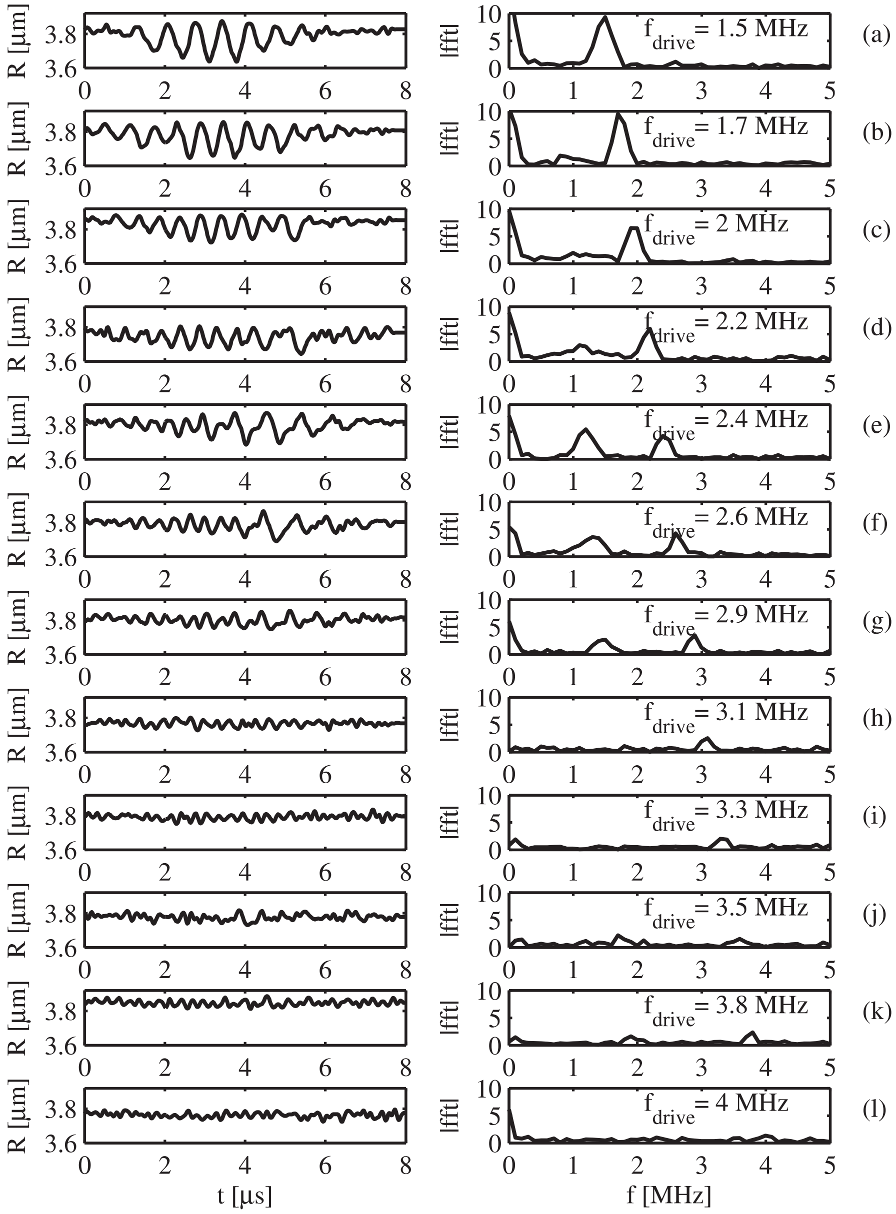

Figure 4.6: The radius-time curves (left column) of a 3.8 µm *microbubble excited with twelve different driving frequencies all with an amplitude of 40 kPa. In the corresponding absolute value of the Fourier transform of the radius-time curves (right column) we observe clear subharmonic behaviour. We can identify a subharmonic resonance curve that peaks at a driving frequency of 2.4 MHz, about twice the resonance frequency of the bubble.*

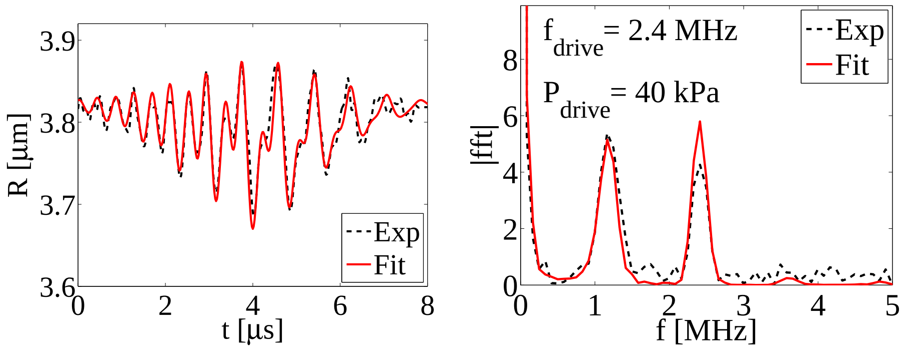

(a) (b)

Figure 4.7: The best fit with the model proposed by Marmottant et al. with the shell parameters $\chi_{max} = 2.5$ *(N/m),* $\zeta = 2000$ *N/m* $\kappa_s = 3 \cdot 10^{-8}$ *(kg/s) and* $\sigma(R_0) = 0.001$ *N/m of the fourth radius-time curve from Fig. 4.6(e) both in a) the time domain and b) in the frequency domain.*

frequency of 1.4 MHz.

Interestingly, we observe that the subharmonic amplitude decreases for increasing driving pressure amplitudes above a pressure of 80 kPa. To investigate the results in more detail we conducted numerical simulations using three different models, a free gas bubble model as described by Lotsberg et al.[25], a purely viscoelastic shell model [19] and the model proposed by Marmottant *et al.* [1]. The shell parameters for the model of Marmottant were taken from the best-fit from Fig. 4.7. For the purely viscoelastic shell model, the same shell viscosity was used however the shell elasticity was assumed to be equal to the shell elasticity found by van der Meer *et al.* [21], $\chi_{eff} = 0.55$ (N/m), who determined the shell elasticity for a purely viscoelastic shell model. The initial surface tension in the purely viscoelastic shell model is assumed to be the same as found in the best fit from Fig. 4.7. In the numerical simulations, the initial bubble radius and driving pressures were those of the experiments. As discussed before, the maximum subharmonic/harmonic response frequency varies slightly for increased driving amplitudes. Therefore, as in the experiments, we varied the driving pressure frequency around twice the resonance frequency of the bubble to find the maximum subharmonic response frequency. The maximum subharmonic oscillation amplitude for the three different models at the maximum subharmonic response frequency was plotted against the driving pressure amplitude together with the experimental data in Fig. 4.8. From this figure it is clear, the free gas bubble model starts to show subharmonic behavior for driving pressure amplitudes between 50 kPa and 80 kPa although the experimental data shows subharmonic behavior already at driving pressure amplitudes of 5 kPa. As a result of the increased damping introduced by the bubble shell, the purely viscoelastic shell model shows no subharmonics up to a driving pressure amplitude of 240 kPa. The model of Marmottant on the other hand predicts that the threshold pressure for the initiation of subharmonics almost vanishes, which is in agreement with what is found experimentally. Overall the agreement between the theoretical predictions of the model proposed by Marmottant *et al.* [1] and the experimental result is good. In both theory and experiment we observe that the oscillation amplitude at the subharmonic frequency can be as high as 4 % of the initial bubble radius already at a driving pressure amplitude of 40 kPa. Also the decrease of the subharmonic oscillation amplitude seems to be correctly predicted by the model. The same experiments and numerical simulations were conducted for two other microbubbles: one for a bubble with an initial bubble radius of 4.8 μm and one for a 2.4 μm radius bubble which are presented in Fig. 4.8(b) and Fig. 4.8(c), respectively. The shell viscosity was adapted to the initial bubble radius of the bubble in accordance with the results of van der Meer *et al.* [21], who found a shell viscosity depending on bubble size, or more precisely on dilatation rate. The shell viscosity was directly taken from the fit in Fig.8B as presented by van der Meer *et al.* [21]. For the 4.8 μm radius bubble the shell viscosity was therefore taken to be equal to $4.3 \cdot 10^{-8}$ kg/s and for the 2.4 μm radius bubble it was taken to be equal to $1.2 \cdot 10^{-8}$ kg/s. In Fig. 4.8(c) and Fig. 4.8(b) we again observe that the subharmonic threshold pressure has decreased considerably compared to the threshold pressure predicted for a free gas bubble of the same size. The purely viscoelastic shell model is unable to predict subharmonics at such low driving pressure amplitudes. Comparing a,b,c of Fig. 4.8 we observe that the maximum subharmonic oscillation amplitude of the largest bubble is comparable to the maximum subharmonic oscillation amplitude of the smallest bubble. Furthermore it is found that the threshold pressure for the initiation of subharmonic oscillations does not vary strongly with bubble radius. We also observe that for all three bubble sizes the model of Marmottant predicts a maximum for the subharmonic oscillation amplitude in between a driving pressure of 50 kPa and 100 kPa. Finally to investigate the frequency dependence of the subharmonic behavior of phospholipid coated microbubbles we

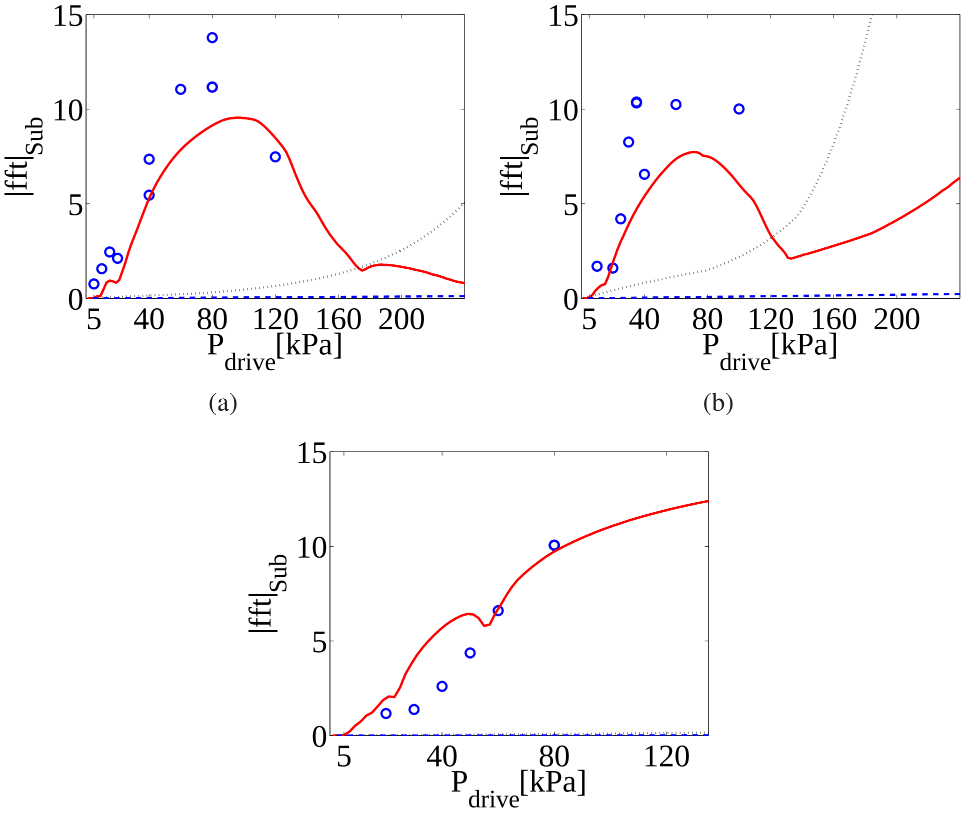

(a)

(b)

(c)

Figure 4.8: The maximum amplitude of the subharmonic oscillations of a a) 3.8 μm bubble, b) 4.8 μm and c) 2.4 μm bubble as a response to different driving pressure amplitudes. The measured responses are compared with the subharmonic responses for the same initial bubble radii predicted by three different models. The model proposed by Marmottant et al.[1] (solid red line), and a purely viscoelastic shell model (dashed blue line) and a free gas bubble model (dotted black line).

varied the driving frequency as shown in Fig. 4.6. A single-plot overview of the full frequency behavior presented in Fig. 4.6 is shown as a spectogram in Fig. 4.9(b). The horizontal axis of the figure is divided into twelve columns representing the twelve driving frequencies extracted from the twelve different movies. The horizontal axis is the response frequency corresponding to the vertical axis of the figures in the right column of Fig. 4.6. The resolution on the vertical axis is determined by the interpolation frequency we used to interpolated the radius-time curves i.e. 50 MHz. Finally, the color in Fig. 4.9(b) represents the absolute value of the Fourier transform of the radius-time curves. In the figure we have filtered out the zero order frequency component completely. Two other examples are also presented respectively in Fig. 4.9(a) and Fig. 4.9(c). In Fig. 4.10 the three fitted parameters from Fig. 4.7 are used to simulate the full (sub)harmonic resonance behavior of the same bubbles presented in Fig. 4.9. The initial surface tension and ζ were assumed to be equal to the value found in Fig. 4.7 and the shell viscosity was again assumed to vary with initial bubble radius as shown by van der Meer *et al.* [21]. The color scaling for the simulated spectra is the same as in Fig. 4.9 allowing for a quantitative comparison between the experimental an theoretical subharmonic behavior. Both the simulated spectra and the measured spectra show subharmonic resonance behavior around the same frequencies. Furthermore, we can also identify a good agreement between the absolute amplitude of the subharmonic response between the simulated and the measured spectra.

Finally, in Fig. 4.11 we have plotted all experimental data that showed clear subharmonic behavior. In this figure the maximum subharmonic response frequency is plotted against the initial bubble radius. For these experiments the driving pressure amplitude varied between 5 kPa and 100 kPa, higher driving pressures where not taken into account. However, it is clear from Fig. 4.8 that the microbubbles that did show subharmonic behavior had a maximum subharmonic response frequency that is in good agreement with the theoretical resonance frequency as predicted by Eq. (4.8) with $\chi_{\mathsf{eff}} = 0.55$ (N/m).

4.5 Discussion

From the comparison between the numerical, analytical and experimental results we conclude that the subharmonic behavior at low acoustic driving pres-

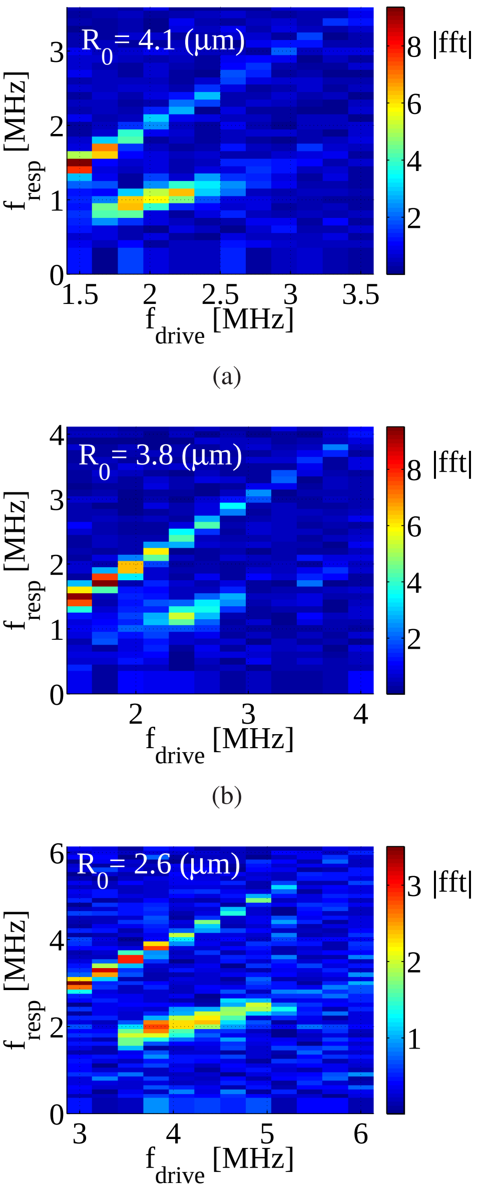

(a)

(b)

(c)

Figure 4.9: The amplitude of the Fourier transform of the radial response of three differently sized bubbles as measured with the Brandaris ultrahigh-speed camera represented by a color. The horizontal axis represents twelve different driving pressure frequencies with a fixed driving pressure amplitude of 40 kPa. The response frequency is represented by the vertical axis.

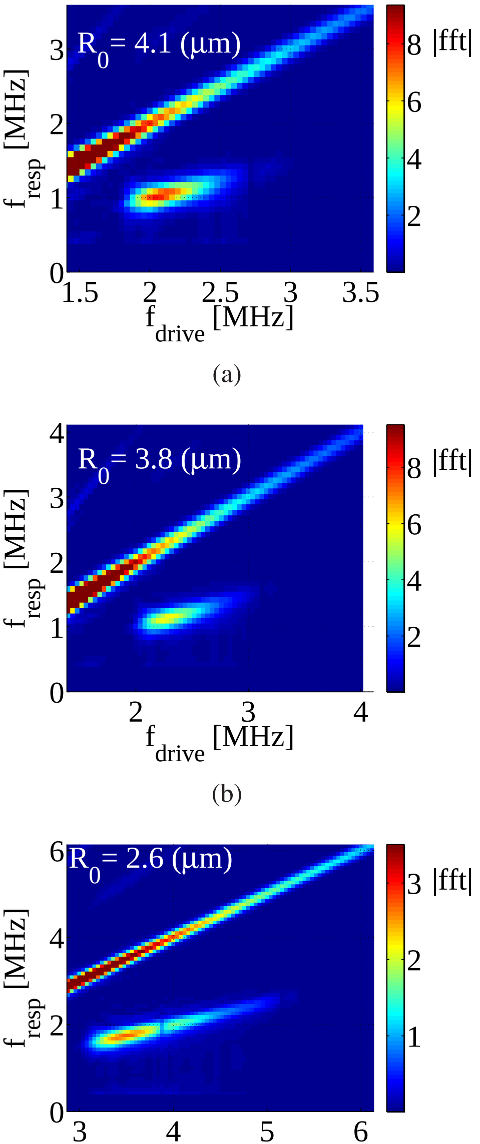

(a)

(b)

(c)

Figure 4.10: Simulated subharmonic resonance behavior of coated microbubbles with the same initial bubble radii as in Fig. 4.9 using the best fit shell parameters found in Fig. 4.7

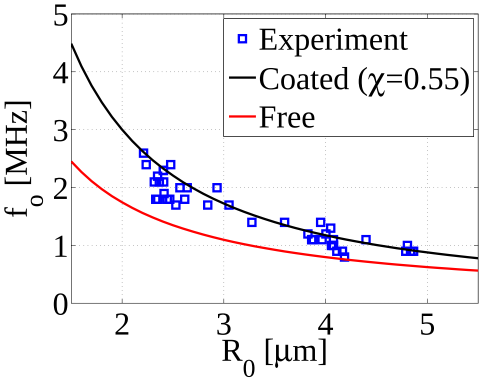

Figure 4.11: Maximum subharmonic response as a function of initial bubble radius. The dots represent all the experimental data in which subharmonic behavior was observed for driving pressure amplitudes in between $0-100$ *kPa.*

sure amplitudes can be explained by a strong change of the initial effective surface tension of the bubble shell. We can also state that especially the subharmonic behavior of phospholipid coated microbubbles is predominately determined by the initial state of the phospholipid shell. The description of the effective surface tension of a phospholipid coated microbubble as a function of bubble radius, as proposed by Marmottant *et al.* [1], could be considered a rather ad-hoc representation. However the main features responsible for the subharmonic behavior of phospholipid coated microbubbles, such as the large change of the initial shell elasticity, provides a good approximation of what is observed experimentally. The phospholipids that are present on the surface of BR-14 microbubbles, are distearoylphosphatidylcholine (DSPC), and dipalmytoylphosphatidylglycerol (DPPG). These are well known pulmonary surfactants [37] and the dynamic behavior of these surfactants is important. Hereto, researchers make use of a so called pulsating bubble surfactometer [38]. In a pulsating bubble surfactometer a bubble of around 500 μm is coated with the surfactant of interest while the radius of the bubble is a varied through an externally applied pressure, the pressure in and outside the bubble which is monitored during the oscillations provides direct information on the dynamic surface tension of the bubble.

From dynamics surface tension measurements conducted by Wen *et al.* [39] and Cheng *et al.* [40] on DPPC (similar to DPPG and DSPC) we observe indeed that the change of the shell elasticity is indeed much larger than the shell elasticity itself for an initial surface tension close to the phospholipid surface saturation concentration (see the sharp peaks for low effective surface tension and round peaks for large effective surface tension in Fig.2 of [39] and Fig.1 of [40].

Despite the research there is no final consensus on the exact form of the effective surface tension figure proposed by Marmottant *et al.* [1]. One of the main reasons is that the exact shape of the effective surface tension as a function of bubble radius, R and the initial surface tension of the bubble depends on many factors, such as the ionic strength and pH of the solution, temperature, impurities and dissolved proteins or other lipids [37]. This provides a possible explanation why around 50% of the microbubbles studied in this chapter and similar studies by others [31, 32] showed no subharmonic behaviour at low acoustic driving pressures. The surface of these bubbles could have been insufficiently saturated with phospholipids for example which results in an insufficiently large change of the initial shell elasticity.

The findings presented in this chapter could prove valuable for the application of phospholipid coated microbubbles in medical ultrasound imaging. If control over the initial conditions of the microbubbles can be achieved the subharmonic behavior of microbubbles can be enhanced improving the contrast to tissue ratio in contrast-enhanced ultrasound imaging. One way of changing and controlling the initial conditions of the phospholipid shell and thus the subharmonic behavior of the microbubble is through changing the ambient pressure. This idea has been shown by Frinking *et al.* [30] and provides new possibilities for non-invasive *in vivo* hydrostatic pressure estimations inside the heart and large vessels.

4.6 Conclusions

Through a weakly non-linear analysis we provided an explanation for the decrease of the initiation of subharmonic behavior of phospholipid coated microbubbles. We show that a decrease of the subharmonic threshold for coated microbubbles can only be explained if the shell elasticity of the bubble shell, $\chi(R)$, varies strongly with the amplitude of oscillation. Unlike the purely viscoelastic models the model of Marmottant *et al.* [1] assumes that the shell of a phospholipid coated microbubble is elastic only for small amplitude oscillations. If the bubble radius becomes smaller or larger than certain threshold radii the shell elasticity is assumed to be zero. It is shown that as a result of this change in the shell elasticity, the subharmonic behaviour of coated microbubbles is likely to occur already for low amplitude driving pressure amplitudes.

In a parameter study of the three parameters of the full numerical model we show that the initial condition for the surface tension of the bubble shell determines if or not subharmonics can occur at low amplitude driving pressures. If the initial surface tension of the bubble is sufficiently close to the ”buckling regime” and the collapse of the phospholipid monolayer from the ”elastic regime” to the ”buckling regime” determined by ζ is sufficiently abrupt subharmonic behavior is enhanced. Furthermore it is confirmed that the subharmonic behavior is enhanced for a smaller shell viscosity.

Experimentally the subharmonic radial dynamics of differently sized microbubbles was studied for different driving pressure frequencies near two times the resonance frequency of the bubble for different driving pressure amplitudes. Subharmonic oscillations were observed for bubbles insonified with driving pressures with amplitudes as low as 5 kPa. This indicates that the threshold pressure above which subharmonic oscillations may occur is smaller for phospholipid-coated microbubbles than for free gas bubbles, even though as a result of the shell viscosity these bubbles are more heavily damped.

It was found that the threshold pressure for the initiation of subharmonics is minimum at two times the resonance frequency. When the resonance frequency determined from the maximum subharmonic response was plotted as function of initial bubble radius the resulting relation was found to be in good agreement with what is found elsewhere in the literature for these type of bubbles [21].

All experimental results were correctly described by the model proposed by Marmottant *et al.* [1]. Unlike the purely viscoelastic models and a free-gas bubble model the model of Marmottant *et al.* [1] was able to quantitatively describe the subharmonic behavior of phospholipid coated microbubbles at low driving pressure amplitudes.

References

[1] P. Marmottant, S. van der Meer, M. Emmer, M. Versluis, N. de Jong, S. Hilgenfeldt, and D. Lohse, “A model for large amplitude oscillations of coated bubbles accounting for buckling and rupture”, J. Acoust. Soc. Am. **118**, 3499 – 3505 (2005).

[2] F. B. Feinstein, "The powerful microbubble: From bench to bedside, from intravascular indicator to therapeutic delivery system, and beyond.", Am. J. Physiol. Heart Circul. Physiol. **287**, H450–457 (2004).

[3] V. Mor-Avi, E. G. Caiani, K. A. Collins, C. E. Korcarz, J. E. Bednarz, and R. M. Lang, "Combined assessment of myocardial perfusion and regional left ventricular function by analysis of contrast-enhanced power modulation images", Circulation **104**, 352–357 (2001).

[4] D. Hope Simpson, C. T. Chin, and P. N. Burns, "Pulse inversion doppler: a new method for detecting nonlinear echoes from microbubble contrast agents", IEEE Trans. Ultrason. Ferroelec. Freq. Contr. **46**, 372–382 (1999).

[5] P. J. A. Frinking, A. Bouakaz, J. Kirkhorn, F. J. Ten Cate, and N. de Jong, "Ultrasound contrast imaging: current and new potential methods", Ultrasound Med. Biol. **26**, 965–975 (2000).

[6] P. Rafter, P. Phillips, and M. A. Vannan, "Imaging technologies and techniques", Cardiology Clinics **22**, 181–197 (2004).

[7] P. M. Shankar, P. D. Krishna, and V. L. Newhouse, "Advantages of subharmonic over second harmonic backscatter for contrast-to-tissue echo enhancement", Ultrasound Med. Biol. **24**, 395–399 (1998).

[8] D. E. Goertz, M. E. Frijlink, N. de Jong, and A. F. W. van der Steen, "High frequency nonlinear scattering from a micrometer to submicrometer sized lipid encapsulated contrast agent", Ultrasound Med. Biol. **32**, 569–577 (2006).

[9] D. E. Goertz, M. E. Frijlink, D. Tempel, V. Bhagwandas, A. Gisolf, R. Krams, N. de Jong, and A. F. W. van der Steen, "Subharmonic contrast intravascular ultrasound for vasa vasorum imaging", Ultrasound Med. Biol. **33**, 1859–1872 (2007).

[10] R. Esche, "Untersuchung der schwingungskavitation in flussigkeiten", Acustica **2**, 208 – 218 (1952).

[11] E. A. Neppiras, "Subharmonic and other low-frequency emission from bubbles in sound-irradiated liquids", J. Acoust. Soc. Am. **46**, 587–601 (1969).

[12] P. de Santis, D. Sette, and F. Wanderlingh, “Cavitation detection: The use of the subharmonics”, J. Acoust. Soc. Am. **42**, 514–516 (1967).

[13] A. Eller and H. G. Flynn, “Generation of subharmonics of order one-half by bubbles in a sound field”, J. Acoust. Soc. Am. **46**, 722–727 (1969).

[14] A. I. Eller, “Subharmonic response of bubbles to underwater sound”, J. Acoust. Soc. Am. **55**, 871–873 (1974).

[15] A. Prosperetti, “Nonlinear oscillations of gas bubbles in liquids: steady-state solutions”, J. Acoust. Soc. Am. **56**, 878–885 (1974).

[16] A. Prosperetti, “Nonlinear oscillations of gas bubbles in liquids. Transient solutions and the connection between subharmonic signal and cavitation”, J. Acoust. Soc. Am. **57**, 810–821 (1975).

[17] W. Lauterborn, “Numerical investigation of nonlinear oscillations of gas bubbles in liquids”, J. Acoust. Soc. Am. **59**, 283–293 (1976).

[18] A. Prosperetti, “Application of the subharmonic threshold to the measurement of the damping of oscillating gas bubbles”, J. Acoust. Soc. Am. **61**, 11–16 (1977).

[19] N. de Jong and L. Hoff, “Ultrasound scattering properties of albunex microspheres”, Ultrasonics **31** (1993).

[20] K. Sarkar, W. T. Shi, D. Chatterjee, and F. Forsberg, “Characterization of ultrasound contrast microbubbles using in vitro experiments and viscous and viscoelastic interface models for encapsulation”, J. Acoust. Soc. Am. **118**, 539–550 (2005).

[21] S. van der Meer, B. Dollet, M. Voormolen, C. T. Chin, A. Bouakaz, N. de Jong, M. Versluis, and D. Lohse, “Microbubble spectroscopy of ultrasound contrast agents”, J. Acoust. Soc. Am. **121**, 648–656 (2007).

[22] P. M. Shankar, P. D. Krishna, and V. L. Newhouse, “Subharmonic backscattering from ultrasound contrast agents”, J. Acoust. Soc. Am. **106**, 2104–2110 (1999).

[23] C. C. Church, “The effect of an elastic solid surface layer on the radial pulsations of gas bubbles”, J. Acoust. Soc. Am. **97**, 1510 – 1521 (1995).

[24] L. Hoff, P. C. Sontum, and J. M. Hovem, “Oscillations of polymeric microbubbles: effect of the encapsulating shell”, J. Acoust. Soc. Am. **107**, 2272–2280 (2000).

[25] O. Lotsberg, J. M. Hovem, and B. Aksum, “Experimental observation of subharmonic oscillations in infoson bubbles”, J. Acoust. Soc. Am. **99**, 1366–1369 (1996).

[26] P. D. Krishna, P. M. Shankar, and V. L. Newhouse, “Subharmonic generation from ultrasonic contrast agents”, Phys. Med. Biol. **44**, 681–694 (1999).

[27] P. H. Chang, K. K. Shung, S. Wu, and H. B. Levene, “Second harmonic imaging and harmonic doppler measurements with albunex”, IEEE Trans. Ultrason. Ferroelec. Freq. Contr. **42**, 1020–1027 (1995).

[28] E. Biagi, L. Breschi, E. Vannacci, and L. A. Masotti, “Stable and transient subharmonic emissions from isolated contrast agent microbubbles”, IEEE Trans. Ultrason. Ferroelec. Freq. Contr. **54**, 480–497 (2007).

[29] P. J. A. Frinking and N. de Jong, “Subharmonic imaging”, in *Fourth Annual Ultrasound Contrast Research Symposium in Radiology* (San Diego, USA) (1999).

[30] P. J. A. Frinking, E. Gaud, J. Brochot, and M. Arditi, “Subharmonic scattering of phospholipid-shell microbubbles at low acoustic pressure amplitudes”, submitted to IEEE Trans. Ultrason. Ferroelec. Freq. Contr. (2009).

[31] G. Bhagavatheeshwaran, W. T. Shi, F. Forsberg, and P. M. Shankar, “Subharmonic signal generation from contrast agents in simulated neovessels”, Ultrasound Med. Biol. **30**, 199–203 (2004).

[32] E. Kimmel, B. Krasovitski, A. Hoogi, D. Razansky, and D. Adam, “Subharmonic response of encapsulated microbubbles: Conditions for existence and amplification”, Ultrasound Med. Biol. **33**, 1767–1776 (2007).

[33] C. T. Chin, C. Lancee, J. Borsboom, F. Mastik, M. E. Frijlink, N. de Jong, M. Versluis, and D. Lohse, “Brandaris 128: A digital 25 million frames per second camera with 128 highly sensitive frames”, Rev. Sci. Instr. **74**, 5026–5034 (2003).

[34] M. Overvelde, V. Garbin, J. Sijl, B. Dollet, N. de Jong, D. Lohse, and M. Versluis, “The non-linear behaviour of phospholipid coated microbubbles at low acoustic pressure is dominated by buckling of the shell”, in preperation .

[35] V. Garbin, D. Cojoc, E. Ferrari, E. Di Fabrizio, M. L. J. Overvelde, S. M. van der Meer, N. de Jong, D. Lohse, and M. Versluis, “Changes in microbubble dynamics near a boundary revealed by combined optical micromanipulation and high-speed imaging”, Appl. Phys. Lett. **90**, 114103–3 (2007).

[36] B. Dollet, S. van der Meer, V. Garbin, N. de Jong, D. Lohse, and M. Versluis, “Nonspherical oscillations of ultrasound contrast agent microbubbles”, Ultrasound Med. Biol. **34**, 1465–1473 (2008).

[37] R. Veldhuizen, K. Nag, S. Orgeig, and F. Possmayer, “The role of lipids in pulmonary surfactant”, Biochim. Biophys. Acta Mol. Basis Dis. **1408**, 90–108 (1998).

[38] G. Enhorning, “Pulsating bubble technique for evaluating pulmonary surfactant”, J. Appl. Physiol. **43**, 198–203 (1977).

[39] X. Wen and E. I. Franses, “Adsorption of bovine serum albumin at the air/water interface and its effect on the formation of dppc surface film”, Colloid. Surface. A **190**, 319–332 (2001).

[40] C. C. Cheng and C. H. Chang, “Retardation effect of tyloxapol on inactivation of dipalmitoyl phosphatidylcholine surface activity by albumin”, Langmuir **16**, 437–441 (2000).

5

Simultaneous optical and acoustical recording of the dynamics of a single ultrasound contrast microbubble[‡]

A full understanding of the contrast enhancing abilities of microbubbles in ultrasound imaging [1], targeted drug delivery with microbubbles, and enhanced drug uptake by using ultrasonically driven microbubbles [2, 3] starts with studying both the optical and the acoustical response of a single microbubble subjected to ultrasound. In this chapter, single isolated ultrasonically-driven microbubbles are imaged with an ultra-high speed camera (recording up to $25 \cdot 10^6$ *frames per second) [4]. The sound emission is recorded simultaneously with a calibrated single element transducer. We show that the sound emission can be predicted from the optically-recorded radial dynamics, and vice versa, that the radial dynamics can be determined from the remotely recorded acoustic response.*

[‡] to be submitted as: Jeroen Sijl, Hendrik J. Vos, Timo Rozendal, Nico de Jong, Detlef Lohse and Michel Versluis, "Simultaneous optical and acoustical recording of the dynamics of a single ultrasound contrast microbubble", Journal of the Acoustical Society of America (2009).

5.1 Introduction

Microbubbles are used as contrast agents for medical ultrasound imaging. With a mean bubble radius between 1 and 5 μm the bubbles are resonant scatterers at typical medical ultrasound frequencies of 1 to 6 MHz. The bubbles scatter ultrasound more efficiently than a solid particle of the same size, at up to nine orders of magnitude, owing primarily to the compressibility of their gas. In addition, microbubbles scatter ultrasound non-linearly at harmonic frequencies of the driving frequency. The non-linear acoustic response of the bubbles allows for a discrimination from the linear tissue echo, thereby improving the contrast-to-tissue ratio and forming the basis for the development of harmonic imaging methods in ultrasound [5], including power modulation imaging [6], and pulse inversion imaging [7].

A driving pressure pulse forces microbubbles into a pulsation which in turn converts into an acoustic response in the far field, the echo. The final acoustic response thus depends strongly on the (non)linear dynamics of the microbubbles. Small radial excursion leads to a radial response that depends linearly on the driving pressure, but larger excursion leads to a non-linear relation [8]. Common equations to describe the radial dynamics are based on the Rayleigh-Plesset equation, which is an ordinary non-linear differential equation. In linearized form, i.e., for small radial excursions, it takes the analytical form of a harmonic oscillator [9].

Microbubbles have a limited lifetime as a result of the capillary pressure $2\sigma/R$ which gives rise to a partial pressure differences inside and outside the microbubble. The capillary pressure which is of the order of the atmospheric pressure thus reduces the time of dissolution of the bubble to several milliseconds. In order to stabilize clinical microbubbles the interface is coated with a protein, lipid, or polymer layer, as to reduce surface tension. The coating prevents gas diffusion, gas exchange to the surrounding liquid is reduced in addition by the choice of a low-solubility gas, such as perfluorocarbon or sulfurhexafluoride.

However the coating has a pronounced effect on the bubble dynamics. The dilatational viscous properties of the shell material result in an overall damping of the oscillation, while the elasticity of the shell material results in an increase of the resonance frequency [8]. But above all the viscoelastic properties can be non-linear which adds to the intrinsic non-linear features of the bubble dynamics. The Rayleigh-Plesset equation can be modified to model the contributions of the shell. The viscoelastic properties are then captured in a set of shell parameters, which values can be determined experimentally. A possible experimental approach would be to optically record the radial dynamics of a microbubble subjected to ultrasound, from which the shell parameters are extracted by comparing the experimental curves with those of the theoretical predictions [9].

The acoustic emission of the bubble directly follows from the radial dynamics. The conversion from energy of the flow around the pulsating bubble into acoustic energy depends on the geometrical size of the bubble, the velocity and the acceleration of the bubble wall. For larger radial excursions this conversion can enhance the non-linear higher harmonic contributions to the acoustic response. The total non-linear acoustic response of the bubble therefore originates from a combination of the intrinsic non-linear contributions of the bubble dynamics, coupled to those of the non-linear shell properties and the transformation of the radial dynamics into acoustic energy in the far field. Since the efficacy of many contrast detection schemes depends on non-linear signals, it is worthwhile to investigate the significance of each contribution. The influence of non-linear shell properties has been extensively studied theoretically and experimentally by e.g. [10–15]. The conversion from radial excursion to the scattered sound wave has had far less attention. Although a theoretical derivation exists based on the equation of motion and energy-conservation laws [16, 17], microbubbles may not comply to the assumptions made in the derivation. Studying the significance of the conversion therefore needs recordings of both the radial response $R(t)$ and the resulting acoustic response $P(t)$ of a microbubble. The Rayleigh-Plesset equation for example assumes the bubble to be isolated in an infinite medium and the bubble to remain spherical at all times. From in-vitro, ex-vivo and in-vivo studies it is know that bubbles are located in confined geometries which lead to interactions with adjacent walls [18–21]. Neighboring bubbles are acoustically coupled. For molecular imaging applications microbubbles are targeted to diseased cells through ligands introducing complex biomolecular interactions. Many of these interactions lead to non-spherical bubble oscillations and *a priori* it is not known how these translate into the acoustic response. Vice versa it would be important to know if and how the radial dynamics could be inferred from the measured acoustic response. This reverse calculation is nontrivial and to our knowledge has never been done in the context of ultrasound contrast agents.[*] Here we present a detailed experimental investigation of the

---

[*] Note that we have recently deduced both the size and the radial dynamics of an entrained bubble in an inkjet channel from the modification of the acoustic response of the channel[22]

different non-linear contributions to the overall acoustic response of coated microbubbles. We employ the Brandaris ultrahigh-speed camera to resolve the radial dynamics of a single microbubble and combine the results with a sensitive and calibrated acoustic setup to quantitatively assess its acoustic response. Through this combined setup we can monitor both the bubble dynamics and the emitted sound and we can verify to what degree these two types of signals correspond to eachother. The data are also used to investigate if it is possible to predict the radial dynamics of the bubble explicitly from its acoustic signature and resting radius.

5.2 Bubble dynamics and Sound emission

The acoustic response of a coated microbubble to a driving pressure pulse is determined in two steps. Both steps are schematically shown in Fig. 5.1. The first step determines the bubble dynamics as a response to the driving pressure pulse. In the case of volumetric oscillations, the dynamics of the bubble is completely described by the radius time curve, $R(t)$. The radius-time curve can be recorded optically with ultra-high speed imaging [4]. For an uncoated bubble the relation between the driving pressure and the dynamics is well described by the Rayleigh-Plesset equation (see below). According to the Rayleigh-Plesset equation the dynamics of a bubble is determined by the initial radius of the bubble, R_0, the driving pressure amplitude and its frequency. The Rayleigh-Plesset equation is non-linear, and it can introduce higher harmonics into the dynamic response of a microbubble. As discussed in the previous chapters the shell of an ultrasound contrast agent microbubble introduces even more non-linearities into the dynamic response. According to the model of Marmottant *et al.* [10] these additional non-linearities can be accounted for by three shell parameters: the shell viscosity, the shell elasticity, and the initial surface tension of the microbubble $\sigma(R_0)$. The most direct method to characterize the shell of the microbubble is therefore to record its radius-time curve as a response to different driving pressures. The second step, which is of main importance for contrast-enhanced ultrasound imaging, describes how the radial dynamics of the bubble converts into an acoustic response at a certain distance, r from the bubble. Conservation of mass and momentum in the liquid completely determine this step. Moreover, this step changes the non-linear content of the final acoustic bubble response as will be shown below. Both steps are detailed in the following subsections.

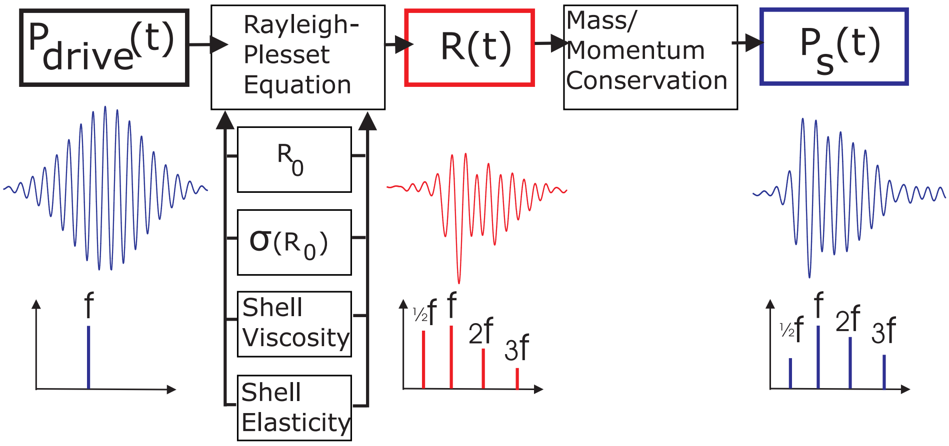

Figure 5.1: A schematic view on the origin of the non-linear acoustic response of an ultrasound contrast agent microbubble to a single frequency driving pressure pulse.

5.2.1 Bubble dynamics

If a bubble experiences a time-varying pressure field (such as an incoming ultrasound wave) it will react with compression or expansion. The kinetic energy supplied to the surrounding liquid should balance the difference between the work performed by the fluid far from the bubble and that at the bubble wall. If we assume the bubble to remain spherical and the liquid to be incompressible the Rayleigh-Plesset equation is obtained [16, 23]:

$$\underbrace{\rho\left(R\ddot{R}+\frac{3\dot{R}^2}{2}\right)}_{\textit{kinetic energy}} = \underbrace{(p_L - p_\infty)}_{\textit{pressure difference}} \tag{5.1}$$

In this equation R, $\dot{R}$, and $\ddot{R}$ describe the radius, the velocity and the acceleration of the bubble wall, respectively. The density of the water is described by $\rho = 10^3$ kg/m^3 and the pressure difference is determined by the pressure in the water at the bubble wall, p_L , and the pressure far from the bubble wall, p_∞. This equation can be worked out and extended in various ways, for example to include the effect of a coating on the bubble dynamics. A popular version of the equation that accounts for the many non-linear characteristics of a phospholipid shell microbubble is provided by Marmottant *et al.* [10]:

$$\begin{aligned} &\rho\left(R\ddot{R}+\frac{3}{2}\dot{R}^2\right) \\ &= \overbrace{\left(P_0+\frac{2\sigma(R_0)}{R_0}\right)\left(\frac{R_0}{R}\right)^{3\gamma}\left(1-\frac{3\gamma\dot{R}}{c}\right)-\frac{2\sigma(R)}{R}}^{p_L} \\ &-4\mu\frac{\dot{R}}{R}-4\kappa_s\frac{\dot{R}}{R^2}\underbrace{-P_0-P_A(t)}_{p_\infty}, \end{aligned} \tag{5.2}$$

In this equation $c = 1500$ m/s denotes the speed of sound in the water. The initial bubble radius is given by R_0 and the ambient pressure by P_0. The driving pressure pulse is described by $P_A(t)$. The relation between the internal gas pressure (P_g), the gas temperature and bubble volume is described by the polytropic ideal gas law, $P_g \propto R^{-3\gamma}$ where γ is the polytropic exponent. For isothermal oscillations $\gamma = 1$ and for adiabatic oscillations γ is equal to the ratio of the specific heats of the gas inside the bubble, C_p/C_v, with C_p the specific heat at constant pressure and C_v the one at constant volume. In the experiments discussed in this chapter we may approximate the oscillations as adiabatic [9, 10]. For the used experimental agent BR-14 (Bracco Research S.A., Geneva, Switzerland) the gas core consists of perfluorocarbon-gas with $\gamma = C_p/C_v = 1.07$ [9, 10]. The main damping of the bubble oscillations results from the liquid viscosity $\mu = 1 \cdot 10^{-3}$ Pa s and the damping introduced by the phospholipid shell described by $\kappa_s = 3 \cdot 10^{-8}$ kg/s [9]. In the model proposed by Marmottant *et al.* [10] the surface tension of the bubble is assumed to depend on the bubble radius, $\sigma(R)$. For full details on the relation between the effective surface tension and the bubble radius we refer to the previous two chapters. In those chapters it was shown that $\sigma(R)$ is completely determined by the shell elasticity $\chi(R)$ and the initial surface tension $\sigma(R_0)$. For given initial conditions the ordinary differential equation Eq. 5.2 can be solved using a numerical solver to give the radial bubble response.

The theoretical influence of the non-linear strain-stress relation of the shell is extensively studied elsewhere in this dissertation and is therefore not further addressed in the current Chapter.

5.2.2 Sound emission

The sound emitted by an oscillating microbubble consists of two parts. The first is a passive contribution that results from the geometrical scattering of the microbubble (could be a non-oscillating body) in the incident ultrasound field and the second is an active contribution that results from the volumetric oscillations of the bubble. In regular applications, ultrasound contrast microbubbles are much smaller than the incident wavelength and the passive contribution can be safely neglected, as shown previously by Hilgenfeldt *et al.* [17]. The active contribution is determined by the radial dynamics of the microbubble only and is described by the radius-time curve $R(t)$. From the conservation of mass and momentum it follows that the emitted pressure wave $P_s(r,t)$, at a distance r, equals the second time derivative of the volume V of the bubble,

$$P_s(r,t-r/c) = \frac{1}{4\pi}\frac{\rho}{r}\ddot{V}(t) = \frac{1}{3}\frac{\rho}{r}\frac{\partial^2}{\partial t^2}[R(t)^3] \tag{5.3}$$

where ρ is the density of the surrounding liquid. The finite time for the pressure wave to travel a distance r from the bubble wall to the transducer surface is accounted for by the term r/c where c again is the speed of sound in the liquid medium.

A regularly used form of Eq. 5.3 is obtained by rewriting:

$$P_s(r,t-r/c) = \frac{\rho}{r}\left(R(t)^2\ddot{R}(t) + 2R(t)\dot{R}(t)^2\right), \tag{5.4}$$

In these equations it is assumed that the receiver is sufficiently far from the microbubble to neglect the Bernoulli pressure (also referred to as the kinetic wave), which decreases with $(1/r^4)$ [16, 24]. Furthermore, Eq. 5.3 accounts only for volumetric oscillations of the bubble; we will validate later that surface modes do not contribute significantly to the sound emission. Translation of the bubble as a result of the acoustic driving also results in additional sound scattering [17, 25]. However, this contribution is of the same order as that of the passive contribution and can therefore be safely neglected. Finally, both equations assume an isolated single bubble; the sound emitted from neighboring pulsating bubbles is not taken into account.

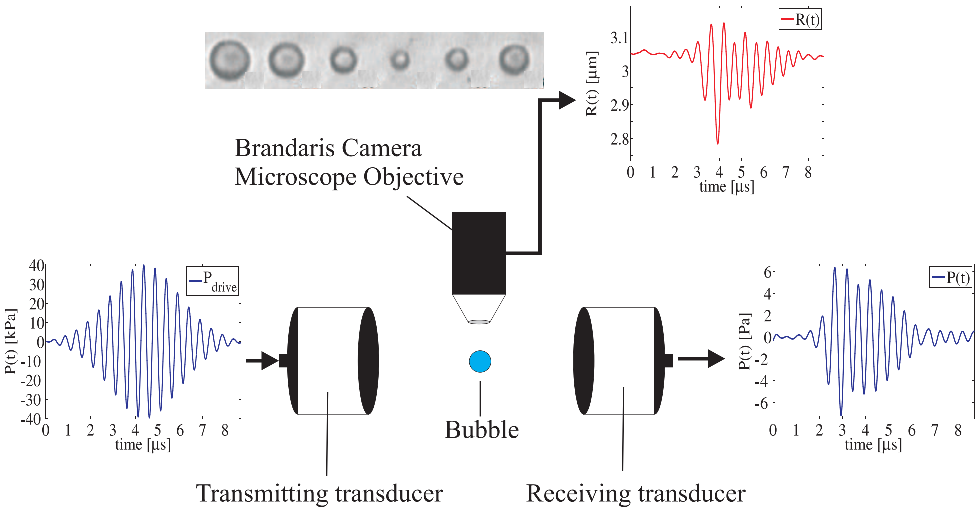

Figure 5.2: A schematic view of the setup which is used to simultaneously record both the radial dynamics and the acoustic response of an isolated ultrasound contrast microbubble. The Gaussian-apodized driving pressure waveform which is produced by an arbitrary waveform generator was amplified and transmitted by a focussed transducer. The echo response of the bubble was received by a second focused calibrated transducer. Simultaneously the radial dynamics of the microbubble was recorded through a 100X microscope objective connected to the Brandaris-128 ultra high speed camera. From the recorded movies, radius time curves are extracted and the relation between the radial dynamics of the bubble and its acoustic response are examined.

5.3 Experimental Setup

To investigate the theoretically derived relations between the radial dynamics of the microbubble and its scattered sound we combine the Brandaris-128 ultra high speed camera with an acoustical setup capable of quantitatively recording the sound transmitted by a single oscillating microbubble, see Ch. 2. The contrast agent studied was BR-14, a contrast agent containing microbubbles with a phospholipid shell and a perfluorocarbon-gas core.

The combined setup is schematically shown in Fig. 5.2. It consists of a cylindrical Plexiglass container which was mounted below an upright microscope (BXFM, Olympus Optical, Japan). Within the container the microbubbles were confined in a 200 µm diameter cellulose capillary tube with an 8-µm wall thickness (Product no. 132294, Spectrum Europe, Breda, The Netherlands). The capillary tube was mounted horizontally in the center of the container.

5.3.1 Single bubbles

It is not straightforward to ensure that the acoustic response received by the transducers results from a single microbubble. It requires the isolation of the microbubble with an initial bubble radius of around 2 µm in a volume as large as 2 mm^3 (comparable to the wavelength of the ultrasound). We have achieved this through the help of a reservoir in which we injected a solution containing a population of microbubbles as is schematically shown in Fig. 5.3. On one side the reservoir was connected to a 200 µm diameter cellulose capillary tube that led to the measurement section. This capillary tube entered the bubble reservoir 400 µm below the top surface of the reservoir. This prevented bubbles that are touching the top surface from flowing into the tube. The other side of the bubble reservoir was open to the atmospheric pressure. Capillary forces prevented the solution from flowing out. With a micropipette connected to a syringe we entered the bubble reservoir from the open side. With a 3D-translation stage connected to the pipette, we could move the pipette around inside the reservoir and select a bubble. The micropipette had a tip size of 0.5 µm which is smaller than the typical bubble size. By applying a negative pressure to the pipette we grabbed a single bubble, brought it down, and released it inside the capillary tube [26]. With a syringe pump connected to the other side of the capillary tube we moved the bubble through the capillary tube into the measurement section. Note that the bubble remains in the capillary tube during the experiments.

The radial dynamics of the bubble were recorded with the Brandaris 128 ultra-high speed camera [4] coupled to the microscope having a 100X microscope objective (LUMFPL, Olympus Optical, Japan) which was focused onto the capillary tube. The focal distance of the objective was 1.1 mm. In our measurements we recorded series of 6 movies of 128 frames each at a frame rate near 13 million frames per second (Mfps). The time interval between recordings was 2.5 s. The microbubble was illuminated from below with a high intensity xenon flashlight (MVS 7010 XE, Perkin Elmer, Waltham, MA). A continuous light source (ACE I, Schott, NY) in combination with a single CCD camera (LCL-902K, Qwonn) was used to monitor the bubble in between experiments.

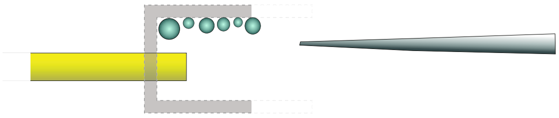

(a) Initial situation

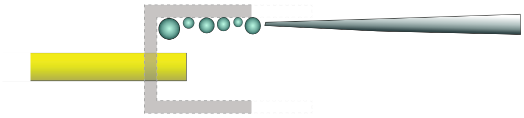

(b) Select a bubble with the micropipet

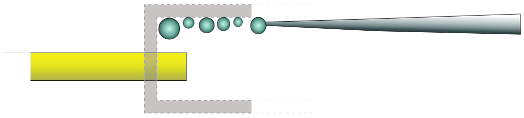

(c) Grab the bubble with the micropipet by applying a negative pressure

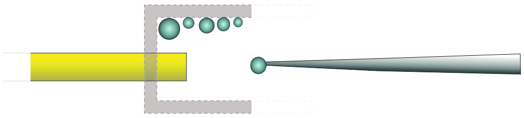

(d) Move the bubble down

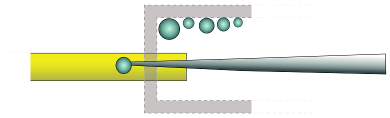

(e) Move the bubble inside the capillary fiber

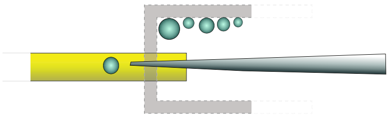

(f) Release the bubble

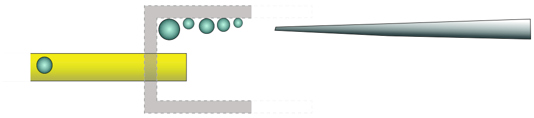

(e) Move micropipet back

Figure 5.3: Schematic view on the single bubble selection

To simultaneously record the sound emitted by the oscillating microbubble, the microscope was confocally aligned with two focused transducers. One of the transducers, a 3-MHz center frequency transducer (PA168, Precision Acoustics Ltd., Dorset, UK) was used to excite the bubble with an ultrasound pulse. The second calibrated transducer (3.5-MHz, 100 % -6 dB relative bandwidth, Panametrics C381-1 inch foucs, Olympus NDT, Waltham, MA) received the acoustic bubble response [11]. The transducers were aligned in the same plane of the capillary tube under an angle of 50° to the capillary tube and at a 100° angle to each other in order to minimize specular reflection of the driving ultrasound on the capillary. Two calibrated 0.2 mm needle hydrophones (Precision Acoustic Ltd., Dorset, UK) were mounted in the Plexiglas container exactly opposite to the two transducers. The hydrophones could be moved in and out of the focus of the two transducers and were used to confocally align the two transducers with the microscope objective. The transmit transducer was excited with pulses generated by an arbitrary waveform generator (Tabor Electronics Ltd, Model 8026, Haifa, Israel) and amplified by a linear power amplifier (ENI, Model 350L with 50 Ω input impedance, Rochester, NY). The received bubble echoes were amplified 59.3 dB by a low-noise amplifier (Miteq, Model AU-1519-10289, Hauppauge, NY) and digitized by a digital oscilloscope (Tektronix, TDS 3012, Beaverton, OR). The digitized data are stored on a PC through a GPIB-link for off-line analysis.

5.3.2 Data generation and processing

Gaussian-apodized driving pressure pulses with frequencies ranging from 1 to 4 MHz were used to drive the bubbles. All pulses had a peak negative pressure amplitude of 40 kPa and had a length of 8.9 μs. The optical frames are analyzed to obtain the $R(t)$ curves through a semi-automatic minimum cost algorithm [9] in MATLAB (The Mathworks, Natick, MA). The acoustically-received voltage vs time curves on the oscilloscope were converted into pressure-time curves using the receive transfer function of the transducer following the procedure described in [11]. The setup, including the capillary tube, produces a steady acoustic background signal. For each experiment this background signal was also recorded in the absence of a microbubble and subtracted from the signal recorded in the presence of a microbubble.

Fig. 5.4 shows a typical recording of the responses of an isolated bubble of 3.7 μm radius to pulses with an increasing frequency of 1.7 to 2.7 MHz (A).

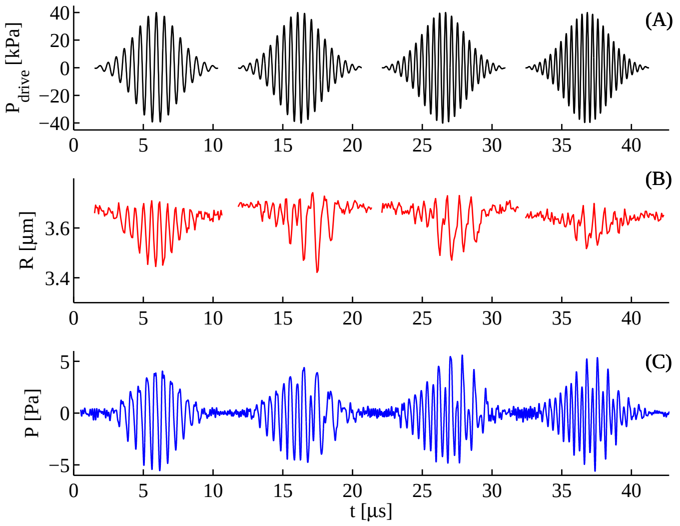

Figure 5.4: A typical example of the simultaneously recorded radial dynamics and the resulting acoustic responses of an isolated 3.7 µm bubble. (Top) four different driving pressures with varying frequency for 1.7 MHz, 2 MHz, 2.3 MHz and 2.6 MHz, (middle) the resulting radial dynamics as recorded with the Brandaris 128 ultra-high speed camera, (bottom) the simultaneously recorded acoustic responses.

The optically-recorded radial response is shown in (B). At the lowest driving frequency (left hand trace) the bubble follows the driving pressure pulse, although the period-averaged radius shows a decrease during the oscillation, resulting in “compression-only” behavior [27]. At higher driving frequencies the “compression-only” behavior is still visible, but also a strong subharmonic component develops after few cycles of the driving pulse. The amplitude of the radial excursion decreases with increasing frequency, which is expected for bubbles that are driven with frequencies increasingly higher than their resonance frequency. The simultaneously recorded acoustic response (C) shows similar envelopes as the driving pulse, and also shows the subharmonic component, although at lesser extent than in the optical data; this effect will be extensively addressed later.

5.4 Results

A total of 16 different microbubbles were studied at different pressures and frequencies resulting in a set of 194 recordings. Depending on the initial bubble radius and the driving frequency a selection of bubbles were observed to oscillate linearly, while the other bubbles oscillated non-linearly, i.e. a non-linear harmonic or subharmonic component could be identified in the radius-time curve. In section 5.4.1 we will first focus on the linear bubble dynamics at the fundamental frequency. The non-linear dynamics will be discussed in section 5.4.2 .

5.4.1 Linear response

A typical example of the recorded oscillations of a 6.5 μm bubble subject to a 1 MHz, 40 kPa driving pulse is shown in Fig. 5.5(a). The camera was recording at a framing rate of 12.5 Mfps. From the absence of harmonics in the spectra of the $R(t)$ curve, shown in Fig. 5.5(b), we conclude that the oscillations are linear. As a result of the oscillations of the bubble wall, a spherical acoustic wave travels outward from the bubble. With Eq. 5.3 and the experimentally determined $R(t)$ curve we have calculated the resulting $P_s(r,t)$. The distance r in Eq. 5.3 is taken equal to 2.54 cm since this is the focal distance of the receiving transducer. The predicted $P_s(r,t)$ is band-pass filtered around the transmission frequency and shown together with the actually measured pressure time curve in Fig. 5.5(c). The agreement between the two curves is very good. Interestingly, both the acoustical setup and the optical setup in combination with Eq. 5.3 are able to pick up and correctly predict pressure variations of the order of 1 Pa on an ambient pressure of 10^5 Pa.
As will be discussed in the next section, the higher frequency content in the $R(t)$ curve are enhanced in the calculated $P(t)$ curve. The typical noise content on the $R(t)$ curve determined from the high-speed movie is around -35 dB lower than the fundamental response, as clearly visible in Fig. 5.5(b). Because of the frequency-dependent enhancement the high-frequency noise level can become as high as the bubble response signal, as observed in Fig. 5.5(c). In order to compare the results in time domain it is therefore necessary to filter the $P(t)$ curve that was predicted from the raw data. The used filter was a low-pass fourth order Butterworth filter with a cut-off frequency of 2 MHz. In Fig. 5.5(d) both the unfiltered and the filtered power spectrum of the calculated $P(t)$ curve are shown.

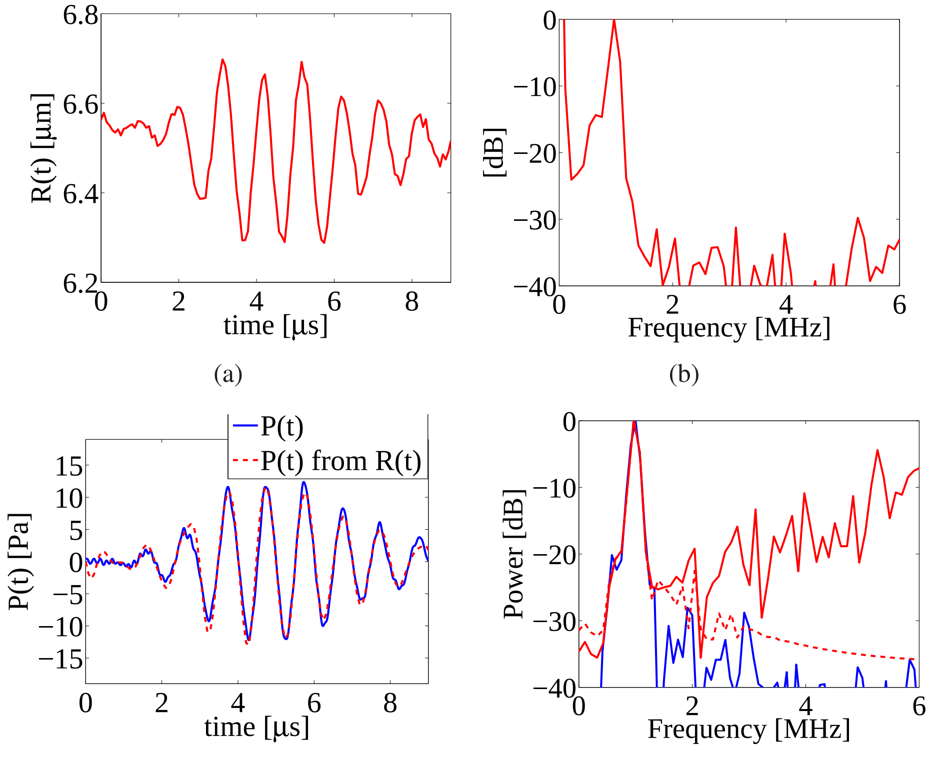

(a) (b)

(c) (d)

Figure 5.5: Acoustic emission as a function of time determined from the bubble radius as function of time. (a) Example of the radial bubble dynamics for a bubble with an initial bubble radius of 6.5 μm*, recorded with the Brandaris ultrahigh-speed camera. The dynamics shown here are the response to a driving pressure waveform with a peak rarefractional amplitude of 40 kPa and a frequency of 1 MHz. (b) The spectrum of the* $R(t)$ *curve showing no higher harmonics. In (c) we compare the acoustic response calculated from the measured* $R(t)$ *curve with Eq. 5.4 (dashed red line) and the actually measured acoustic response (solid blue line) measured by the receive transducer. In (d) the power spectra of the measured* $P(t)$ *curve in blue and the filtered (solid red line) and unfiltered (dashed red line) predicted* $R(t)$ *curve.*

The data processing shown above for a single bubble was repeated for all recordings. From the recorded and predicted $P(t)$ curves the maximum amplitude of the acoustic response was determined. The amplitudes for all data are shown in the scatter plot in Fig. 5.6. Though not for all data the agreement is as good as presented in Fig. 5.5(c) it is satisfactory. The middle line in this figure denotes the expectation of equal pressure amplitudes from the recorded and the derived pressure traces. The upper and lower (red) lines in Fig. 5.6 represent a difference of 3 dB between the two data sets. For 70% of the experiments the fundamental response predicted from the $R(t)$ curve is within 3 dB of the measured fundamental response. For 90% of the experiments the difference is within 6 dB. We observe that the measured fundamental acoustic response is typically 1 dB lower than the acoustic response predicted from the $R(t)$ curve. Several possible causes can be identified. First possible cause is the acoustic attenuation in the cellulose capillary tube. Second is an error in determination of the bubble radius, R. Preliminary studies have shown that a small difference in optical focusing could result in a systematic measurement error in the radius of 15 %. Third is a possible error in the calibration value of the receiving transducer; the hydrophone used as a standard for the calibration has an calibration accuracy of 10 %, or 0.8 dB, as stated by the manufacturer.

5.4.2 Non-linear response

In order to understand the effect of Eq. 5.3 on the non-linear bubble response it is insightfull to linearize Eq. 5.3. For this purpose we assume the radial dynamics to be described by $R(t) = R_0(1+\epsilon \cdot \sin(\omega t))$ where $\epsilon << 1$ and ω the angular frequency of the oscillation. Inserting this into Eq. 5.3 and ignoring terms of second and higher order we obtain

$$P_s(r, t-r/c) = \frac{\rho\omega^2 R_0^3 \epsilon \cdot \sin(\omega t)}{r} \tag{5.5}$$

First of all, this relation shows that the scattered sound of the bubble increases cubically with the initial bubble radius. Therefore for a similar relative radial excursion ϵ, a larger bubble will scatter more sound than a smaller bubble. Similarly, the amplitude of the scattered sound of an oscillating bubble increases quadratically with the frequency of oscillation. As a result, the ratio of the second harmonic oscillations to that of the fundamental is enhanced by a factor of four for the acoustic response as compared to the radial response.

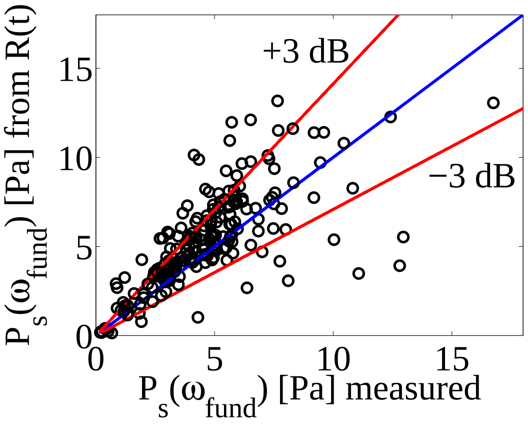

Figure 5.6: A comparison between the amplitude of the acoustic bubble response at the fundamental driving pressure frequency as measured by the receive transducer and the acoustic response as predicted from the measured $R(t)$ *curve for 194 different experiments for 16 different bubbles. The driving pressure amplitude of 40 kPa is fixed for all experiments while the driving pressure frequency was varied. The red lines represent the +3 dB and -3 dB bounds of the data set.*

This also explains the origin of the increase of the high frequency noise in the $P(t)$ curve calculated from the experimentally recorded $R(t)$ curve presented in Fig. 5.5.

In the example presented in Fig. 5.5 the bubble is oscillating linearly, and no signal is present at the higher frequencies. The latter implies that high frequency noise on the predicted $P(t)$ curve can be removed by a low-pass filter without signal loss. However, a non-linearly oscillating bubble will show higher harmonic oscillations and the use of a low-pass filter could result in signal loss.

An example of a non-linearly oscillating bubble is shown in Fig. 5.7(a). The bubble has an initial bubble radius of 4.9 μm and it was excited with a driving pulse with a frequency of 1.8 MHz. Since this driving frequency was close to twice its resonance frequency [9], the bubble responds non-linearly with subharmonic oscillations at 0.9 MHz. The radial subharmonic response is higher than the fundamental response at 1.8 MHz. The resulting acoustic response from these non-linear oscillations is calculated with Eq. 5.3. Fig. 5.7(b) shows the power spectrum of the resulting acoustic response which is compared to the power spectrum of the simultaneously measured acoustic response. For

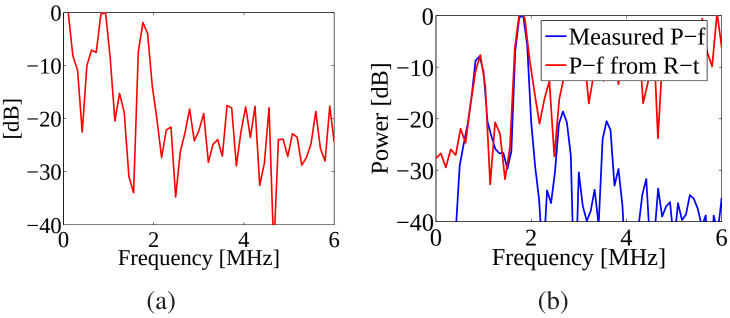

Figure 5.7: (a) Square of Fourier transform of the radius time curve of a bubble with an initial bubble radius of 4.9 μm. *A clear subharmonic response is visible at 0.9 MHz at half of the driving pressure frequency of 1.8 MHz (b) The square of the Fourier transform of the pressure time curve calculated from the* $R(t)$ *curve (red line) is compared to the square of the Fourier transform of the simultaneously measured acoustic response (solid blue line). A quantitative agreement is observed between the measured and calculated acoustic responses both for the fundamental and the subharmonic. Furthermore, it is observed that in the acoustic emission the higher frequencies are enhanced. The high frequency noise from the* $R(t)$ *curve is enhanced which is now shadowing the higher harmonic responses that can be observed in the measured acoustic response. For the same reason the relative amplitude of the subharmonic has decreased in the pressure response.*

the fundamental response and the subharmonic response the agreement is good. As explained by the ω^2-relation in Eq. 5.5 the subharmonic acoustic response has decreased significantly relative to the fundamental acoustic response. In the measured acoustic response we clearly observe higher harmonic contents at frequencies of 2.7 MHz and 3.6 MHz, which are not visible in the response predicted from the recorded radial dynamics. The noise in the radial response curve is visible at nearly 25 dB below the fundamental response, see Fig. 5.7(a), while the acoustic recording shows its superior resolving power of the higher harmonic responses with a noise level of -40 dB.

5.4.3 The inverse problem

In the previous two sections we have shown that it is possible to correctly predict the acoustic response of an oscillating microbubble based on its experimentally recorded $R(t)$ curve. It is clear that especially the fundamental and subharmonic *acoustic* response are correctly predicted from the optically recorded radial dynamics of a microbubble. However as a result of the noise on the measured $R(t)$ curve and the limited resolving power of the optical system, higher harmonics are difficult to study optically. The high frequency enhancement in the acoustical response and the sensitivity of an acoustical recording makes the recording of the acoustical response of a microbubble therefore complementary to an optical recording.

So we wonder wether it is possible to reconstruct the radial dynamics from the measured $P(t)$ curve. The radial dynamics can be recovered from a double integration of Eq. 5.3:

$$R^3(t) = R^3(0) + \dot{R}^3(0) + \frac{3r}{\rho}\int_0^t dt' \int_0^{t'} P_s(r,t')ds. \tag{5.6}$$

For a known initial bubble radius and a known initial bubble wall velocity (in general $\dot{R} = 0$) together with a known distance r between the receiving transducer and the microbubble the acoustic response can be integrated numerically to give the bubble radius $R(t)$ as a function of time.

In Fig. 5.8(a) the result from solving this inverse problem is shown for the acoustic response of the very same bubble as presented in Fig. 5.5. The bubble had a radius of 6.5 μm and it was subjected to a 1 MHz pulse. The acoustic response $P_s(r,t)$ was numerically integrated twice to give $R(t)^3$. The noise of the recorded acoustical response on average gives the $P(t)$ curve a small off-set. The double integration is extremely sensitive to low frequencies and a small offset results in a drift and an unphysical growth of the bubble size in the final $R(t)$ curve. We corrected for this drift by applying a second order Butterworth 0.2 MHz high-pass filter on $\dot{R}^3(t)$ after the first integration step. For sufficiently small time steps ($\Delta t < 5 \cdot 10^{-8}$s) the double integration was found to converge to the predicted $R(t)$ curve as shown in Fig. 5.8(b). The good agreement between the predicted and recorded radial dynamics is remarkable. Oscillations of the bubble wall smaller than 100 nm are correctly predicted from an acoustic response measured at a distance of 2.5 cm.

A small difference in the radial offset during the oscillation can be observed between the predicted and the measured $R(t)$ curves. As discussed before, “compression-only” behavior [10, 27], see also Ch. 3 gives an offset to the mean radius during the oscillation. The offset can be looked upon as a low-frequency component. Since the receive transducer is not sensitive to such low frequency component it is not detected; conversion from the recorded

`P(t)` into an `R(t)` will therefore not predict the low-frequency offset. To investigate the accuracy of the inverse method for all bubble recordings, the amplitudes of the optically-recorded radial responses were compared to those of the predicted ones, at the fundamental frequency. The agreement between the two was of similar quality as the one resulting from the agreement seen with the forward method (see Fig. 5.6) and therefore not plotted. In 60% of the experiments the fundamental response of the radial dynamics predicted from the `P(t)` curve is within 3 dB of the measured fundamental response. For 80% of the experiments the difference is within 6 dB. On average the acoustically-derived radial response had a slightly lower amplitude of oscillation than the optically-observed radial response.

In Fig. 5.9 the square of the Fourier transform of an optically recorded `R(t)` curve is presented together with the spectrum of the radial dynamics as predicted from the measured `P(t)` curve. Both curves are normalized to the same maximum response. We can identify a quantitative agreement between the two curves. Furthermore, Fig. 5.9 confirms the hypothesis that acoustic techniques can be used to study the higher harmonic radial dynamics of ultrasound contrast agent microbubbles, more sensitive than ultra-high speed imaging can. The higher harmonic oscillations of the bubble that are invisible in the optically recorded `R(t)` curve are clearly visible in the dynamics determined from the recorded acoustic response.

5.4.4 Subharmonic responses

In some of the conducted experiments, non-spherical shape oscillations were observed. Since these oscillations are predominately of a period-doubling nature [28] it can be hypothesized that these surface modes transmit subharmonic sound in the far field. If the surface modes would emit sound at the subharmonic frequency there should be a difference between the sound transmission calculated from the radius time curve, which is based only on the volumetric bubble oscillations through Eq. 5.3, and the scattered sound measured simultaneously with the transducer.

Of the set of 16 bubbles a total of 4 bubbles in 23 different experiments showed an acoustic subharmonic response, i.e. the acoustic subharmonic response was not more than 20 dB lower than the fundamental response. Examples of these subharmonic responses are shown in Figs.5.4 and 5.7(b). As in Fig. 5.7(b) the predicted and measured sound emission at the subharmonic frequency overlap within 2.5 dB for 20 of the 23 experiments, independent

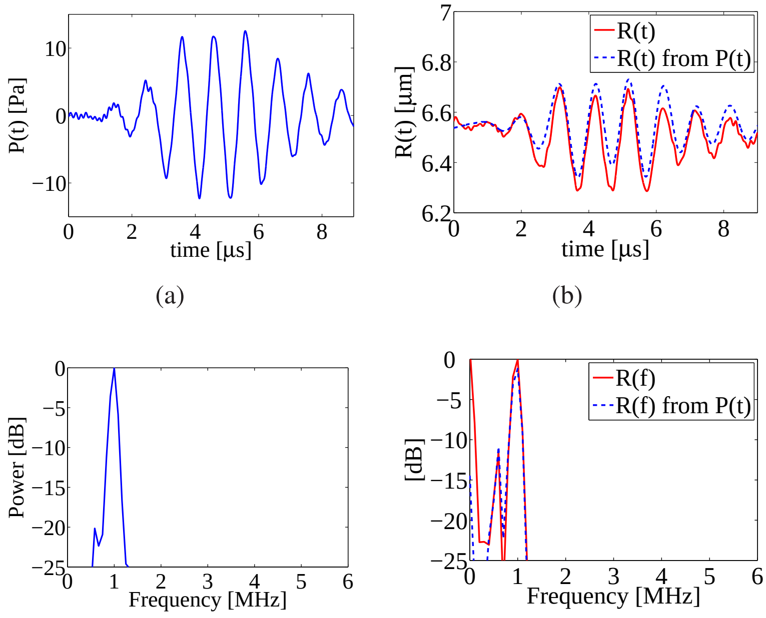

(a) (b)

(c) (d)

Figure 5.8: Bubble radius as a function of time determined from the acoustic emission as a function of time (a) The acoustic response of a 6.6 μm radius microbubble as measured with a focussed transducer at a distance of 2.54 cm from the bubble (same as in Fig. 5.5(a)). (b) From the measured acoustic response the dynamics of the bubble are predicted provided the initial bubble radius and the initial bubble wall velocity (zero) are known. We observe a good agreement between the measured and the predicted bubble dynamics. (c) The Fourier transform of the measured acoustic bubble response. (d) The Fourier transform of both the measured and the predicted bubble dynamics. We observe a good agreement between the two.

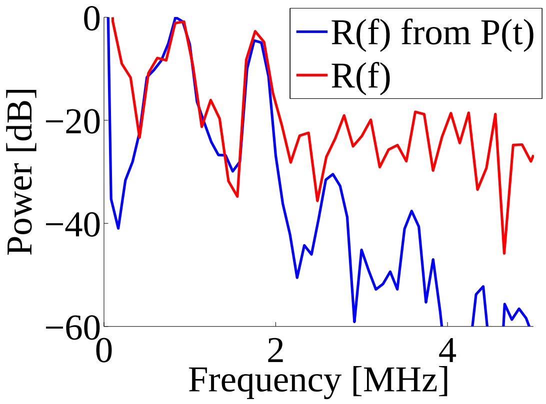

Figure 5.9: The square of the Fourier transform of the measured R(t) *curve of a bubble with an initial bubble radius of 4.9* μm *subjected to a 1.8 MHz, 40 kPa driving pressure pulse (same response as in Fig. 5.7(a)). Together with the square of the Fourier transform of the* R(t) *curve predicted from the simultaneously measured acoustic response. The higher harmonic oscillations of the bubble wall are clearly visible in the reconstructed dynamics.*

	Acoustic subharmonic	No acoustic subharmonic
Surface modes	15	54
No surface modes	8	192-15-54-8 = 115

Table 5.1: Overview of occurrence of subharmonic scattering and surface modes. Total number of recordings is 192.

of the occurrence of surface modes; see Table 5.1. Furthermore in 54 other experiments surface modes were observed in the absence of any volumetric subharmonic oscillation or subharmonic acoustic emission. The occurrence of surface modes was scored manually from the optical and acoustical data.

5.5 Discussion

5.5.1 Noise, sensitivity and bandwidth

The examples presented in Fig .5.7(b) and Fig. 5.9 show that the acoustic measurement is superior in terms of sensitivity, owing to the good noise characteristics of the transducer and amplifier. Strictly speaking, the high sensitivity is only present in a limited frequency band. Current optimized single-element transducers have a bandwidth of typically 1-6 MHz. Low frequency features of the radial dynamics such as "compression-only" behaviour might therefore not be captured by acoustical methods. In future experiments one could try to work around this by the addition of a dedicated low-frequency transducer. The Brandaris ultrahigh-speed camera has an effective bandwidth of 0-12.5 MHz when operated at its maximum frame rate of 25 Mfps and can therefore inherently capture the low-frequency contents.

If smaller bubbles are studied than presented here, the acoustic signals are expected to decrease on average. For equal radial excursion and frequency the acoustic amplitude depends cubically on the radius (Eq. 5.5). Hence, if smaller bubbles are studied the acoustic signal to noise ratio (SNR) will also decrease. On the other hand, it can be shown that the SNR in the optical movies also depend on the radius because of the finite pixel size in the frames (with the 100X objective the pixel size is $\sim 0.11\,\mu\text{m}$). Therefore, even for smaller bubbles the acoustic method is expected to be more sensitive than the optical method to study higher harmonic responses.

The sensitivity of the optically recorded radial response could be improved. One could try to increase the optical zoom to decrease the influence of the finite pixel size. Another improvement would be to reduce motion blur of the oscillating bubble wall by decreasing the exposure times within the design of the Brandaris camera. This requires either more sensitive ccd's or an increased intensity of the illumination. A third option would be to use laser-induced fluorescence techniques and high-intensity illumination to increase the contrast of the bubble wall with respect to the background illumination. Finally, improved data processing of the ultra-high speed movies into $R(t)$ curves may eventually lead to noise reduction. An improvement of 20 to 30 dB, if we take Fig. 5.9 as a reference, will then be the ultimate challenge.

5.5.2 Remote acoustic detection of in-vivo mechanical forcing

The inverse acoustical method provides a sensitive method to study the radial dynamics of ultrasound contrast agent microbubbles. An advantage of the method is that the recording can be performed remotely, at a distance of 10 cm or more from the bubble, while optical methods with a microscope inherently need an objective mounted close to the bubble, regularly at a distance

on the order of 1 mm. Such objective might produce unwanted acoustic reflections that interfere with the bubble signals.
The inverse method could potentially provide a new tool to *in-vivo* investigate the relation between local mechanical action and enhanced drug uptake by cells [2, 29, 30]. In literature it is suggested that strain caused by oscillating bubbles close to a cell membrane results in opening of the cell and enhanced drug uptake. Strain could be estimated from the oscillation amplitude of the bubble [2, 3, 30, 31]. Thus, in the future a remote acoustic detection method may give direct feedback on the locally controlled mechanical forcing near cells. One requirement for such application is to know the initial bubble radius to enable the integration of Eq. 5.6. Acoustical techniques based on off-resonant bubble sizing [32, 33] could provide an estimate of the initial bubble radius. More elegantly, the size requirement could be fulfilled by the use of monodisperse ultrasound contrast agent microbubbles that can be produced through flow focusing in a lab-on-a-chip device [28, 34].

5.5.3 Subharmonic responses

From the analysis of the absence and presence of subharmonic signals we may conclude that surface modes do not transmit sound at the subharmonic frequency in the far field. Surface modes may still play a role in the initiation of volumetric subharmonic oscillations. However, the optical plane of the microscope is parallel to the wall, and any non-spherical modes with an orientation normal to the wall will not be visible in the optical images [19]. Therefore a more detailed investigation requires the addition of another objective to also visualize the non-spherical modes of the bubble normal to the wall as in [19].

5.6 Conclusions

In conclusion, we have experimentally shown that the radial dynamics of an isolated oscillating microbubble can predict the acoustic emission resulting from these dynamics. It is shown that the higher order harmonics in the radial dynamics of the microbubbles are enhanced in the acoustic emission, which is in agreement with the theoretical predictions. Vice versa, we show that the measured acoustic emission resulting from an isolated oscillating microbubble with known initial bubble radius can be converted to correctly describe the bubble dynamics. Ultra-high speed imaging and acoustical recordings are shown to complement each other in the characterization of both the dynamic and the acoustic behavior of ultrasound contrast agent microbubbles. Small amplitude and higher harmonic behavior is shown to be more sensitively characterized by acoustical techniques. Non-spherical oscillations and low frequency behavior such as "compression only" behavior, essential for modelling and predicting bubble behavior, are exclusively visible in optically recorded bubble dynamics.

References

[1] J. R. Lindner, "Microbubbles in medical imaging: current applications and future directions", Nat. Rev. Drug Disco. **3**, 527–533 (2004).

[2] P. Marmottant and S. Hilgenfeldt, "Controlled vesicle deformation and lysis by single oscillating bubbles", Nature **423**, 153–156 (2003).

[3] P. Prentice, A. Cuschieri, K. Dholokia, M. Prausnitz, and P. Campbell, "Membrane disruption by optically controlled microbubble cavitation", Nature Physics **148**, 1–4 (2005).

[4] C. T. Chin, C. Lancee, J. Borsboom, F. Mastik, M. E. Frijlink, N. de Jong, M. Versluis, and D. Lohse, "Brandaris 128: A digital 25 million frames per second camera with 128 highly sensitive frames", Rev. Sci. Instr. **74**, 5026–5034 (2003).

[5] P. N. Burns, J. E. Powers, D. Hope Simpson, A. Brezina, A. Kolin, C. T. Chin, and T. Fritzsch, "Harmonic imaging: New imaging and doppler method for contrast enahanced us", Radiology **185**, 142 (1992).

[6] V. Mor-Avi, E. G. Caiani, K. A. Collins, C. E. Korcarz, J. E. Bednarz, and R. M. Lang, "Combined assessment of myocardial perfusion and regional left ventricular function by analysis of contrast-enhanced power modulation images", Circulation **104**, 352–357 (2001).

[7] D. Hope Simpson, C. T. Chin, and P. N. Burns, "Pulse inversion doppler: a new method for detecting nonlinear echoes from microbubble contrast agents", IEEE Trans. Ultrason. Ferroelec. Freq. Contr. **46**, 372–382 (1999).

[8] N. de Jong, A. Bouakaz, and P. J. A. Frinking, “Basic acoustic properties of microbubbles”, Echocardiography **19**, 229–240 (2002).

[9] S. van der Meer, B. Dollet, M. Voormolen, C. T. Chin, A. Bouakaz, N. de Jong, M. Versluis, and D. Lohse, “Microbubble spectroscopy of ultrasound contrast agents”, J. Acoust. Soc. Am. **121**, 648–656 (2007).

[10] P. Marmottant, S. van der Meer, M. Emmer, M. Versluis, N. de Jong, S. Hilgenfeldt, and D. Lohse, “A model for large amplitude oscillations of coated bubbles accounting for buckling and rupture”, J. Acoust. Soc. Am. **118**, 3499 – 3505 (2005).

[11] J. Sijl, E. Gaud, P. J. A. Frinking, M. Arditi, N. de Jong, D. Lohse, and M. Versluis, “Acoustic characterization of single ultrasound contrast agent microbubbles”, J. Acoust. Soc. Am. **124**, 4091–4097 (2008).

[12] E. Stride, “The influence of surface adsorption on microbubble dynamics”, Phil. Trans. R. Soc. A **366**, 2103–2115 (2008).

[13] A. Doinikov and P. A. Dayton, “Maxwell rheological model for lipid-shelled ultrasound microbubble contrast agents”, J. Acoust. Soc. Am. **121**, 3331–3340 (2007).

[14] M. Emmer, A. van Wamel, D. E. Goertz, and N. de Jong, “The onset of microbubble vibration”, Ultrasound. Med. Biol. **33**, 941–949 (2007).

[15] M. Emmer, H. J. Vos, and N. de Jong, “Radial modulation of single microbubbles”, IEEE Trans. Ultrason. Ferroelec. Freq. Contr. **56**, 2370–2379 (2009).

[16] T. G. Leighton, *The acoustic bubble (Academic, London, 1994)* (1994).

[17] S. Hilgenfeldt, D. Lohse, and M. Zomack, “Response of bubbles to diagnostic ultrasound: a unifying theoretical approach”, Eur. J. Phys. **4**, 247–255 (1998).

[18] S. Zhao, K. W. Ferrara, and P. A. Dayton, “Asymmetric oscillation of adherent targeted ultrasound contrast agents”, Appl. Phys. Lett. **87**, 134103–3 (2005).

[19] H. J. Vos, B. Dollet, J. G. Bosch, M. Versluis, and N. de Jong, "Non-spherical vibrations of microbubbles in contact with a wall - a pilot study at low mechanical index", Ultrasound. Med. Biol. **34**, 685–688 (2008).

[20] C. F. Caskey, S. M. Stieger, S. Qin, P. A. Dayton, and K. W. Ferrara, "Direct observations of ultrasound microbubble contrast agent interaction with the microvessel wall", J. Acoust. Soc. Am. **122**, 1191–1200 (2007).

[21] J. R. Lindner, J. Song, A. R. Jayaweera, J. Sklenar, and S. Kaul, "Microvascular rheology of definity microbubbles after intra-arterial and intravenous administration", J. Am. Soc. Echocard. **15**, 396–403 (2002).

[22] R. Jeurissen, A. van der Bos, H. Reinten, M. van den Berg, H. Wijshoff, J. de Jong, M. Versluis, and D. Lohse, "Acoustic measurement of bubble size in an inkjet printhead", J. Acoust. Soc. Am. **126**, 2184–2190 (2009).

[23] M. P. Brenner, S. Hilgenfeldt, and D. Lohse, "Single-bubble sonoluminescence", Rev. Mod. Phys. **74**, 425 – 483 (2002).

[24] K. Vokurka, "On rayleigh's model of a freely oscillating bubble. I. basic relations", Czech. J. Phys. **35**, 28–40 (1985).

[25] V. Garbin, B. Dollet, M. Overvelde, D. Cojoc, E. Di Fabrizio, L. van Wijngaarden, A. Prosperetti, N. de Jong, D. Lohse, and M. Versluis, "History force on coated microbubbles propelled by ultrasound", Phys. Fluids **21**, 092003–7 (2009).

[26] D. H. Kim, M. J. Costello, P. B. Duncan, and D. Needham, "Mechanical properties and microstructure of polycrystalline phospholipid monolayer shells: Novel solid microparticles", Langmuir **19**, 8455–8466 (2003).

[27] N. de Jong, M. Emmer, C. T. Chin, A. Bouakaz, F. Mastik, D. Lohse, and M. Versluis, ""Compression-Only" behavior of phospholipid-coated contrast bubbles", Ultrasound Med. Biol. **33** (2007).

[28] B. Dollet, W. van Hoeve, J. P. Raven, P. Marmottant, and M. Versluis, "Role of the channel geometry on the bubble pinch-off in flow-focusing devices", Phys. Rev. Lett. **100**, 034504 (2008).

[29] A. van Wamel, K. Kooiman, M. Harteveld, M. Emmer, F. J. Ten Cate, M. Versluis, and N. de Jong, “Vibrating microbubbles poking individual cells: Drug transfer into cells via sonoporation”, J. Controlled Release **112**, 149–155 (2006).

[30] C. D. Ohl, M. Arora, R. Ikink, N. de Jong, M. Versluis, M. Delius, and D. Lohse, “Sonoporation from jetting cavitation bubbles”, Biophys. J. **91**, 4285–4295 (2006).

[31] X. Liu and J. Wu, “Acoustic microstreaming around an isolated encapsulated microbubble”, J. Acoust. Soc. Am. **125**, 1319–1330 (2009).

[32] A. D. Phelps and T. G. Leighton, “High-resolution bubble sizing through detection of the subharmonic response with a two-frequency excitation technique”, J. Acoust. Soc. Am. **99**, 1985–1992 (1996).

[33] H. Medwin, “Counting bubbles acoustically: a review”, Ultrasonics 7–13 (1977).

[34] K. Hettiarachchi, E. Talu, M. L. Longo, P. A. Dayton, and A. P. Lee, “On-chip generation of microbubbles as a practical technology for manufacturing contrast agents for ultrasonic imaging”, Lab on a Chip **7**, 463 – 468 (2007).

6

Conclusions

The characterization of any non-linear system starts with an understanding of the small amplitude behaviour of the system (see Ch. 1). The properties deduced from this linear analysis may then be extrapolated to investigate its non-linear characteristics. With an analysis of linear resonance curves determined from the radial dynamics of phospholipid coated bubbles obtained with the Brandaris ultrahigh-speed camera [1] van der Meer *et al.* have determined these linear properties for phospholipid coated microbubbles in 2007. The start of a complete understanding of the behavior of these bubbles was made. In this thesis we have expanded this knowledge in order to quantitatively describe and fundamentally understand some of the unique non-linear characteristics of phospholipid coated microbubbles.

In Ch. 2 we show that the small amplitude behavior of individual phospholipid coated microbubbles can be studied acoustically. An acoustical characterization provides a more direct measure for the contrast enhancing abilities of phospholipid coated microbubbles but also necessitates the isolation of a *single* microbubble. The quantification of the acoustic waveform scattered by the isolated bubbles is provided through a rigorous transducer calibration procedure. Accordingly, the measured acoustic backscatter allowed for a quantitative comparison with the full numerical model proposed by Marmottant *et al.* [2]. The quality of the agreement that was found between the theory and the experiment provides a strong validation of the full numerical model as proposed by Marmottant *et al.*.

In Ch. 3 the radial dynamics of differently sized phospholipid coated microbubbles, recorded with the Brandaris ultrahigh-speed camera [1], are investigated to quantify and to understand the effect of the coating on the effective surface tension of the microbubbles. Hereto we explore the non-linear "compression-only" behavior which is exclusively seen with coated microbubbles. We show that "compression-only" behavior is a second order non-linearity of the standard Rayleigh-Plesset equation. Interestingly, the nature of a phospholipid coating reverses the amplitude of this behavior as compared to uncoated bubbles, which in general are observed to expand more than they compress. Regarded as a second order non-linearity, a quantification of the "compression-only" behavior reveals how the effective surface tension of a phospholipid coated microbubble changes with bubble radius R. The results confirm the relation between the effective surface tension and R as proposed by Marmottant *et al.*. In addition we found that the break up tension as proposed in this model is essential to correctly describe the saturation of the "compression-only" behavior that occurs for increased oscillation amplitude. The amount of "compression-only" behavior is shown to be predominately determined by the initial concentration of phospholipids on the bubble surface. This initial concentration varies from bubble to bubble. The initial phospholipid concentration on the bubble surface is also shown to determine subharmonic behaviour of phospholipid coated microbubbles (see Ch. 4). For a microbubble that is initially saturated with phospholipids the subharmonic behavior is shown to be strongly enhanced as compared to uncoated bubbles. The analytical solutions determined from a weakly non-linear analysis of a general model for coated bubbles show a numerical model that assumes the effective surface tension of the bubble is strongly dependent on the bubble radius R is essential to predict subharmonic behavior for coated microbubbles at low acoustic driving pressure amplitudes. The excellent agreement found between subharmonically oscillating microbubbles recorded with the Brandaris ultrahigh-speed camera and the predictions of the numerical model proposed by Marmottant *et al.* confirm these analytical solutions. A characterization of ultrasound contrast agent microbubbles is incomplete without knowledge on the acoustic signature induced by the bubble dynamics. In the Ch. 2 we have characterized the linear acoustic response of the phospholipid coated microbubbles. In Ch. 5 we wrap up the thesis by demonstrating how the non-linear characteristics of the radial dynamics investigated in Ch. 3 and Ch. 4 are converted into an acoustic response. A combined optical and acoustical setup is used to validate that the bubble sound emission can be calculated from

the recorded radial dynamics. Vice versa we show how the radial dynamics of a microbubble can be determined from the remotely recorded acoustic response. We concluded that small amplitude and higher harmonic behavior is more sensitively characterized by acoustical techniques. Optical techniques on the other hand provide more direct information on low frequency behavior such as “compression-only” behavior. These last features of the bubble dynamics that are exclusively visible in optically recorded bubble dynamics are shown to be essential for modelling and predicting bubble behavior.
The findings presented in this thesis strongly support the hypothesis of Marmottant *et al.* that the elastic characteristics of phospholipid monolayers found under static conditions [3–5] can be extrapolated to higher frequencies/velocities. In addition, based on the results presented in this thesis, we claim that the relation between the phospholipid surface concentration and the effective surface tension is quantitatively the same for all phospholipid coated microbubbles. Differences in the dynamic behavior between phospholipid microbubbles can be completely accounted for by a difference in the initial phospholipid surface concentration of the bubble at rest. This hypothesis reduces the number of free parameters of the model proposed by Marmottant *et al.* [2] to a single parameter, namely the initial surface tension $\sigma(R_0)$. This result opens up new possibilities for the research on contrast-enhanced ultrasound imaging. With only a single free parameter, contrast enhancing pulse sequences can be reliably optimized almost entirely numerically, accelerating the time consuming experimental search for the optimal amplitude, frequency, envelope, and sequence of new imaging modalities. A future focus of the research on ultrasound contrast agents microbubbles should be to get experimental control over the initial surface tension $\sigma(R_0)$ of a phospholipid coated bubble. Mastering this parameter, for example through the use of specific phospholipids or gasses inside the bubble, will enable manufacturers of contrast agents to regulate the non-linear characteristics of their microbubbles. In the future this will allow for the development of ultrasound contrast agents specifically optimized for subharmonic, second harmonic, or other imaging modalities.

References

[1] C. T. Chin, C. Lancee, J. Borsboom, F. Mastik, M. E. Frijlink, N. de Jong, M. Versluis, and D. Lohse, “Brandaris 128: A digital 25 million frames

per second camera with 128 highly sensitive frames", Rev. Sci. Instr. **74**, 5026–5034 (2003).

[2] P. Marmottant, S. van der Meer, M. Emmer, M. Versluis, N. de Jong, S. Hilgenfeldt, and D. Lohse, "A model for large amplitude oscillations of coated bubbles accounting for buckling and rupture", J. Acoust. Soc. Am. **118**, 3499 – 3505 (2005).

[3] M. I. Sández, A. Suárez, and A. Gil, "Surface pressure-area isotherms and fluorescent behavior of phospholipids containing labeled pyrene", J. Coll. Interf. Sci **250**, 128–133 (2002).

[4] F. Pétriat, E. Roux, J. C. Leroux, and S. Giasson, "Study of molecular interactions between a phospholipidic layer and a ph-sensitive polymer using the langmuir balance technique", Langmuir **20**, 1393–1400 (2004).

[5] K. Y. C. Lee, "Collapse mechanisms of langmuir monolayers", Ann. Rev. Phys. Chem. **59**, 771–791 (2008).

Summary

This thesis describes the characterization of the dynamics and the acoustic responses of single BR14 (Bracco Research S.A., Geneva, Switzerland) ultrasound contrast agent microbubbles under the influence of ultrasound. As discussed in Ch. 1 a fundamental characterization starts with an understanding of the small amplitude behavior of isolated phospholipid coated microbubbles.

In Ch. 2 of this thesis we investigate the small amplitude behavior of isolated microbubbles acoustically. To ensure that the measured acoustic response originates from one bubble only, it requires the isolation of a single microbubble within an ultrasound beam. Furthermore to operate in the linear regime, the measurements should be performed at low acoustic driving pressure amplitudes, which puts stringent requirements on the sensitivity of the receiving transducer. In this chapter we present a study where both these challenges are met. Furthermore a rigorous transducer calibration method allowed us to extract quantitative information on the shell properties of individual microbubbles from the received bubble echoes. Small bubbles excited below their resonance frequency are shown to have a response dominated by the characteristics of their phospholipid shell, whereas larger bubbles, excited above resonance, have a response identical to those of uncoated bubbles of similar size.

In Ch. 3 the Brandaris ultrahigh-speed camera is used to investigate the radial dynamics of differently sized phospholipid coated microbubbles optically. Here, we present an experimental study where the driving pressure amplitude and frequency is varied to investigate the dependence of the nonlinear "compression-only" behavior of phospholipid coated microbubbles on the oscillation amplitude of the bubble wall. Through a weakly non-linear analysis of the equations describing the bubble dynamics it is shown that "compression-only" behavior is a second order non-linear effect that results from a rapidly varying shell elasticity of the bubble induced by the phospholipid shell. A comparison between the experimental results and full numerical simulations presented in this chapter show the initial surface tension of the bubble determines its the "compression-only" behavior.

Chapter 4 presents a study into the origin of the subharmonic behavior of phospholipid coated microbubbles. The Brandaris ultrahigh-speed camera is exploited to investigate the effect of the amplitude and the frequency of the driving pressure on the radial subharmonic dynamics of individual phospholipid coated microbubbles. The experimental results show that the phospholipid shell of the microbubbles can enhance subharmonic behavior of coated bubbles as compared to uncoated bubbles. Subharmonic oscillations are observed to occur already for driving pressures as low as 5 kPa. This is in contradiction with the assumption that the damping induced by the phospholipid shell reduces this non-linear behavior. In this chapter an explanation for the enhanced subharmonic behavior of phospholipid coated bubbles is provided. Through a weakly non-linear analysis of a general form of the numerical model describing the dynamics of coated bubbles it is shown that a shell elasticity that rapidly changes with bubble oscillation amplitude enhances subharmonic behavior. This rapid change in elasticity is hypothesized to result from the 3D-collapse of the phospholipid monolayer coating of the bubble, i.e. buckling of the phospholipid shell. The agreement that is found between the experimentally determined radial dynamics and the numerical model of Marmottant *et. al.* that takes into account the buckling of the shell confirms this hypothesis. The comparison between the numerical model and the experimental results shown that the subharmonic behavior of phospholipid coated microbubbles is strongly determined by the initial surface tension of the bubble similar to as was shown for "compression-only" behaviour. A bubble with an initial surface tension close to zero, i.e. a bubble of which the surface is initially completely saturated with phospholipids shows strong subharmonic behavior at low acoustic driving pressure amplitudes. In contrast, a bubble of which the surface is initially unsaturated with phospholipids shows no subharmonic behavior for driving pressure amplitudes up to 150 kPa.

In the final chapter, Ch. 5, the optical characterization methods of 3 and Ch. 4 are combined with the acoustical characterization method presented in Ch. 2. The radial dynamics and the acoustic response of individual isolated pulsating microbubbles are simultaneously recorded using the Brandaris ultrahigh-speed camera and a sensitive calibrated receive transducer. In this chapter we show how the bubble sound emission can be predicted from the recorded radial dynamics. Vice versa the radial dynamics of a microbubble can be determined from the remotely recorded acoustic response. It is shown how the experimental techniques used to record the radial dynamics and the acoustic response of the pulsating microbubble complement eachother in the characterization of the bubbles. Small amplitude and higher harmonic behavior is shown to be more sensitively characterized by acoustical techniques. Non-spherical oscillations and low frequency behavior such as “compression-only” behavior”, essential for modeling an predicting bubble behavior, are exclusively visible in optically recorded bubble dynamics. This chapter therefore proofs a complete understanding and optimal use of the non-linear properties of these coated microbubbles in medical imaging is achieved only through a combined optical and acoustical characterization.

Samenvatting

Dit proefschrift beschrijft de karakterisatie van de beldynamica en de resulterende echo van geïsoleerde BR14 (Bracco Research S.A., Genève, Zwitserland) microbellen onder de invloed van ultrageluid. De bellen met een schil van fosfolipiden worden gebruikt als contrastmiddel in medische beeldvorming met behulp van ultrageluid. In hoofdstuk 1 wordt eerst uitgelegd dat we eerst het lineaire systeem moeten bestuderen voor we de niet-lineaire dynamica van een complex systeem zoals die van een oscillerende bel kunnen begrijpen. De oscillaties van een bel zijn slechts dan lineair in het geval van kleine oscillatie amplitudes.

In hoofdstuk 2 van dit proefschrift onderzoeken we de akoestische respons afkomstig van enkele bellen. De bellen worden aangestraald door een ultrageluidsgolf met een lage amplitude om ervoor te zorgen dat de radiële uitwijking klein is, d.w.z. de bel gedraagt zich lineair. Om er zeker van te zijn dat de gemeten echo van één enkele bel afkomstig is, moet er voor worden gezorgd dat er inderdaad maar één bel in het akoestische focus van de transducer aanwezig is. De echo van één enkele bel bij lineaire aandrijving is slechts een enkele Pascal en dit stelt dus hoge eisen aan de gevoeligheid van de ontvangende transducer. Een nauwkeurige kalibratie van de ontvangende transducer stelt ons in staat om de gemeten echo te vertalen naar gedetailleerde informatie over de fysische eigenschappen van de belschil. Voor kleine bellen wordt de bel aangedreven onder resonantie en domineert de belschil het dynamisch gedrag van de bel. Voor grotere bellen welke worden aangedreven boven resonantie is de invloed van de schil minimaal en gedraagt de bel zich als een vrije gasbel zonder schil.

In hoofdstuk 3 van dit proefschrift maken we gebruik van de Brandaris 128 hogesnelheidscamera om optisch de dynamica van individuele microbellen van verschillende grootte te bestuderen. In dit hoofdstuk presenteren wij een experimentele studie naar een interessant en vooralsnog onbegrepen niet-lineair gedrag van fosfolipide gecoate bellen. We onderzoeken het "compression-only" gedrag, waarbij de bellen meer lijken te comprimeren dan dat ze expanderen. Het verband tussen "compression-only" gedrag en de oscillatie amplitude wordt vastgelegd door de frequentie en de druk van de ultrageluidspuls te variëren. Door gebruik te maken van storingsrekening toegepast op de bewegingsvergelijking van de bel, laten wij analytisch zien dat het "compression-only" gedrag van een bel een niet-lineairiteit van tweede orde is. Deze niet-lineariteit is het gevolg van een snelvariërende elasticiteit van de schil welke geïnduceerd wordt door een snelveranderende concentratie van de fosfolipiden op de schil van de bel. De experimentele resultaten en numerieke simulaties laten zien dat "compression-only" gedrag bepaald wordt door de initiële effectieve oppervlaktespanning van de bel.

In hoofdstuk 4 presenteren we een experimentele en theoretische studie naar het subharmonische gedrag van microbellen met een fosfolipiden coating. Met behulp van de Brandaris 128 hogesnelheidscamera is het effect van de frequentie en de amplitude van de ultrageluidspuls op de (subharmonische) dynamica van individuele gecoate microbellen onderzocht. De experimentele resultaten laten zien dat microbellen met een fosfolipide schil meer subharmonisch gedrag kunnen vertonen dan bellen zonder schil. In sommige gevallen vertonen de fosfolipide gecoate bellen al subharmonische oscillaties bij een amplitude van de aandrijfdruk van slechts 5 kPa. Dit in tegenstelling tot de algemeen geaccepteerde gedachte dat de fosfolipide schil van de microbellen extra demping veroorzaakt welke dit niet-lineaire gedrag onderdrukt. In dit hoofdstuk geven wij een verklaring voor het versterkte subharmonisch gedrag van fosfolipide gecoate microbellen. Met behulp van een storingsrekeningstechniek hebben we uit de bewegingsvergelijking van de microbellen met een fosfolipiden coating een analytische oplossing van tweede orde verkregen voor het niet-lineaire subharmonische gedrag van bellen. Uit deze analyse blijkt dat dit gedrag versterkt wordt doordat de elasticiteit van de schil varieert met de uitwijking van de bel. In dit hoofdstuk introduceren wij de hypothese dat deze snelle verandering van de schilelasticiteit veroorzaakt wordt door de vervorming en verkreukeling van de fosfolipide monolaag waaruit de schil van de bel bestaat. De goede overeenkomst die we vinden tussen de experimenteel gemeten radiële (subharmonische) dynamica van de bel en de numerieke simulaties gebaseerd op het model van Marmottant *et. al.* bevestigt deze hypothese. Het model van Marmottant *et. al.* neemt namelijk het kreukelen van de schil mee in de beschrijving van de dynamica van deze microbellen. Het vergelijk tussen de experimentele resultaten en het model laat zien dat het subharmonische gedrag van deze microbellen, net als hun “compression-only” gedrag, voornamelijk bepaald wordt door de initiële effectieve oppervlakte spanning van de bel. Een microbel met een initiële effectieve oppervlaktespanning dicht bij nul, d.w.z. een microbel waarvan het oppervlak bijna geheel verzadigd is met fosfolipiden en makkelijk kreukelt, laat al bij lage amplitudes van de opgelegde drukgolf veel subharmonisch gedrag zien. Daarentegen een microbel waarvan het oppervlak in de begintoestand niet volledig bedekt is met fosfolipiden, en zich meer elastisch gedraagt, laat geen subharmonisch gedrag zien voor een opgelegde drukgolf met een amplitude lager dan 150 kPa.

In het laatste hoofdstuk van dit proefschrift, hoofdstuk 5, combineren we de optische karakterisatiemethode van hoofdstuk 3 en hoofdstuk 4 met de akoestische meetmethode zoals gepresenteerd in hoofdstuk. 2. We laten zien dat het mogelijk is om tegelijkertijd optisch (met de Brandaris 128 camera) en akoestisch (met de gevoelige en nauwkeurig gekalibreerde transducer) beide responsies van individuele bellen te meten. In dit hoofdstuk laten we zien dat de echo van een pulserende bel berekend kan worden uit de optisch gemeten beloscillaties. Omgekeerd laten we zien dat de radiële oscillaties berekend kunnen worden uit de gemeten echo van de bel. Bovendien complementeren de akoestische en optische methoden elkaar, hetgeen resulteert in aanvullende fysische informatie van het schilgedrag. Aan de ene kant is de harmonische component van bellen die trillen met een kleine uitwijking akoestisch beter zichtbaar. De niet sferische oscillaties en laagfrequent gedrag zoals “compression-only” gedrag zijn daarentegen optisch beter zichtbaar. Dit hoofdstuk bewijst dan ook dat een volledig begrip van het gedrag van microbellen met een fosfolipiden coating, welke nodig is voor een optimaal gebruik van contrastmiddelen in medisch ultrageluid, enkel bereikt kan worden door de combinatie van optische en akoestische karakterisatiemethoden.

Acknowledgments

First of all I would like to thank Detlef Lohse, Michel Versluis and Nico de Jong for providing the opportunity to do my PhD in the Physics of Fluids group. With their guidance, support and encouragement I have learned many things during these last four years. Michel, besides your scientific supervision, you considerably helped to improve my skills in presenting, both in oral presentations and written work, not to forget my improved networking skills (drinking beer in the bar) at conferences.

My PhD is part of the NIMTIK (Non-Invasive Molecular Tumor Imaging and Killing) project. I want to thank the people of this project for the collaboration and the motivating lunch meetings we had every three months.

I want to thank Bracco Research SA for always supplying me with the necessary phospholipid-coated microbubbles that made this study possible. Bracco is also acknowledged for the financial support provided for my stay in Geneva in the first months of my PhD.

The work presented in this thesis was done together with many others. Without these people it would not have been possible to make the progress we made in understanding the dynamics of coated microbubbles. Therefore, I want to thank the co-authors of the first chapter of this thesis, Emmanuel Gaud, Marcel Arditi, Peter Frinking and other colleagues at Bracco Research SA for their valuable contributions to this work. I especially want to thank Peter Frinking for the inspiring scientific discussions we had throughout the four years of my PhD.

The co-authors of the second set of chapters of this thesis, Marlies Overvelde, Benjamin Dollet, Valeria Garbin, Rik Vos and Timo Rozendal are greatly acknowledged for their contributions. As direct colleagues I have really enjoyed working with you. Not only from a professional point of view but also personally. The drinks, diners, conference meetings, hikes, coffee breaks and philosophical discussions have made my PhD not only an inspiring but also a fun time.

Not all of the work that was done during the four year of my PhD is directly included in this thesis. Parts of this work has been presented at confer-

ences as abstracts, proceedings, posters or presentations and I want to thank, Todd Hay, Sander van der Meer, Paul van Neer, Francesco Guidi, Jacopo Viti, Pierro Tortoli, Constantin Ungureanu, Srirang Manohar for the collaboration that made this possible. During part of my PhD I had the privilege to be assisted by Bachelor and Master students. I want to thank Tamara van Weperen, Timo Rozendal, Daan Kater and Jan Veldhuizen for their contributions to this thesis and the nice collaboration.

The research in this thesis is greatly facilitated by Gert-Wim Bruggert, Martin Bos, Leo Bekkering and Cees Pakvis who have helped me with the design and building of the experimental setups. I also want to thank Bas Benschop for patiently solving all my ICT-problems. I must admit that in the last two years I have missed the necessity to get my first cup of coffee in the office of Gert-Wim, Martin and Bas. Since we moved to the Meander Building I completely lost track of the performances and latest results of FC Buurse. Evidently, I also want to thank Joanita Leferink for assisting me in the administrative part of my PhD.

A great part of the scientific support but also the fun during my PhD was provided by my colleagues and former colleagues in the POF group. I want to thank you all for the discussions, coffee breaks, lunch walks, dinners and drinks we had together. Special thanks to POF United and their coaches Jos and Arjan for the nice soccer matches we enjoyed together. Thank you, Benjamin, Wim, Valeria, James and Tess as my office mates for the help you have provided me in many ways, from deriving the equation of sound and explaining a Knudsen gas, to making coffee, providing me with fruits, and philosophical advice. Thank you Marlies, Rory, Bram, Sylvain, Edip, Eric, Amy, and Aaldert, my regular coffee and discussion mates for the many nice breaks.

Last but definitely not least, without the constant and warm support of my friends and family, accomplishing this work would not have been possible. I am thankful to my friends from Huizen, my friends in Amsterdam, ”doegroep de Vadsige Zeemeermin” (especially Ruud always supporting me in many ways), Maurits and friends from icehockey. Shelter, dinners, coffee, orange juices, beers, nice visiting friends and above all ’gezelligheid’ was provided by my room mates in Huize ’t Poortje, thanks for everything!

Very special thanks to my parents and my two brothers Roel and Tom for always being there. Femke, your love was the greatest support!

About the author

Jeroen Sijl was born on November 13th, 1980 in Laren (NH), The Netherlands. He graduated from high school ”Het dudok college” in Hilversum in 1999. In September of the same year he started studying Applied Physics at the University of Twente in Enschede. In 2003 Jeroen studied in Portugal at the University of Lisbon, ”Instituto Superior Téchnico” (IST). Apart from finishing nine months of the curriculum of Applied Physics he also learned to speak Portuguese in Lisbon and improved his skills in his favorite sport ,wave surfing. His stay in Portugal was ended with a three-month traineeship project in the Geophysics group of IST. Besides studying Applied Physics, Jeroen also finished the minor ”Sustainable development in a North South Perspective” at the University of Twente. This minor provided Jeroen with another opportunity to go abroad and do another traineeship. He went to Salvador de Bahia in April 2004, where he conducted a feasibility study on the empowerment of poor farmers in the region through the production and use of biodiesel. After this project, Jeroen went for nine months to Geneva, Switzerland to finish his masters. He worked for Bracco Research S.A., which is the producer of the Ultrasound Contrast Agent SonoVue$^{\mathrm{TM}}$. At Bracco Research, Jeroen conducted, in collaboration with the Physics of Fluids group of prof. dr. Detlef Lohse under guidance of dr. Michel Versluis and direct supervision of dr. ir. Peter Frinking and dr. Marcel Arditi, a study on ”The optical and acoustical properties of single microbubbles”. In July 2005 he graduated for his masters and continued his research on Ultrasound Contrast Agents as a PhD student in the Physics of Fluids group.